



# Bacterial communication in synthetic biology quantified by single cell (droplet) microfluidics

Inaugural dissertation

for the attainment of the title of doctor  
in the Faculty of Mathematics and Natural Sciences  
at the Heinrich-Heine-University Düsseldorf

presented by

Andrea Mückl  
born in Cham

Düsseldorf, November 2017



at the Chair of Physics of Synthetic Biological Systems, Physics Department  
Technical University of Munich

Published by permission of the Faculty of  
Mathematics and Natural Sciences at  
Heinrich-Heine-University Düsseldorf

|                |   |
|----------------|---|
| Supervisor:    | Jun. Prof. Dr. Ilka Maria Axmann<br>Institute of Synthetic Microbiology,<br>Heinrich-Heine-University                 |
| Co-supervisor: | Prof. Dr. Markus Kollmann<br>Institute of Mathematical Modelling and Biological Systems,<br>Heinrich-Heine-University |

Date of oral examination: 19.03.2018

# Statutory declaration and statement

## Erklärung

Ich versichere an Eides Statt, dass die vorgelegte Dissertation von mir selbständig und ohne unzulässige fremde Hilfe unter Beachtung der „Grundsätze zur Sicherung guter wissenschaftlicher Praxis an der Heinrich-Heine-Universität Düsseldorf“ erstellt worden ist. Ich habe keine anderen als die angegebenen Quellen und Hilfsmittel verwendet und habe alle Stellen, in denen ich Bezug auf die Arbeit anderer nehme, diese als solche kenntlich gemacht. Die Dissertation wurde in der vorgelegten oder in ähnlicher Form noch bei keiner anderen Institution von mir eingereicht. Ich habe bisher keine erfolglosen Promotionsversuche unternommen.

Gezeichnet

Andrea Mückl

Düsseldorf im November 2017



# Content

|   |      |
|---|------|
| Content.....  | v    |
| Abbreviations.....  | vii  |
| List of Publications .....  | viii |
| Author's declaration of contribution .....  | ix   |
| Abstract.....   | xii  |
| Zusammenfassung .....   | xiii |
| Aims of the thesis and their scientific context.....  | xiv  |
| Gene expression quantitation of synthetic sender and receiver bacteria .....  | xiv  |
| Communication and small molecule diffusion between emulsion droplets .....  | xv   |
| 1 Introduction.....   | 1    |
| 1.1. The concept of synthetic biology .....   | 1    |
| 1.2. A chronology through synthetic biology .....   | 1    |
| 1.3. Biological computation.....  | 4    |
| Traditional vs. biological computation .....  | 4    |
| <i>In vitro</i> computation .....   | 6    |
| <i>In vivo</i> computation .....  | 8    |
| 1.4. Quantitative single cell studies .....   | 9    |
| 1.5. Bacterial communication .....  | 11   |
| Quorum sensing – Diffusion sensing – Efficiency sensing .....   | 11   |
| Chemical communication in synthetic biology .....   | 12   |
| The diversity of signals.....   | 12   |
| AI-1 synthesis, release and response .....  | 13   |
| 2 Results .....   | 15   |
| 2.1. Single cell analysis of a bacterial sender-receiver system .....   | 15   |
| 2.2. Communication and computation by bacteria compartmentalized within<br>microemulsion droplets.....                                | 32   |
| 2.3. Chemical communication between bacteria and cell-free gene expression<br>systems within linear chains of emulsion droplets ..... | 37   |
| 3 Discussion.....   | 45   |
| 3.1. Gene induction quantitation at the single cell level .....   | 45   |
| 3.2. AHL mediated communication in microenvironments .....  | 47   |

## Content

|      |  |     |
|------|--|-----|
| 4    | References .....   | 49  |
| 5    | Appendix .....   | 60  |
| 5.1. | Single cell analysis of a bacterial sender-receiver system.....  | 61  |
| 5.2. | Communication and computation by bacteria compartmentalized within<br>microemulsion droplets .....                               | 72  |
| 5.3. | Chemical communication between bacteria and cell-free gene expression<br>systems within linear chains of emulsion droplets ..... | 96  |
|      | Acknowledgement – Danksagung.....  | 108 |
|      | Curriculum Vitae.....  | 109 |

# Abbreviations

|                |   |
|----------------|---|
| 3-oxo-C6-HSL   | 3-oxohexanoyl-homoserine lactone                          |
| Acyl-ACP       | acylated acyl carrier protein                             |
| Acyl-HSL       | acyl-homoserine lactone                                   |
| AHL            | acyl homoserine lactone                                   |
| AI             | autoinducer   |
| Cas            | CRISPR associated system                                  |
| CFS            | cell-free system  |
| CSF            | competence-stimulating factor                             |
| CPU            | central processing unit                                   |
| CRISPR         | clustered regularly interspaced short palindromic repeats |
| $D_a$          | apparent diffusion coefficient                            |
| $D_{eff}$      | effective diffusion coefficient                           |
| DNA            | deoxyribonucleic acid                                     |
| DPD            | 4,5-dihydroxy-2,3-pentanedione                            |
| DS             | diffusion sensing   |
| <i>E. coli</i> | <i>Escherichia coli</i>                                   |
| ES             | efficiency sensing  |
| FT             | fluorescence timer  |
| GFP            | green fluorescent protein                                 |
| IPTG           | Isopropyl- $\beta$ -D-thiogalactopyranoside               |
| IVTT           | <i>in vitro</i> transcription translation                 |
| MTP            | microtiter plate  |
| PCR            | polymerase chain reaction                                 |
| PDMS           | polydimethylsiloxane                                      |
| PEG            | polyethylene glycol                                       |
| PFPE           | perfluorinated polyether                                  |
| PHA            | polyhydroxyalkanoate                                      |
| QS             | quorum sensing  |
| QQ             | quorum quenching  |
| RFP            | red fluorescent protein                                   |
| RNA            | ribonucleic acid  |
| SAM            | S-adenosyl methionine                                     |
| SBOL           | synthetic biology open language                           |
| TALEN          | transcription activator-like effector nucleases           |
| TLFM           | time-lapse fluorescence microscopy                        |
| ZFN            | zinc finger nuclease                                      |

## List of Publications

The thesis consists of the following published research articles:

### Publication I

T. Ramalho, A. Meyer, **A. Mückl**, K. Kapsner, U. Gerland, F. C. Simmel, *Single cell analysis of a bacterial sender-receiver system*, PLOS ONE, e0145829 (2016).

### Publication II

M. Weitz\*, **A. Mückl**\*, K. Kapsner, R. Berg, A. Meyer, F. C. Simmel, *Communication and computation by bacteria compartmentalized within microemulsion droplets*, Journal of the American Chemical Society **136**, 72-75 (2014).

### Publication III

M. Schwarz-Schilling, L. Aufinger, **A. Mückl**, F. C. Simmel, *Chemical communication between bacteria and cell-free gene expression systems within linear chains of emulsion droplets*, Integrative Biology **8**, 564-570 (2016).

\*equally contributed

Other contributions with no subject-matter in the present thesis:

### **Book chapter**

M. B. Scheible, M. Weitz, **A. Mückl**, K. Kapsner, F. C. Simmel, *Biomedical Applications for Nucleic Acid Nanodevices*. In DNA and RNA Nanobiotechnologies in Medicine: Diagnosis and Treatment of Diseases, Springer Berlin Heidelberg, 329-348 (2013).

### **Manuscript**

M. Schwarz-Schilling\*, **A. Mückl**\*, K. Fischer, F. C. Simmel, *CRISPR-based control of cell division in Escherichia coli*, in preparation.

## Author's declaration of contribution

My personal contributions to the above listed publications are explained in detail on the following pages:

### **Publication I**

*Single cell analysis of a bacterial sender-receiver system*

Journal information:

PLOS ONE, Impact factor (2016) 3.057, peer-reviewed

Contribution information:

A. Meyer and **A. Mückl** conceived and designed the experiments together with FCS. The experiments were performed by A. Meyer and **A. Mückl**. The data were analyzed by TR, A. Meyer, KK, UG and FCS. TR and KK contributed customized software analysis tools. The paper was written by TR, A. Meyer, UG and FCS. KK and **A. Mückl** proofread the manuscript and contributed to the supplemental information part.

|           |                    |   |
|-----------|--------------------|---|
| Pro rata: | Experimental work: | 50%   |
|           | Data analysis:     | 1% (Fig C supplementary information)                            |
|           | Paper writing:     | 10% (of the supplementary information) plus helpful discussions |

## Publication II

*Communication and computation by bacteria compartmentalized within microemulsion droplets*

Journal information:

JACS, Impact factor (2016) 13.038, peer-reviewed

Contribution information:

MW and **A. Mückl** equally contributed to the paper. They conceived and designed the experiments together with FCS. The experiments (generation of emulsion droplets and time-lapse microscopy imaging) were performed by MW and **A. Mückl**. The data were analyzed by MW, KK and FCS. A. Meyer proofread the manuscript with helpful advice. KK provided customized software analysis tools. The paper was written by MW, **A. Mückl** and FCS. MW and **A. Mückl** supervised and trained RB in the framework of a bachelor thesis. **A. Mückl** constructed and cloned all plasmids in this study. Cell growth and cultivation was done by **A. Mückl**.

|           |                    |  |
|-----------|--------------------|--|
| Pro rata: | Experimental work: | 60%  |
|           | Data analysis:     | 15% (characterization of the genetic circuit together with RB) |
|           | Paper writing:     | 30%  |

### **Publication III**

*Chemical communication between bacteria and cell-free gene expression systems within linear chains of emulsion droplets*

Journal information:

Integrative Biology, Impact factor (2016) 3.371, peer-reviewed

Contribution information:

MSS, LA and **A. Mückl** conceived and designed the experiments which was supervised by FCS. The experimental work was performed by MSS and LA. **A. Mückl** prepared the cell-free gene expression system and constructed the bacterial strains. **A. Mückl** trained MSS and LA in soft lithography, microfluidic chip fabrication and cell culture handling. The data were analyzed by MSS and LA. MSS, LA and FCS wrote the paper with helpful discussions and concepts of **A. Mückl**.

|           |                    |  |
|-----------|--------------------|--|
| Pro rata: | Experimental work: | 30%  |
|           | Data analysis:     | 10% (analyzing the performance of the cell free expression system) |
|           | Paper writing:     | 10% (of the supplementary information) plus helpful discussions    |

Author's abbreviations:

LA: Lukas Aufinger, RB: Ronja Berg, UG: Ulrich Gerland, KK: Korbinian Kapsner, AM: Andrea Meyer, TR: Tiago Ramalho, MSS: Matthäus Schwarz-Schilling, FCS: Friedrich C. Simmel, MW: Maximilian Weitz

## Abstract

Bacterial communication or quorum sensing (QS) is a cell-density dependent way to regulate diverse functions in microbial communities. QS is mediated by autoregulative processes involving the production, sense and response of small, diffusible molecules such as acyl homoserine lactone (AHL). We utilize an artificial QS system based on isolated sender and receiver parts of the marine bacterium *Aliivibrio fischeri* and implemented the components in *Escherichia coli*. The sender cells produce AHL, while the receiver cells express a reporter gene in presents of AHL. The system is widely applied in synthetic gene circuits for the synchronization of bacterial behavior. However, to this end, important information on cellular heterogeneity and stochasticity of the system is lacking as well as information on the communication ability of bacterial groups confined for example in water-in-oil emulsion droplets.

In this thesis, we quantified gene expression dynamics at the single cell level, evaluated noise and subpopulation behavior of receiver cells and provided a method to determine the effective AHL concentration at the colony level in co-cultured sender and receiver bacteria. Our results provide quantitative detail and can be further used to elucidate communication behavior of other and natural bacterial communication systems.

We further clarified whether communication circuits can be established across emulsion droplets and what mechanisms describe the diffusion processes. We established artificial communication over large arrays of microemulsion droplets and linear droplet chains by the diffusion and integration of two amphiphilic inducer chemicals. We were the first showing communication between a bacterial receiver unit and an artificial cellular sender compartment producing AHL cell-free. Our results demonstrate the potential of programmed pattern formation by a tunable diffusion coefficient.



## Zusammenfassung

Kommunikation zwischen Mikroben wird als Quorum sensing bezeichnet. Diese Art der Kommunikation ist abhängig von der Zelldichte und regelt diverse Funktionen im mikrobiellen Zusammenleben. Quorum sensing wird ermöglicht durch einen autoregulativen Prozess, welcher die Produktion, das Aussenden und den Empfang von kleinen, diffundierenden Molekülen, den sogenannten AHLs, organisiert. Ausgehend von den natürlichen QS-Komponenten des gramnegativen Bakteriums *Aliivibrio fischeri*, wurde in dieser Studie ein voneinander getrenntes Sender-Empfänger System in *Escherichia coli* implementiert. Dabei wird AHL von den Senderzellen synthetisiert und in den Empfängerzellen durch Genexpression nachgewiesen. Dieses System ist schon lange bekannt und wird häufig zur Synchronisation von bakteriellern Verhalten in der synthetischen Biologie eingesetzt. Jedoch fehlen bis dato, wichtige Informationen zur zellulären Heterogenität und Stochastizität sowie Informationen über die Kommunikationsfähigkeit bakterieller Populationen in zum Beispiel Wasser-in-Öl Tröpfchen.

In dieser Dissertation quantifizieren wir Genexpressionsdynamiken auf der Einzelzellebene, bewerten zelluläres Rauschen sowie das Verhalten von Subpopulationen und zeigen eine Möglichkeit auf, die effektive AHL-Konzentration in einem Gemisch aus Sender- und Empfängerzellen zu bestimmen. Unsere Methode kann dazu beitragen, eine detaillierte, quantitative Aussage über andere, natürliche bakterielle Kommunikationssysteme zu erhalten.

In einer weiteren Studie wurde klargelegt, ob Kommunikationsschaltkreise über Emulsionströpfchen hinaus kreierte werden können und unter welchen Gesichtspunkten der Diffusionsprozess stattfindet. Wir starteten ein Kommunikationsexperiment mit dem Ziel möglichst große Flächen von Tröpfchenaneinanderreihungen als auch eindimensionale Anordnungen durch die Diffusion von amphiphilen Chemikalien wie AHL und IPTG zu induzieren. Wir waren die Ersten, die zeigen konnten, dass eine Kommunikation zwischen bakteriellen Empfängern und einem synthetischen, zell-ähnlichen Kompartiment welches AHL über einen zellfreien Synthesemechanismus produziert, aufgebaut werden kann. Die Ergebnisse dieser Studie können für weitere Bereiche der programmierbaren Musterbildung durch einen potentiell einstellbaren Diffusionskoeffizienten von Bedeutung sein.

## Aims of the thesis and their scientific context

### Gene expression quantitation of synthetic sender and receiver bacteria

Quantitation of gene expression is important, since ‘numbers’ are required to estimate parameters for theoretical models that help to understand and shed light on biological context. Especially in synthetic biology this is necessary to design functional systems with novel and useful features. Even genetically identical cells display huge variability in their gene expression dynamics and levels. This observed noise originates from intrinsic processes such as protein fluctuations or plasmid copy number effects or reasons from other extrinsic factors (1). Noise is generated over a wide range of cellular organizations which leads to heterogeneous populations. Nevertheless, bacteria evolved methods such as communication systems to reduce noise and synchronize their behavior with other cells. In nature, an elaborate communication system is likely important for survival in a continuously changing environment. The way of bacterial communication termed quorum sensing (QS) is mediated by diffusible molecules such as acyl homoserine lactone (AHL) that can be sent and received by a variety of species (2). Communication by simple diffusion of small molecules is an attractive strategy for synthetically designed genetic programs to minimize noise and enhance robustness in a population. Thus, quorum sensing as a tool to communicate the behavior between engineered bacteria gained wide interest in synthetic biology applications.

Moreover the role of noise in the context of quorum sensing has been investigated theoretically (3). On the experimental side, there exist also quantitative studies at the single cell resolution (4) and about the origin of noise in microcolonies (5). The focus in those studies however, was merely placed on natural quorum sensing systems. Therefore, in *Single Cell Analysis of a Bacterial Sender- Receiver System* (6), we aimed to investigate and quantify the heterogeneous gene induction behavior within a population of synthetic QS receiver bacteria. The cells were equipped with green fluorescent protein (GFP) under the lux-promoter. In a microfluidic chemostat, we utilized the receiver cells as a ‘bacterial sensor’ for AHL. We studied gene expression dynamics and their variability to learn and understand more deeply about cellular behavior at the single cell level. We further determined the effective AHL concentration in a system containing both AHL sender and receiver bacteria.

## Communication and small molecule diffusion between emulsion droplets

With the characterization data from our single cell experience and the knowledge about the signal ‘sending power’ on hand, we next tested our communication system in a bacterial computer. In the publication *Communication and Computation by Bacteria Compartmentalized within Microemulsion Droplets* (7) we investigated spatial properties of cell-to-cell communication and used emulsion droplets as model system for a heterogeneous environment.

Confined microenvironments allow scientist to study gene expression dynamics within a small population of cells under well-defined conditions. QS has been studied in other artificial microenvironments such as inkjet prints (8) or fiber-optic microarrays (9). More recently, bacteria have been confined in two emulsion droplets touching each other in a trap in which cell-to-cell signaling was studied across the contact area (10).

In contrast to previous studies, our emulsion based droplet system uses spatially large arrays of water-in-oil droplets containing either engineered bacteria or chemical reservoirs. We tested the diffusion of sender molecules in a distance-dependent manner. Thus, we addressed the question whether AHL and other compounds dissolve in the oil phase and whether communication takes place mainly through the interface of adjacent droplets in direct physical contact or via free diffusion through the oil. The established reaction-diffusion model revealed a reduced apparent diffusion coefficient.

As an application of our potentially tunable diffusivity, we extended our engineered bacteria to integrate AHL and a second amphiphilic chemical such as Isopropyl- $\beta$ -D-thiogalactopyranoside (IPTG). We showed the potential of distributed computing in spatially separated compartments by a synthetic AND gate gene circuit on a reduced length scale compared to aqueous medium. Thus, we provide a setup for genetically programmable pattern formation at a different length scale.

Since we observed a reduced apparent diffusion coefficient in earlier studies, we further aimed to quantitatively understand the diffusion process of autoinducers in a heterogeneous medium such as emulsions, which was lacking to this end. For this, we arranged emulsion droplets in capillaries and presented our results in the publication *Chemical communication between bacteria and cell-free gene expression systems within linear chains of emulsion droplets* (11).

The setup represented a simple one-dimensional diffusion process along the long axis of a capillary and was based on a gradient of inducer molecules that switches on genes in a position-dependent manner. The scientific context of this study applies to spatially-directed gene expression, which plays an important role in cellular differentiation during development and is also triggered by signal molecule (morphogen) gradients. Thus, our system represents further a useful model to reveal developmental processes in an artificial context.

Our results in this study indicated an AHL molecule transport via two distinct processes involving partitioning into the oil and micelle-mediated transport via the surfactant. In addition, the strong chemical coupling between neighboring compartments in the 1D geometry led to an extended spatial range compared to our 2D setup. This enabled us to a more sophisticated arrangement in which we further expanded our system to a communication network between artificial cellular compartments, equipped with genetic constructs, and bacteria. We first demonstrated the communication ability between such a cell-free signal producing sender system and a bacterial receiver system.



# 1 Introduction

## 1.1. The concept of synthetic biology

Synthetic biology uses elements from engineering and computing to design and construct biological devices and systems in a predictive way and for a useful purpose (12). Such a goal may be the manufacture of new materials and drugs, the production of high value food, the improvement of human health and environmental pollutions (13) or the ambitious intention to create life (14). The engineering aspect includes rational design basics such as abstraction, standardization, specification and modularization (12).

Abstraction in terms of biological processes is often useful and readily applied by representing proteins as circles or DNA as a line. This approach demands standardized rules as well as characterized and cataloged parts with potential utility (14). One step in this direction was taken by Christopher A. Voigt, Thomas F. Knight and Drew Endy some of the early pioneers of modern synthetic biology. The synthetic biology open language (SBOL) and the public registration of biological parts ([http://parts.igem.org/Main\\_Page](http://parts.igem.org/Main_Page)) provide the demands for standardization and allow simple selection of biological devices with defined functions. For instance, an operon can turn into a highly modular biological building block by combining the subunit with other parts towards sophisticated constructs with a predictable performance such as circuits (12,15).

From the computational perspective, software aided tools such as flux-balance programs for metabolism studies (16), translation calculators for optimization of ribosome binding sites (17,18), the D-Tailor package for the automated analysis and design of DNA sequences (19) as well as protein structure and (multi)domain engineering platforms (20,21), numerous databases such as BioModels for the computational description of biological processes (22) and other computer aided tools (23), are central technologies for synthetic biology workers.

## 1.2. A chronology through synthetic biology

The idea of making life is old and at the same moment the idea of synthetic biology. Indeed, some visions can be traced back to the beginning of the 20<sup>th</sup> century. The following section gives a brief overview about the historical developments and the outstanding scientists of their time and their visions. Those brought us to the point of synthetic biology as we understand it today. The most of this part is referred to the work of Porcar and Peretó (12) presented in their book “Synthetic Biology”. Within this section, I refer to selected publications of groundbreaking achievements that helped on synthetic biology and served as foundation and motivation for the results presented in this thesis.

Based on the fundamentals of biology provided by Gregor J. Mendel, Louis Pasteur, Eduard Buchner or Charles R. Darwin one century before, the French Biologist Stéphane A. N. Leduc published his work “La biologie synthétique” in 1912 and wondered “Why is it less acceptable to seek how to make a cell than how to make a molecule?” (24). In respect to this high-aimed question, there was a shared idea that scientists such as S. Leduc, Edward A. Schäfer, Thomas H. Huxley and others had in common around this time, namely that life was inseparably linked to matter and must underlie physical and chemical laws or to say in the words of Huxley “the physical basis or the matter of life was what united all

living beings”. Another seminal scientist of this time was Jacques Loeb. His effort to evoke the interest in studying cell biology thoroughly from a physicochemical point of view was decisive for the whole field.

Indeed, knowledge about cell chemistry was rudimental at this time. With the development of important technologies, especially in structural molecular biology and advanced imaging such as X-ray diffraction (25,26) and protein crystallography (27), major breakthroughs quickly set in:

In 1953, the DNA structure was solved (28,29), but also Stanley L. Miller and Harold C. Urey were the first who synthesized amino acids in an early atmosphere simulating ‘test tube’ by applying electricity to different gases. The origin of life by chemical evolution was also early propagated by the biochemist Alexander I. Oparin (30) and is still subject of modern science (31,32). Only a few years later, scientist at Berkeley observed the self-assembly of infectious virus particles after mixing virus-related proteins with genomic RNA. The identification of DNA modifying enzymes (33) by researcher around Arthur Kronberg led to the synthesis of biological-active circular phage DNA in 1967 (34). Studies on enzyme activity (35) and the description of gene regulation from an engineering point of view significantly improved the development in this field. In return, Jacques L Monod, François Jacob and André M. Lwoff were awarded with the Nobel Prize in Physiology or Medicine in 1965.

The potential of synthetic biology was early understood by Waław Szybalski. With their contribution on DNA-mediated gene transfer in mammalian cells (36), the authors Elizabeth Hunter Szybalska and Waław Szybalski coined the term synthetic biology in 1974. Their work is today generally recognized as the forerunner of modern gene therapy. When the enzymatic cleavage of DNA was discovered and intensely studied throughout the 1970s, the dramatic potential of the new technique, namely to manipulate DNA sequence-specifically (37,38), inspired Szybalski to the following comment in 1978:

“The work on restriction nucleases not only permits us easily to construct recombinant DNA molecules and to analyze individual genes, but also has led us into the new era of synthetic biology where not only existing genes are described and analyzed but also new gene arrangements can be constructed and evaluated” (39)

Hence, synthetic biology principally arose from recombinant DNA technologies. In the 1980s, Kary B. Mullis and Fred A. Faloona (40) made it possible to amplify DNA by polymerase chain reaction (PCR). Along with the ‘omics era’ and the decoding of the human genome (41), many researcher, in special those working on interdisciplinary topics settled between chemistry and biology such as Eric T. Kool, started to call their work synthetic biology in 2000 (42), a meaningful year for the entire ‘SynBio’ community.

Just in the same year, Michael B. Elowitz and Stanislas Leibler published their almost legendary work about the ‘repressilator’ (43), the first synthetic gene oscillatory circuit implemented in *E. coli*. A genetic network arranged in a rock-paper-scissor fashion where each symbol beats the next in the loop. At the genetic level this means that a repressor protein represses the next gene in a configured cycle and is repressed by the previous gene itself. Interestingly, the observed oscillation periods were longer than a cell’s replication cycle, hence the dynamics of the circuit were inherited from one generation to the other.

From there on, synthetic biology was boosted and still benefits form accompanied side-effects: these comprise the development of ‘big data’ handling solutions, the development of advanced sequencing technologies, the continuously decreasing prices for DNA synthesis and recently, the development of powerful and sophisticated computer modeling

and simulation software for rational design and analysis of gene regulation mechanisms and molecules with predictable function. Despite others, *in silico* biology quickly opened the gates towards the first ‘real world’ applications and synthetic microbes:

30 years after the first chemical synthesis of a short gene coding for a transfer RNA (44), J. Craig Venter showed the solely chemically synthesis of genome fragments assembled into a whole chromosome *in vivo* and the successful transplantation of the genome into a recipient cell, starting self-replication (45). Recently, advancements in metabolic and pathway engineering led to the development of novel materials such as bioplastics, produced from sugars or naturally occurring polyesters such as polyhydroxyalkanoates (PHA). Bacterial cellulose and poly(lactic acid) are now used by many Biotech companies to coat medical products (46).

Scientists developed versatile research interests among synthetic biology. Besides diverse *in vivo* approaches subject to bacterial engineering, as already highlighted in selected cases, there exist many projects with the goal to decrease the dependence on cells in order to increase engineering flexibility. This *in vitro* synthetic biology will be introduced in chapter [\*in vitro\* computation](#).

The latest dramatic contribution of a technological development was recently achieved in the field of genome editing (47). Site-specific cleavage of double-stranded DNA for sequence manipulation is now easily possible in any species and living organisms. Together with zinc finger nucleases (ZFNs) or transcription activator-like effector nucleases (TALENs), clustered regularly interspaced short palindromic repeats (CRISPR) found in the CRISPR-associated system (Cas) of bacteria are the methods of choice for diverse gene manipulations. First described by researcher around Jennifer A. Doudna and Emmanuelle M. Charpentier (47) the novel technique CRISPR/Cas9 already gained traction in industry and medicine. Special designed ‘molecular scissors’ were recently tested in persons (48). Several clinical trials with the CRISPR/Cas9 system already commenced in 2017 to treat various cancer types.

The promising new approach announces an exciting era for synthetic biology and many other ‘technosciences’, which let me conclude the developments in this field so far with the statement of Wacław Szybalski (1974):

Synthetic biology is “[...] a field with unlimited expansion potential and hardly any limitations to building ‘new better control circuits’ and [...] I am not concerned that we will run out of exciting and novel ideas [...]”. (49)

### 1.3. Biological computation

Biological computation is closely linked to synthetic biology. Building organisms that perform computational tasks by themselves is of major interest. Contrariwise, the abstraction of biological systems, inspired by electronic components such as resistors or capacitors is an attempt to understand biology in a more unified manner (50). Indeed, biological systems compute as defined by mathematical relationships, however it is not easy to disclose the ‘How’ and the ‘Why’ they compute and the principles and general laws applying to their operations. It is far from simple to simulate the computational part that living organisms solve in nature. Larger network structures can be solved, in principal, by means of Gillespie’s algorithm, even though computationally demanding (51).

Systematic problem solving with the help of computational models is the key instrument of computer science. The fragmentation of natural tasks into abstract descriptions, coarse-grained networks linked to experimental setups that reveal the number of species involved and their amount is essential in understanding and controlling biological computation.

Obviously, computational tools accelerate biological problem solving. According to our expectations, cellular logic operations are essential for biological systems to compute. The following paragraphs give attention to our ‘traditional’ understanding of computation and how we transfer it to cells. Directly after, I introduce current directions of computational *in vitro* and *in vivo* approaches towards programmable biology (52).

#### Traditional vs. biological computation

In a computer, information is processed via logic operations by the CPU. The information is of digital nature and handled as bits. The memory is fixed or rewritable and stored centralized. The computational operations are deterministic and exact, leading to an ultimate result (50). In contrast to traditional computers, living systems process information via different molecules that diffuse, compared to physically mounted transistors. Many biological processes can be expressed as logic functions (53) or algorithms (54). For example, a simple AND-gate operation is achieved, when a reporter gene such as GFP is only expressed in the presents of two input signals, shortly expressed as:  $GFP = [input1] \text{ AND } [input2]$ . The input molecules can be e. g. [quorum sensing](#) signal molecules or certain types of sugars. So, numerous applications can be implemented in cells by the construction of logic circuits from Boolean operation building blocks. For instance, distributed bacterial computing was shown by Tamsir and colleagues (55). A genetic NOR gate, consisting of wired and orthogonal QS sender and receiver units, revealed the production of all possible two-input gates. Also, one of the first computational tasks realized in *E. coli* was a genetically encoded toggle switch (56). The synthetic circuit was composed of two different repressible promoters arranged in the fashion that the gene products under control of the corresponding promoter inhibited the expression of the other in an alternating way. External signals switched the system between the two possible states.

Such coupled biochemical reactions are basically of analog nature. Biological reactions get only approximately depict by logic circuitry, due to the dependence on stoichiometry, concentration or rate parameters of the individual species and interactions involved. Biomolecular switches that compute continuous-value functions such as multiplications are hardly implemented (53). One example of such a system is represented in an ‘adder’ gate, a genetic network that counts (57). Here, the output level is the sum of its inputs’ levels. In addition, it is often difficult and inefficient to implement complex circuits in an individual cell. Supported by this view, Regot *et al.* (58) created a library of engineered



cells each endowing a logic function combinable in multiple ways. With some small consortia of these cells, a cellular multiplexer was practically tested in yeast. Another sophisticated task could be the recording of the number of cell divisions, assuming memory is handed over. In computation, memory is a quite useful feature and was remarkably recently implemented in a molecular version of logic circuitry (59).

As mentioned, the distributed information-processing in a cell often struggles with noise. The origin of noise is both, intrinsic (due to variations of small molecules such as plasmid copy numbers (60) in femtoliter-sized cell volumes) as well as extrinsic (fluctuations of environmental parameters such as the number of individual system components depending on growth, space and food conditions) (1,61,62). The computed results and the dynamic cell behavior are often of expedient nature and based on stochastic effects. Those stochastic fluctuations play a crucial role when working with microbes like *E. coli*. In this case, the noisy nature of cellular computation and thus gene expression dynamics has to be taken into account when genetically encoded programs are performed at the single cell level, as designed in this thesis.

Since biological systems are complex, the information represented, computed and communicated by the system are complex (63). The continuous character of living entities impedes the clear perception of what exactly is the input or output signal of a certain operation (50). In most biological cells neither exist synchronization. However, quorum sensing (QS) is a natural strategy to synchronize large numbers of individual system components in a certain way, comparable to the synchronization process that is commonly achieved with software engineering tools such as spinlocks, barriers or semaphore control mechanisms in multi-processor systems, executing parallel tasks with shared resources or codes (64). Data synchronization plays an important role in computer sciences. In biology for instance, horizontal gene transfer (and in special cloning) serves in terms of data matching with the goal to equip the entire population with the same genetic material. The phases of data synchronization are closely related and involving data extraction, transfer and transformation plus integration to the new host system, although the temporal demands can differ remarkably.

However, genetic data are affected by mutations and these frequently result in certain discrepancies. In data transmission with traditional computing systems, soft errors and their probability can be handled and decoded by certain error control algorithms (65,66). In living systems, mechanisms that prevent fluctuations and facilitate robust regimes must be considered (53). This is attempted for example by quantitative threshold implementations to flag active or inactive states towards digitalized output levels (very low or very high signals). Although, stochastic properties have less dramatic effects when a group of cells are observed on the basis of the population's mean, which levels out fluctuation effects (67).

### *In vitro* computation

The interest in molecular computers dates back decades (68) and one of the first realized system was presented by Leonard Adleman (69). It was about a DNA-based computer that solved a graphical combinatorial problem by oligonucleotide base-pairing. The solution was resolved on an agarose gel.

In principle molecular switches and circuits are still preferentially designed of DNA, followed by RNA and protein building units (53) simply due to the fact that base-pairing underlies predictable rules.

For biological computation, the matrix in which the system components are embedded or confined also plays an important role. Chemical reaction-diffusion experiments as applied in pattern formation studies, are better controllable in a well-defined environment. This makes *in vitro* approaches attractive. Due to the absence of cell division and unnecessary metabolic fluxes, computational modeling is simplified *in vitro*, allowing increased circuit complexity beyond proof-of-concept experiments (53). Up to now, gel-based reactors, filled capillaries or microfluidic setups and emulsion droplets have been used for compartmentalization. In Schwarz-Schilling *et al.* (11), we demonstrate a simple approach towards the study of spatial differentiation in cell-free reaction-based droplet confinements. The following paragraphs, hereafter, are brief introductions to cell-free systems and emulsion droplets.

*Cell-free systems* (CFSs) or *in vitro* transcription-translation (IVTT) reactions are usually prepared from whole-cell lysates of the desired strain or species (70-72). They are completed with further components such as salts, energy solutions or additional amino acids (73) required for proper performance. 1967 marks the beginning of CF era. The enzyme  $\beta$ -galactosidase was first synthesized *in vitro* by the group of Zubay (74). Shortly after, the Penman group and others established the synthesis of polypeptides from various DNA sources including viruses (75) and bone-marrow (76) within divers CFSs (77).

To overcome expression limitations and other impairing effects such as low yields or long delay times due to laborious preparation procedures, CFSs have been consciously optimized since then. For instance, it is now common practice to exploit the high-level transcription rate of phage T7 RNA polymerase *in situ* (78,79). One simple and straight way to obtain stable and soluble or unique proteins with novel function in CFSs, is the incorporation of unnatural amino acids as reviewed by Jewett (80). However, most crude cell extracts contain undesired components such as proteases and nucleases. The absence of any nuclease activity was achieved by recombinant protein synthesis and purification of all system components. The so reconstituted IVTT machinery, called PURE® system (81) has unique advantages regarding protein stability and design. However, this IVTT mix is expensive and less efficient regarding yield. Other methods to overcome DNA degradation in crude cell extracts exist (82). Due to their well-known composition, IVTT were recently simulated (83). Oscillatory gene expressions have been modeled and implemented in CFSs. To this end, the circuit dynamics were maintained by microfluidic devices that dilute and feed the reaction mix (84,85).

Homemade CFSs or the commercial available PURE® system are widely applied in synthetic biology (86). Some applications for example include: rapid prototyping systems to test genetic circuits built by Gibson assembly (87), model systems for *in vitro* directed evolution studies (88) with the goal to improve enzyme stability at the industrial scale (89), or screening and selection projects that identify novel biochemicals or specific inhibitors (90). Other popular applications are the reengineering and redesigning of metabolic pathways (91). Recently, the production of *n*-butanol was tested and improved by means of CFSs (92). Furthermore, the use of CFS for diagnostic purposes (e.g. point-of-care

devices) is a growing sector and contemporary issue. Diverse low-cost biosensors implemented on portable devices such as simple freeze-dried paper discs, have been developed. Those have the ability to detect many infectious diseases *in situ* such as Ebola (93) or Zika (94) viruses within a few hours, based on genetic circuit networks in CFSs.

*Emulsions* are typically two-phase liquid components in which the oily one is dispersed in the continuous (often water) phase bearing oil-in-water emulsions (95) such as lipoproteins observed in living organisms. Other types of emulsions (water-in-oil droplets) and multi-bedded (water-in-oil-in-water) droplets are of particular interest for biochemical applications as microreactor. Studies in cell-like volumes can be performed in a wide range of concentrations depending on droplet size and on the applied compartmentalization technique (stochastic partitioning or ordered encapsulation (96)). Thus, single cells or molecules can be encapsulated in microdroplets as well (97). Numerous of such individual microcompartments offer the possibility to parallelize tests as designed for emulsion PCR reactions. This concept proved to be very powerful for drug screening and cell screening applications or *in vitro* evolution experiments selecting for specific ribozymes or functional proteins in a high-throughput manner (98-100). Moreover, emulsion droplets can be massively manipulated. After generation, they can be transferred into other traps or chamber devices (101), densely packed to hexagonal arrays or additional reagents can be added at any time point by fusion (102) or direct injection (103). Single droplets can be divided for further dilution purposes (104) or sorted due to their size (105) or actively in an electric field (106). It is also possible to retrieve encapsulated samples using mild extraction ways such as demulsification chips (107).

A special class of emulsions are microemulsions which are stabilized by surfactants against coalescence. Surfactants are surface-active agents with amphiphilic character that accumulate between the boundaries of immiscible phases, minimizing the free energy to form micro-sized droplets (108). Indeed, due to surface tension, the drops appear spherical. The role of the surfactant and the corresponding utilized oil is critical. Bearing on aqueous droplets dispersed into oil as used for bioreactors, the surfactant must further provide an inert interface to avoid interactions between the biological content of the aqueous phase and the inner boundary surface (109). Many biomolecules such as DNA, RNA or proteins used in gene circuits possess charged groups that are subject to denature and activity loss when electrostatically attached to surfaces. Thus, biocompatibility suffers when strong hydrophilic and charged surfactants are applied. Surfactants separate adjacent droplets and consist of hydrophilic head groups such as polyethylenoxide or polyethylene glycol (PEG) moieties and hydrophobic tail groups of various length of perfluorinated polyethers PFPE fluorocarbon (110). Diffusion can be the rate limiting step, when tails are too long (51). On the other hand, tail length is critical for stabilization against shear forces and densely packed droplet constructions. Copolymeric morphological structures synthesized of di- and triblocks of a PFPE-PEG-PFPE architecture (110) have shown to fulfill both requirements for diverse biochemical *in vitro* reactions.

While requirements for the surfactant were already assessed, an appropriate continuous phase has to be chosen carefully, too. Since droplets are often generated in microfluidic chips usually molded from polydimethylsiloxane (PDMS), the silicone-based elastomer is prone to swell when incompatible organic fluids are applied (111). Low solubility of biological substances and gas-permeability is also desired. Thus, the hydrophobic and lipophobic qualities of fluorocarbon oils (112) meet the demands and are frequently used in droplet production. Such as in this thesis, the non-ionic surfactant with PFPE-PEG-PFPE architecture developed by Holtze *et al.* (110) is used in combination with the fluorinated oil FC-40®.

Monodisperse size distributed emulsion droplets in the pico-to-femtoliter scale (113) are commonly obtained in microfluidic devices with carefully chosen chip geometry, whereas droplets with a high polydispersity can be generated by simple steering, vortexing or ultrasonication (114) (51). An ordinary droplet generator setup comprises the microfluidic device, pumps, valves and fluid flux control software. For on-chip detection, fluorescence image acquisition, UV-spectroscopy or electrochemical detection methods assist proper control systems.

The parameters which determine the droplet production are the viscosities and densities of the two phases (surfactant and oil), the interfacial tension, the applied volumetric flow rates and the channel geometry (inlet and outlet widths as well as channel height) which forms the flow-field in the laminar flow conditions (108). Considering all the aspects including shear stress and stochastic processes such as fluctuations in the laminar flow of liquids, the theoretical description of droplet forming is demanding, compared to the practical handling of this technique. In addition, the microfluidic droplet generator device can be made from different channel geometries (108). This comprise co-flow streams, a setup arranged by two concentrically assembled glass capillaries with the dispersed fluid inside and the continuous one in the outer tube. Cross-flow or T-junction devices and flow-focusing geometries (as used here) are widely applied, too. However, droplet formation physics and geometric modelling for drop breakoff would exceed the scope of this thesis and thus are not be further addressed here, but can be looked up as well as their numerous applications in recent reviews (108,109,115).

### *In vivo* computation

Alan M. Turing gave direction to the origin of spatial patterns and shapes in biological organisms (116). His work on the mathematical description of chemical reactions led him to the reaction-diffusion system, a model which explains the spatial and temporal changes in the concentration of involved chemical species due to chemical transformation and diffusion.

One early implementation of Turing's morphogenesis paper was shown by James D. Murray. With the theory on hand, he could explain the stripes' and spots' characteristics of the fur of cats (117). Further research in this area underpinned the involvement of the reaction-diffusion model in various biological processes such as tumor growth (118) or embryonic development of *Drosophila* (119,120). A subsequent recent highlight in programmed pattern formation has been realized by Tabor *et al.* (121). Edge detection is a sophisticated computational task required for segmentation algorithms in image processing, for instance. Based on a light/dark sensing circuit, the production of a black 'ink' between the boundaries of adjacent bacteria in the two different states (dark/light) was recently shown in *E. coli*. Upon the stimulation of the photoreceptor of a light-sensitive protein, a diffusible trigger molecule was produced by the cell, 'and' a functional NOT-light gate interpreted the dark state. Such a genetically wired program encoded in bacteria drove the final output as computed by reaction-diffusion equations. Beside pattern forming computations, engineered cells can also identify and report tumor forming cell states by multiple endogenous miRNA markers and finally initiate an apoptosis protocol (122). Other tailored microorganisms have been programmed to commit suicide, when subject to external stress, but 'altruistically' leave a public good for the survivors (123).

In the context of this thesis, a simple reaction-diffusion system is applied to model diffusion-mediated communication between bacteria. The cells are confined in micro-emulsion droplets arranged in spatially large arrays that can form position-dependent patterns (7).

#### 1.4. Quantitative single cell studies

Although, cells naturally live in highly spatiotemporal organized and complex networks, it is important to study their single cell existence (124,125). This has long been realized and quite powerful methods have been developed. Moreover, a quantitative display of genetic circuit behavior is only obtained when large numbers of single cells are measured. This originates from cell-to-cell variability in the expression levels (126,127), from persistence or aging (128) or other phenotypes which we interpret as ‘noise’. Recently, two distinct temporal noise phenotypes, concerning cell cycle duration and start variability in budding yeast were identified by histograms, generated out of quantitative microscope data analysis (129). Thus, single cell studies are preferentially performed in high-throughput-based manner. The common techniques and the developments in this fields are introduced at this point.

For this purpose, flow cytometry and subsequent sorting provide quantitative capacities for up to 100.000 events in classical end point measurements and reveal information on cellular size and granularity as well as expression levels from fluorescence detection (97,130). Recently, mass spectrometry was coupled to flow cytometry using isotopes instead of fluorophores which greatly expand the number of detectable parameters (131). Such hybrid systems are termed mass cytometry and reflect the current state-of-the-art setups.

Classical wide-field epi-fluorescence microscopes equipped with automated time-lapse image acquisition control provide insights into dynamic processes in living cells as well. At the same time, microfluidic platforms evolved that allow long-term monitoring in parallel of up to thousands of single cells in precisely defined chemostats with low reagent consumption (132). Beside droplet generation, microfluidic devices have been used to study aging in chips that trap the mother cell, while the outgrowing daughter cell is flushed away (133), and electron transport by the fabrication of distinct electrodes surrounded by a microchamber containing bacteria (134). When single cells come in contact with the electrode, a current increase was measured. Many more seminal studies with elaborate chip designs exist that revealed exciting results of bacterial life or provide myriad applications for diagnostic purposes. Recent reviews on microfluidics can be found here (135,136). Microfluidic design and fabrication conventionally involve soft lithography (137) and replica molding based on a gas-permeable silicone elastomer (such as PDMS) (138). Valve-based microfluidic devices have been developed which allow flexible and diverse manipulations such as the application of spatial or concentration-based gradients or time-dependent perturbations (139). Biological samples compartmentalized in emulsion droplets can also be simple transferred into microfluidic traps and imaged concurrently (95,140). Pressure-based flow controllers have been available recently that maintain precise flow gradients and waveform pulses. Microfluidic chips can be simply customized at low costs making them ideally suited for any kind of dynamic studies. The emergence of 3D printing has made the manufacture of next generation microfluidic chips possible reaching the ranges of bacterial demands (141,142). Many more single cell techniques exist which do not allow dynamic insights in living cells such as quantitative PCR, but complement other techniques such as microfluidic-based time-lapse acquisition.

Another technological boost in time-lapse fluorescence microscopy (TLFM) was made by the development of spectrally different gene variants of green fluorescent protein (GFP) with improved properties in brightness, maturation time or photo stability (143,144). With these fluorescent reporter proteins on hand, many parameters can now be monitored in the same cell just using appropriate filter sets for detection. From there on, it was possible to illuminate important network features such as genetic feedback loops in dynamic

measurements (145,146) or to shed light on the kinetic expression order of cellular events using green and red fluorescent protein fusions (147). But also, fundamental dynamic processes such as the interaction between a transcription factor and its target gene resulting in a gene regulation function with characteristic variability (148,149) or the determination of protein degradation rates (150) have been identified. The characterization of such simple systems has been proved to be useful when implementing synthetic circuit designs *in vivo*. Many more fluorescent tools have been realized since then. For dynamic tracking in live cells, photo switchable fluorophores (151) and fluorescence timers (FTs) (152) found great popularity. Also a panel of signal peptides that guide tagged fluorescence proteins (153) to a fast degrading protease system (ssrA) (154), are widely used when tunable protein stability is needed. Such tools are commonly applied in oscillatory circuits, for instance (43). Particularly interesting from the standpoint of transcriptional monitoring was the development of GFP-mimicking aptamers (155). These specific designed RNA sequences bind, stabilize and therefore switch on corresponding fluorescent molecules that resemble the fluorophore core of GFP. In addition, these fluorophores neither show unspecific light up nor cytotoxicity in cells. They represent a novel tool for the live observation of RNA transcription, previously inaccessible.

However, automated image analysis is required for most TLFM experiments, since up to thousands of cells and just as many time points are recorded. Manual dataset evaluation can be error-prone and often impossible. A classical approach to extract data out of image time-series begins with proper pre-processing. This involves background reduction by applying nonlinear filtering tools and deconvolution methods against blurring effects as well as proper segmentation algorithms based on the intensities of neighboring pixels. Segmentation methods can include edge detection, thresholding, water shedding and template matching procedures (156). The identified pixels belonging to a cell respectively the regions of interest give information about intensity, shape, size, velocity, pixel-to-pixel fluctuations, co-localization of regions in other color channels, ancestral trajectories of single cells and many more criteria which can be tracked over time (125).

Finally, the continuous improvement of image analysis software is anticipated, although many commercial and open-source software packages are available. For instance, Matlab and the freeware ImageJ are two mainly accepted software suites for academic image analysis, but there are many others such as CellTracer, which have their individual strengths and weaknesses. Since no program could possibly analyze every experimental setup (125), it should be customizable. Scripting skills are beneficial to implement user-defined demands or plug-ins for particular imaging conditions.

In this thesis, TLFM with microfluidic devices for *E. coli* single cell analysis and droplet generation are the central techniques in the publications presented in chapter [Results](#). For image processing and data extraction, customized software was developed by Korbinian Kapsner and Tiago Ramalho.

## 1.5. Bacterial communication

Bacterial chatter is of particular importance. Many infectious diseases, virulence and biofilm formation are facilitated by the information exchange of bacteria (157-161). The following section is an introduction to the elaborate molecular communication managed by bacteria.

### Quorum sensing – Diffusion sensing – Efficiency sensing

Quorum sensing (QS) is a mode of prokaryotic cell-to-cell communication widespread in gram-negative and gram-positive bacteria within and between species. Small molecules, called autoinducers (162) (AIs) are the membrane-passing transmitters. The message bacteria produce, send, read and respond by these chemical molecules enables them to monitor their environment in a cell-density dependent manner (163). Hence, the communication process was termed ‘quorum sensing’. In a typical QS circuit, the extracellular AI concentration accumulates with increasing cell population (2,164). Once, the signal molecules reach an internal threshold concentration, gene induction is activated by certain regulators and leads to high expression rates of QS-related genes and AIs. This executed positive feedback loop also alters the cellular behavior by switching the entire population into ‘quorum sensing mode’. Hence, QS is a powerful - and from the classical point of view - a social strategy to coordinate collective cellular interests among bacterial communities. Such common goods for instance are certain exoenzymes, cooperatively secreted for the digestion of difficult nutrients or the enhancement of group fitness in complex organic material (165). By the concerted action of QS, the production of protective extracellular matrices (166,167), certain antibiotics (168) or common chemotactic behaviors (169,170) are also achieved.

Well, bacterial populations in their natural environment are complicated and diverse. For instance, in early biofilm formation small groups of bacteria successfully colonize attractive surfaces such as plant roots or soil particles and rapidly form complex 3D aggregates despite continuously changing environments. Interestingly, in such an early stage of cell clusters of different sizes, AI-mediated cell-to-cell communication over long distances was observed (171). Also in confined space, single QS bacteria have been observed to achieve high-density behavior (172). Hence, under some circumstances, the spatial distribution of cells plays a more important role in QS than (true) cell density (173). However, QS is not only affected by spatial confinement but also by other environmental factors such as mass transport (diffusion or advection) and degradation or the presents of third party producers, cheater and cross-talk (QS interference (159)). Due to the fact of diffusion limitation in heterogeneous biofilms, Redfield proposed to interpret QS as ‘diffusion sensing’ (DS) process in which bacteria probe whether AI signal molecules diffuse rapidly away or are slowly enough that further AI secretion is efficient (174). This hypothesis spotlights the unsocial character of QS in which the direct fitness benefit is of individual interest.

However, the functional role and the notion of QS still remains controversial. In a recent computational study, Cornforth and colleagues demonstrate, that cells can simultaneously deduce both their social (density dependent) and physical (mass transfer based) environment by a combinatorial response to multiple signals of distinct half-life (175).

QS might not be a question of cooperative or non-cooperative behavior, but rather of what cells measure and why. Hense *et al.* proposed a well plausible hypothesis which does not contemplate both concepts QS and DS discretely, but rather encompasses both to the most appropriate interpretation of AIs signaling (173). According to Hense *et al.* bacteria use

AI as relevant information to estimate their efficiency. In other words, producing costlier effectors for the extracellular space or not. This efficiency sensing strategy can be of individual interest due to direct fitness benefit when effector production is optimized but does not exclude social aspects in appropriate situations concerning survival and growth. Nevertheless, keeping the alternative explanations in mind, the term quorum sensing will be usually used throughout this thesis.

### Chemical communication in synthetic biology

In contrast to natural ecosystems, synthetic biology commonly utilizes bacterial QS for the execution of artificial genetic programs between engineered cells. In a seminal work, Weiss and Knight first came up with the idea to separate the natural QS system of the seawater bacterium *Aliivibrio fischeri* into a 'sender' and 'receiver' unit (176). Based on this sender-receiver system, artificial intercellular communication was applied in many studies of outstanding interest:

For instance, to control the density of a bacterial population, QS was used to commence programmed cell death in *E. coli*. The implemented circuit coupled the signal molecule production and detection to the death rate induced gene expression leading to tunable cell densities (177). Other programmable cell systems use QS to activate and coordinate biofilm formation after the detection of damaged DNA (178), or only when two *E. coli* strains were present of which each owns a specific combination of a bidirectional quorum sensing system built up of LasI/LasR and RhII/RhlR components of *Pseudomonas aeruginosa* (179). An example for interkingdom communication between mammalian cells, bacteria, yeast and plants was shown by Weber *et al.* (180).

An autoinducer gradient was utilized to form programmed patterns such as ring-like structures and ellipses in a synthetic multicellular system (181). The core unit is based on engineered receiver cells that express different fluorescent proteins according to user-defined levels of signal molecules. Thus, the arrangement of both, sending and receiving bacteria lead to the desired spatial pattern. Further inspiring studies include the synthesis and degradation of autoinducer molecules, which have been linked to a fluorescent read-out, encoded on a rational engineered synthetic circuit. Such a system built the basis for synchronized oscillations in growing bacterial colonies over large distances in a microfluidic device (182,183).

### The diversity of signals

Nature evolved various chemical signals to communicate with each other. Many prokaryotes are able to use different signal molecules (recently reviewed in (184)) in parallel to channel information and to regulate diverse functions (185). Thus, different classes of autoinducer (AI) molecules exist. Some are species specific, others are used for interspecies communication such as autoinducer-2 (AI-2) molecules (186-188). A universal precursor for AI-2 sensing is DPD (4,5-dihydroxy-2,3-pentanedione) (189). The highly reactive molecule exists in different forms and modifications such as furanones (190). Each variation is identified by a particular bacteria species but rapidly interconverts into another. Hence, the recognition by other bacteria is facilitated (191). Interestingly, AI-2 are the most common autoinducers in bacteria identified to date (192), however, certain bacteria do not produce AI-2 type signals. Nevertheless, sensing the foreign compounds is part of their abilities as well as changing the gene expression pattern according to them (193).

Oligopeptides are mainly found in gram-positive bacteria (194,195). A prominent example for this type of cell-to-cell signal is derived from *Bacillus subtilis*. The competence-stimulating factor (CSF) is a pentapeptide, secreted into the medium and reimported by



oligopeptide permeases to regulated the competence pathway and sporulation process (196). Also oligopeptides which ask for plasmid conjugation in appropriate donor cells were identified (197).

In addition, quinolones, known for their antibiotic and anticancer properties are used as autoinducers by certain microorganisms such as *Pseudomonas aeruginosa*. Such an example highlights in particular the chemical diversity but also the multi-functionality of molecular communication in bacteria.

Autoinducer of class 1 (AI-1) include *N*-acyl-L-homoserine lactones (AHLs or acyl-HSLs). This cell-to-cell communication signals solely exist in gram-negative bacteria (198,199) and are commonly dedicated within a species.

The following sections deals with an introduction to their biosynthesis.

### AI-1 synthesis, release and response

AHLs are originally derived from *Aliivibrio fischeri*, a light-producing marine bacterium. The light emission of the symbiotic microbe is based on luciferase enzymes genetically encoded by the *luxICDABE* operon (163,200). The mechanisms regulating production, uptake, and response to these signal molecules are well-understood and briefly introduced in this section.

Chemically, AHLs are synthesized from *S*-adenosyl methionine (SAM) precursor, the source for the homoserine moiety (201). The acyl chains are supplied by an acylated acyl carrier protein (acyl-ACP) of the fatty acid biosynthesis pathway (202). The fundamental gene products required for the catalysis are LuxI-like proteins and homologs of the regulatory protein LuxR. This enzymes also comprise the LasI/LasR and RhII/RhlR system of *Pseudomonas aeruginosa* or TraI/TraR QS circuit of *Agrobacterium tumefaciens* for instance (reviewed in Miller and Bassler (163) and Papenfort and Bassler (184)). Followed by the interaction with SAM, the AHL synthase LuxI recognizes specifically acyl-ACPs of certain carbon chain length and reduction state (203). The first carbon of the acyl chain is then conjugated to the amino nitrogen on the methionine moiety of SAM to form an amide bond (204). A conserved threonine residue observed in many LuxI family proteins assigns specify for 3-oxo-ACPs (205) and directs the oxidation state of the third carbon of the acyl chain to 3-oxo-acyl HSL. Upon release of the apo-ACP, the lactonization of the intermediate homoserine ring leads to the final AHL product (206).

AHLs exist in different structures and show acyl chain length variations between 4-18 carbons (in an increment of 2), a varying degree of oxidation and different till extraordinary additional modifications such as coumaroyl moieties. Short chained AHLs freely diffuse through cell membranes (207) whereas AHLs with long, hydrophobic acyl chains such as the 3-oxo-C12 HSL of *Pseudomonas aeruginosa* require assisted transport into the cell by certain efflux pumps (208,209). Once in the cytoplasm, the signal receptor LuxR perceives, binds and activates the transcription of autoinducers by itself (200). The amino-termini of LuxR-type proteins recognize and envelops the cognate autoinducer molecule provided by LuxI synthases (210,211). Upon dimerization the protein is stabilized against proteolysis (187) and the helix-turn-helix DNA binding motif of the C-terminal domain stimulates together with RNA polymerase (212) the bidirectional transcription of the downstream *lux*-operon and *luxR* to increase the intracellular production of AI in response to the extracellular concentration.

The bacterial response to autoinducers is the activation or (in some circumstances) the repression of up to hundreds of QS related genes for various reasons (biofilm formation, scouting the environment or diverse social and unsocial tactics as mentioned in section QS.), but also the degradation of such molecules. Hence, bacteria evolved strategies that

degrade AHLs (213). The ability to interfere with bacterial QS is not surprising, since in natural environments, bacteria often compete with other species for space and resources. Such quorum quenching (QQ) strategies may be crucial for population survival or gives an advantage over other microbe species (214,215). For instance, an extremely efficient QS inhibitor is produced by *Bacillus subtilis*, a metallohydrolase called AiiA (216,217). The enzyme is secreted and cleaves the lactone ring from any acyl moiety of AHL that eliminates a wide range of chemical signals. Also eukaryotic hosts counteract bacterial QS to prevent colonization and virulence (218). Several natural and synthetic AI analogs such as furanones block LuxR-type proteins and cause their degradation (219-221).

The sender and receiver unit applied in this thesis is derived from the construction presented by Weiss and Knight (176) with additional optional degradation of the reporter fluorescence protein GFP by peptide tags recognized by the protein degradation system *ssrA* (153,154). The LuxI/LuxR system have been used to study communication and computation between populations of *E. coli* in a microfluidic device (6), compartmentalized into emulsion-based droplets (7) or with confined cell-free systems (11). The results of this studies are presented on the following pages.

## 2 Results

### 2.1. Single cell analysis of a bacterial sender-receiver system

A bacterial sender-receiver system based on the quorum sensing components LuxI/pluxR for AHL synthesis and detection was monitored at the single cell level.

We applied a customized microfluidic chemostat in which fresh nutrients permanently flow in and waste products out. The cells were trapped in chambers connected to the nutrient flow channel and monitored by fluorescence microscopy. The cells were equipped with green fluorescent protein (GFP) that reports about AHL levels. Videos obtained from time-lapse microscopy allowed the extraction of quantitative data by cell tracking and stochastic data analysis.

We determined bacterial lineages and report about gene expression dynamics and variability (gene expression noise) upon varying concentrations of AHL inducer molecules. We found the expression noise in the main population of our system is linked to extrinsic noise for high induction levels, while for low inducer concentrations the laws for extrinsic and intrinsic noise characteristics were not assignable to generic models of noise analysis. However, from the response curves of single cell trajectories we further extracted subpopulations of bacteria with classified, homogenous expression levels. Such subpopulations showed more cooperative response behavior (larger Hill exponent) compared to the heterogeneous entire population. We further determined the effective AHL concentration produced by sender bacteria based on the response curve data of an AHL-receiving bacterial sensor and mathematical modelling. These ‘sending power’ laid in the low nanomolar regime and was adjustable by the ratio of sender/receiver bacteria in the microfluidic chamber and is approximately proportional to  $t^2$  due to the influence of cell growth and AHL biosynthesis.

The following copy of the original research article (6) shows the above-summarized results in detail. Supplemental figures, tables and methods can be found in the [Appendix](#). For supplemental movies, please refer to the publishing journal.

## RESEARCH ARTICLE

# Single Cell Analysis of a Bacterial Sender-Receiver System

Tiago Ramalho<sup>1</sup>\*, Andrea Meyer<sup>2</sup>\*, Andrea Mückl<sup>2</sup>, Korbinian Kapsner<sup>2</sup>, Ulrich Gerland<sup>1,3</sup>\*, Friedrich C. Simmel<sup>2,3</sup>\*

**1** Physics Department, TU München, Garching, Germany, **2** Physics Department and ZNN/WSI, TU München, Garching, Germany, **3** Nanosystems Initiative Munich, Munich, Germany

\* These authors contributed equally to this work.

\* [gerland@tum.de](mailto:gerland@tum.de) (UG); [simmel@tum.de](mailto:simmel@tum.de) (FCS)



## OPEN ACCESS

**Citation:** Ramalho T, Meyer A, Mückl A, Kapsner K, Gerland U, Simmel FC (2016) Single Cell Analysis of a Bacterial Sender-Receiver System. PLoS ONE 11(1): e0145829. doi:10.1371/journal.pone.0145829

**Editor:** Michael M. Meijler, Ben-Gurion University of the Negev, ISRAEL

**Received:** October 27, 2015

**Accepted:** November 3, 2015

**Published:** January 25, 2016

**Copyright:** © 2016 Ramalho et al. This is an open access article distributed under the terms of the [Creative Commons Attribution License](https://creativecommons.org/licenses/by/4.0/), which permits unrestricted use, distribution, and reproduction in any medium, provided the original author and source are credited.

**Data Availability Statement:** Data are available in the paper and its Supporting Information files. Additional data have been deposited to the Leibniz Supercomputing Centre of the Bavarian Academy of Sciences and Humanities (<http://www.lrz.de/english/>). Raw video data that forms the basis of this study is available for download at (total size 32 GB): <https://syncandshare.lrz.de/d/fiMMwJkM8GHod3oXuWwWm3gxj.zip> A collection of compressed videos, in which bright field and fluorescence microscopy images were overlaid is available here (total size 465 MB): <https://syncandshare.lrz.de/d/fiPWxVaD4uw5NESj4Bkan2b1.zip>.

## Abstract

Monitoring gene expression dynamics on the single cell level provides important information on cellular heterogeneity and stochasticity, and potentially allows for more accurate quantitation of gene expression processes. We here study bacterial senders and receivers genetically engineered with components of the quorum sensing system derived from *Aliivibrio fischeri* on the single cell level using microfluidics-based bacterial chemostats and fluorescence video microscopy. We track large numbers of bacteria over extended periods of time, which allows us to determine bacterial lineages and filter out subpopulations within a heterogeneous population. We quantitatively determine the dynamic gene expression response of receiver bacteria to varying amounts of the quorum sensing inducer N-3-oxo-C6-homoserine lactone (AHL). From this we construct AHL response curves and characterize gene expression dynamics of whole bacterial populations by investigating the statistical distribution of gene expression activity over time. The bacteria are found to display heterogeneous induction behavior within the population. We therefore also characterize gene expression in a homogeneous bacterial subpopulation by focusing on single cell trajectories derived only from bacteria with similar induction behavior. The response at the single cell level is found to be more cooperative than that obtained for the heterogeneous total population. For the analysis of systems containing both AHL senders and receiver cells, we utilize the receiver cells as 'bacterial sensors' for AHL. Based on a simple gene expression model and the response curves obtained in receiver-only experiments, the effective AHL concentration established by the senders and their 'sending power' is determined.

## Introduction

Components of bacterial communication systems [1, 2] have been frequently utilized for applications in synthetic biology. In an early seminal work, Weiss and Knight [3] created artificial bacterial 'sender' and 'receiver' cells based on a quorum sensing (QS) system from the marine bacterium *Aliivibrio fischeri*, which is also utilized in this work. In this system, sender cells are equipped with the *luxI* gene from the *lux* operon coding for the autoinducer synthase LuxI.



**Funding:** This work was supported by European Commission FP7 (grant no. 248919 – BACTOCOM, [http://ec.europa.eu/research/fp7/index\\_en.cfm](http://ec.europa.eu/research/fp7/index_en.cfm)) and Deutsche Forschungsgemeinschaft (Cluster of Excellence Nanosystems Initiative Munich - NIM and DFG priority program SPP 1617, [www.dfg.de](http://www.dfg.de)). The funders had no role in study design, data collection and analysis, decision to publish, or preparation of the manuscript.

**Competing Interests:** The authors have declared that no competing interests exist.

LuxI catalyzes the synthesis of the quorum sensing signal N-3-oxo-C6-homoserine lactone (an acyl homoserine lactone, abbreviated AHL). AHL can diffuse through bacterial cell membranes and bind to LuxR activator proteins, which activate gene expression in receiver cells, from genes put under the control of  $P_{lux}$  promoters. In contrast to the natural QS system, in which all senders are also receivers, AHL is not utilized as an ‘autoinducer’ and there is no positive autoregulation of AHL production. Similar sender-receiver modules were already utilized in a wide variety of synthetic biology applications, e.g., in an artificial population control system [4, 5], for bacterial pattern formation [6, 7], synchronization of bacterial oscillators [8], bacterial edge detection [9], or distributed computing systems [10, 11].

In the context of synthetic biology, an important consideration is the reproducibility and robustness of synthetically generated behaviors. This is particularly challenging, as complex biological systems unavoidably display variability on various levels of organization. Over the past two decades it has become increasingly apparent that gene expression levels and their dynamics can vary considerably from one cell to another even in homogeneous colonies of genetically identical cells [12–17]. While this phenotypic heterogeneity was found to be the exception rather than the rule in a homogeneous environment [18], it is likely important for the survival of the colony in fluctuating environments. Mechanistically, the heterogeneity can be attributed to the intrinsic stochasticity of the processes involved in gene expression [19], in protein number fluctuations [20] and the noise generated by the unequal distribution of cellular components during cell division [21, 22], or other “extrinsic” factors.

The role of noise in the context of quorum sensing was previously analyzed theoretically, where in particular the impact of population feedback [23] and diffusion of the signals [24] was investigated. Diffusive coupling of the cells was surmised to lead to an overall reduction of extrinsic gene expression noise in the cells [24]. On the experimental side, quorum sensing was investigated on the single-cell level in *V. harveyi* bacteria, which communicate via two distinct autoinducer signals [25]. Noise was characterized for several reporter strains and found to be extrinsic in nature. An alternative approach was demonstrated in [26], where protein level fluctuations were analyzed using correlation functions on the microcolony level rather than based on single cell data.

In contrast to previous work, we here focus specifically on an artificial sender-receiver system as typically used in synthetic biology applications. Based on fluorescence microscopy experiments [27] with bacterial cells growing in microfluidic chemostats [28, 29], we first study gene expression dynamics of a QS-derived ‘receiver module’ implemented in *E. coli*. We show that single cell data can be used to determine the quantitative input-output characteristics for the AHL/ $P_{lux}$  system, which agree with data generated using bulk methods. We then analyze individual single cell gene expression time courses, which display a considerable heterogeneity compared to the bulk data. From these we extract statistical distributions of gene expression rates in the bacteria, and identify sub-populations with different induction behavior. In our analysis, we first follow the time-course of the gene expression rate distribution of the whole population. By tracking individual cell lineages, we then restrict the analysis to the sub-population of the bacteria with the dominant induction state, which results in a more accurate estimate of gene expression rates and the corresponding quantitative single cell input-output characteristics.

Finally, we apply our analysis procedure to a synthetic sender-receiver system [3, 11], in which the AHL signals are produced *in situ* by dedicated sender bacteria. In order to be able to determine AHL concentration within the chambers, we utilize the highly sensitive receiver cells themselves as AHL bioreporters [30]. Using a simple model of gene expression in sender and receiver bacteria, we can deduce the effective AHL concentration established by the bacteria in the microchambers, which falls in the low nanomolar range for our experimental setup. We

show that the effective AHL concentration scales with the average sender/receiver ratio in the chamber and rises  $\sim t^2$  with time.

A similar analysis could help to provide a quantitative experimental basis for the ongoing debate about the evolutionary origins of QS [31, 32]. The question is centered around whether the autoinducer is really a social signal to other cells, or instead simply a single cell mechanism to measure effective diffusion in the local environment. This distinction is relevant in the context of heterogeneous colonies, where different individuals may evolve to respond differently to the autoinducer—if some contribute external molecules which benefit all cells while others do not, then ‘cheaters’ can have a growth advantage. The analysis approach established here for the synthetic sender-receiver system will be useful to quantitatively characterize the QS behavior by controlling effective AHL diffusion as well as population sizes.

## Materials and Methods

### Plasmids

All experiments were performed with genetic constructs derived from the *Aliivibrio fischeri* bacterial quorum sensing system (cf. Fig A in S1 File). Receiver plasmids contained the *luxR* gene under control of the TetR repressed promoter  $P_{tet}$  and the *gfpmut3b* gene [33] controlled the *lux* promoter  $P_{lux}$  (BioBrick part BBa\_T9002) on vector pSB1A3. In the absence of TetR, LuxR was constitutively expressed from this plasmid. To construct the sender plasmids, the gene for LuxI synthase (BioBrick part BBa\_C0261) was cloned into a pETDuet-1 expression vector (Merck Millipore) inserted between the BioBrick cloning sites XbaI and PstI. Expression from this vector is driven by T7RNAP, which is produced by the compatible host strain *E. coli* BL21(DE3)pLysS after IPTG induction. As a fluorescent reporter, an additional *rfp* gene (derived from BioBrick BBa\_E1010) was cloned between the NdeI and PacI restriction sites of the plasmid. A complete description of the construction of the plasmids including their sequences can be found in a previous publication [11]. Receiver and sender cells were created by transforming the corresponding plasmids into *E. coli* BL21(DE3)pLysS using an Electroporator (ECM399, BTX Harvard Apparatus, Holliston, MA, USA).

### Bacterial cell culture

Experiments were performed with the *Escherichia coli* strain BL21(DE3)pLysS (Promega, Fitchburg, WI, USA). Cells were grown in 10 ml Luria-Bertani (LB) medium (Carl Roth, Karlsruhe, Germany), containing 100  $\mu$ g/ml Carbenicillin (AppliChem GmbH, Darmstadt, Germany) and stored for 4 hours in a shaker (Innova 44R, New Brunswick scientific, Edison, NJ, USA) at 37°C and 250rpm. After 4 hours, the OD600 typically was between 1.0 and 1.5. The OD600 was then adjusted to 1.0 with fresh LB medium. 10 ml of the culture were centrifuged for 5 minutes at 7000 rcf. The supernatant was decanted and the remaining pellet was resuspended with 1 ml LB medium for the microscopy experiment and 10 ml LB medium for plate reader measurements.

### Plate reader experiments

Bulk characterization of gene expression activity was performed in a FLUOstar Omega plate reader (BMG, Ortenberg, Germany). A 96-well plate (ibidi, Martinsried, Germany) was prepared by combining 30  $\mu$ l of a 10 X AHL stock solution (corresponding to the desired 1 X concentration) and 240  $\mu$ l LB medium. 30  $\mu$ l of bacterial suspension in LB were added directly before the experiment was started. Fluorescence and optical density were measured every 5 minutes for 15 hours. Between two consecutive measurements the plate was shaken with



1100 rpm. To prevent evaporation a gas permeable laminate (Carl-Roth GmbH, Karlsruhe, Germany) was bonded onto the plate. Fluorescence was excited at  $\lambda_{exc} = 485$  nm for excitation and detected at  $\lambda_{em} = 520$  nm. The absorbance of the cell suspension was measured at 600 nm. Cells were initially diluted to an absorbance of  $OD_{600} = 0.1$ , and inducer was added at concentrations ranging from 0 nM to 100 nM. AHL did not have any observable influence on bacterial growth during exponential phase, while it slightly affected the saturation level. Bacterial cultures appeared to grow to higher densities at higher inducer concentration.

### Microfluidic chemostats

Microfluidic chemostats consisted of bacterial traps ( $100 \mu\text{m} \times 60 \mu\text{m} \times 1 \mu\text{m}$ ) connected to microfluidic supply channels ( $\text{width} \times \text{height} = 100 \mu\text{m} \times 15 \mu\text{m}$ ), similar to those previously described in Ref. [8]. AHL concentrations were varied using a microfluidic gradient mixer adopted from [34]. A schematic design of the microfluidic device is shown in Fig B in [S1 File](#). The chemostats were fabricated using standard soft lithography procedures. A lithographic master was first defined by photolithography on a silicon wafer using the negative resists Epo-Core 20XP (micro resist technology, Berlin) and AZ-nLOF 2070 (Microchemicals, Ulm, Germany). Channels and traps were defined separately in two consecutive steps. The microfluidic channels were then molded in the elastomer Polydimethylsiloxane (PDMS) (Sylgard 182, Dow Corning, Senefte, Belgium). After baking for 2 h, PDMS and a microscopy cover glass slide were sonicated for 10 minutes in 2/3 isopropanol and 1/3 ddH<sub>2</sub>O, followed by exposure to an oxygen plasma in a plasma cleaner (Femto, Diener electronic, Ebhausen, Germany) for 1 minute, after which the PDMS was bonded to the glass. Calibration measurements using fluorescent buffer solution (cf. Fig C in [S1 File](#)) showed correct performance of the gradient mixer with a relative precision in the concentrations of  $\pm 20\%$ .

For the experiments, bacterial suspension was flushed through the microfluidic system until single or few bacteria were captured in the traps. After trapping, bacteria were constantly supplied with nutrients (LB medium) using a syringe pump with two syringes at a speed of  $2 \times 80 \mu\text{l/h}$ . For the titration experiments, AHL (N-3-oxo-C6-homoserine lactone, Sigma Aldrich, Taufkirchen, Germany) was added to the medium to achieve the desired concentrations after passing the microfluidic mixer. The bacterial growth rates in the microfluidic chambers ranged from  $\mu \approx 0.36 \text{ h}^{-1}$  up to  $\mu \approx 1 \text{ h}^{-1}$ , independently of the inducer concentration.

### Fluorescence Microscopy

Time-lapse microscopy was performed on an automated fluorescence microscope (IX81, Olympus, Tokyo, Japan) equipped with a ZDC2 laser autofocus system and a motorized x-y-stage (Scan IM, Maerzhaeuser, Wetzlar, Germany). The microscope was enclosed in a cage incubator (okolab, Ottaviano, Italy) and held at a constant temperature of 37°C. Brightfield and fluorescence images were acquired every 3 minutes for 15 hours with an emCCD camera (iXon3 888, Andor, Belfast, UK) through an oil-immersion 100x objective (UPlanSApo 100x, Olympus, Tokyo, Japan) with acquisition times of 0.2 seconds, and all devices were controlled via CellSense software (Olympus, Tokyo, Japan). Fluorescence was excited by an x-cite 120 lamp (EXFO, Quebec, Canada).

### Image analysis and extraction of single cell data

A detailed description of the image processing procedures is found in [S1 File](#). In brief, microscopic images are first preprocessed by applying contrast enhancement, noise reduction, and sharpening algorithms (Fig D in [S1 File](#)). As a second step, each pixel is classified as belonging to a cell or not, based on a hybrid method: global brightness, adaptive local brightness and an

adaptive masking method (adapted from Wang et al. [35]) each contribute to the classification of a pixel as 'cell area' or 'image background'. After removal of the background pixels, cell markers are created by a multi-step process. First, connected regions of cell area pixels are assigned to a shared marker. These regions are then broken down based on edge information, brightness, and cell geometry until all regions have dimensions consistent with the cell type. The resulting regions are refined using the watershed algorithm. Spurious results may be removed by filtering regions by size and via the use of a classifier. We use a support vector machine (SVM) as classifier, which has previously been used to distinguish cell phenotypes with success [36]. The classifier is trained by the user via a graphical user interface (GUI). Finally, cells are tracked in time using a maximum-overlap method. This method compares cell labels in two adjacent frames and calculates their overlap. For each cell in the later frame, the cell with maximum overlap in the previous frame is assigned as its parent, and cell lineages can be constructed from the data (Fig E in S1 File). The user can correct tracking assignments via the GUI.

### Data analysis

In plate reader experiments, the time-dependent optical density (OD600) is taken as a proxy for the total cell mass,  $M(t)$ . Together with the fluorescence  $F(t)$  the expression rate  $\alpha$  is calculated via

$$\alpha \sim \dot{F}/M. \quad (1)$$

This proportionality holds for expression of a stable fluorescent protein during exponential growth of the bacteria: In exponential growth, the total mass grows according to  $\dot{M} = \mu M$ , while the number of fluorescent proteins  $p$  per bacterium follows  $\dot{p} = \alpha - \mu p$ , which assumes that protein concentration is only diluted by bacterial growth. Since  $p \sim F/M$ , one has

$$\frac{d}{dt} \frac{F}{M} = \frac{\dot{F}}{M} - \frac{\dot{M}F}{M^2} = \frac{\dot{F}}{M} - \mu \frac{F}{M}, \quad (2)$$

and thus

$$\frac{\dot{F}}{M} = \frac{d}{dt} \frac{F}{M} + \mu \frac{F}{M}, \quad (3)$$

which is proportional to  $\dot{p} + \mu p = \alpha$ . In plate reader data analysis, we took the maximum of  $\dot{F}/M$  during exponential growth as an approximate measure for  $\alpha$ . In microfluidic experiments, the area  $A$  occupied by the cells takes the role of the cell mass/absorbance in the bulk experiments and thus  $\alpha \sim \dot{F}/A$ .

## Results and Discussion

### Gene induction by AHL—population average

We first characterized the average gene expression response of our receiver cells using standard plate reader experiments. Receiver cells constitutively expressed LuxR and thus, in the presence of the QS inducer AHL, produced the fluorescent reporter protein GFPmut3 (Fig A in S1 File). Experiments with varying inducer levels ( $[AHL] = 0 - 100$  nM) were used to deduce the response curve of the bacteria, which was well fit by a Hill function with Hill exponent  $n = 0.97 \pm 0.08$ . The AHL concentration required for half induction was obtained from the fit as  $K = 13.9 \pm 1.7$  nM (cf. Fig F in S1 File). These parameters are consistent with previous



quantitative analyses of the AHL/ $P_{lux}$  system, which have typically resulted in Hill exponents around  $n = 1 - 1.5$  and induction thresholds in the range  $K = 5 - 15$  nM [25, 37–39].

Using time-lapse fluorescence microscopy [27], we then recorded the response of growing populations of receiver bacteria within microfluidic bacterial chemostats similar to those previously described in [8] (see Methods and Fig B in S1 File). In these structures, bacterial cells are captured in shallow microchambers of dimensions  $100\ \mu\text{m} \times 60\ \mu\text{m}$  and  $\approx 1\ \mu\text{m}$  height, which only allow cell growth in a single layer. The microchambers are connected to larger microfluidic supply channels, which continuously provide fresh medium and remove waste products from the chambers. As a result, bacteria can grow in the chambers in exponential phase over extended periods of time.

In the experiments, we recorded bright field (BF) and fluorescence images of growing bacterial populations over a timespan of typically 15 h with a temporal resolution of 3 minutes. The microscopy images were then analyzed using a custom-written image analysis software package, which is described in detailed in the Supporting Information (Text A in S1 File). We first used the extracted data to determine the colony average of all observables, permitting us to compare the average response in the microfluidic chemostats to the bulk response measured with the plate reader. Fig 1A shows the time-dependent total area  $A(t)$  of all cells in a microcolony for different external AHL concentrations, while Fig 1B shows the total integrated fluorescence  $F(t)$  for a colony. Since the total area is a proxy for total cell mass, the average gene expression activity  $\alpha$  for the microfluidic experiments can be defined as  $\alpha = \dot{F}/A$ . Taking  $\alpha_{\text{max}}$

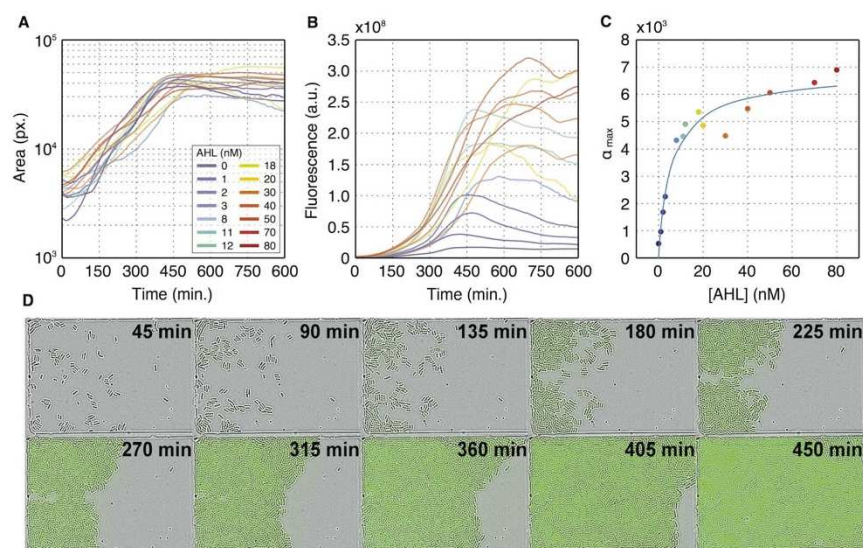


**Fig 1. Bulk analysis of gene expression in microfluidic chemostats.** (A) Total cell area  $A$  in pixels as a function of time for acquisitions with different AHL concentrations. The cells are in exponential growth for at least 450 min. After this time, the bacteria completely fill the microfluidic traps and the measured area stays constant. (B) Total colony fluorescence  $F$  as a function of time. (C) Maximum gene expression rates calculated as  $\dot{F}/A$  (cf. Eqs 1–3). The solid response curve is a Hill fit to the data with  $n = 0.95 \pm 0.2$  and  $K = 5.3 \pm 1.4$  nM. (D) Snapshots taken from a time-lapse microscopy video of a bacterial colony growing in a microfluidic trap, which is connected to a supply channel on the right. The images shown are overlays of bright-field and fluorescence data. In the example, the bacteria were induced with 12 nM AHL.

doi:10.1371/journal.pone.0145829.g001

from each curve, we can construct the average response of the AHL/ $P_{lux}$  system (Fig 1C). In this case, the Hill function fit leads to a cooperativity exponent of  $n = 0.95 \pm 0.2$  and half activation at  $K = 5.3 \pm 1.4$  nM. The Hill exponent thus agrees well with the one extracted from the bulk experiment, while the induction threshold  $K$  is somewhat lower in our microfluidic device. This difference could be caused by the different physiological state of the bacteria in the microfluidic environment, e.g., their significantly lower growth rate compared to the bulk experiment. Additionally, the microfluidic setup may introduce a small deviation between the expected and actual local AHL concentration (Fig C in S1 File).

### Analysis of gene expression variability

We next characterized the stochastic response of the AHL/ $P_{lux}$  system by extracting time-dependent histograms of fluorescence levels from our data. Fig 2A shows an example for such a time-dependent histogram where the cells were induced with 50 nM AHL. Note that in this analysis the identity of the individual cells is not followed. From a theoretical perspective, this characterization of the gene expression dynamics corresponds to the Fokker-Planck description of stochastic systems in terms of a time-dependent probability distribution, in contrast to the Langevin description in terms of stochastic trajectories (see below).

In order to display the entire range of expression levels, we plot the fluorescence per cell area in Fig 2A on a logarithmic scale. A single time slice, taken at the late time point  $t = 600$  min, is displayed in Fig 2B. The Gaussian fit to the main peak (green line) shows that the dominant part of the gene expression histogram is well described by a Gaussian distribution on the logarithmic axis, which corresponds to a lognormal probability distribution for the expression level. Theoretically, a lognormal distribution is expected to be a good description for a biological quantity that is determined by several independent kinetic rates. For instance, if the steady-state concentration  $p$  of a protein is determined by the rates of mRNA synthesis,  $\alpha_r$ , and degradation,  $\lambda_r$ , as well as the translation rate  $\alpha_p$  and the rate of protein degradation  $\lambda_p$  via  $p = \alpha_r \alpha_p / \lambda_r \lambda_p$ , and the statistical variations of these rates from cell to cell are not strongly correlated, then the central limit theorem can be applied to the logarithm of this expression [40, 41]. The theorem states that the limiting distribution obtained for many different rates is the lognormal distribution, but in practice the distribution will already be very close to lognormal even when only a couple of rates are involved, as in this example where  $p$  is determined by four rates.

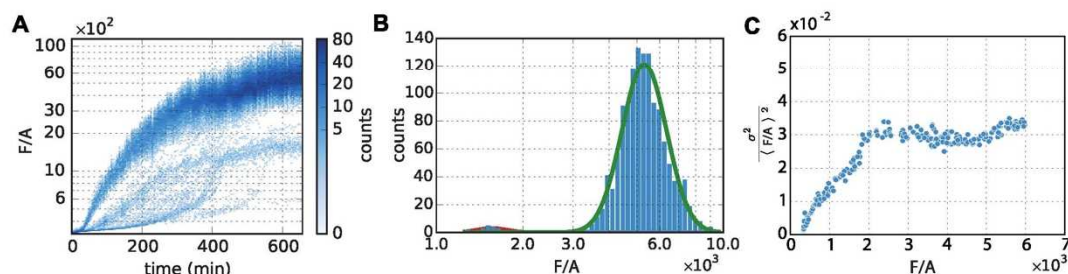


**Fig 2. Single cell gene expression histogram and trajectories for AHL = 50 nM.** (A) Evolution of the bacterial fluorescence per area  $F/A$  as a function of time. Clusters of 'late inducers' are visible. (B) Histogram of  $F/A$  at time  $t = 600$  min using a logarithmic scale on the x-axis. Solid lines represent the two Gaussian distributions resulting from the Gaussian mixture fitting procedure used to separate out the dominant, homogeneous fraction of cells. (C) Parametric plot of the square of the coefficient of variation (CV) of  $p = F/A$ , i.e.,  $\sigma_p^2 / \langle p \rangle^2$ , as a function of  $\langle p \rangle$ . The noise is dynamically ramping up until the cells reach roughly 1/3 of their maximal expression level. After this,  $CV^2$  stays approximately constant, indicating the dominance of extrinsic noise in gene expression.

doi:10.1371/journal.pone.0145829.g002



Previously, a variety of distributions for gene expression variability have been theoretically derived [19, 20, 42–44] from different assumptions for the underlying noise process, including the negative binomial and the Gamma distribution, which are empirically hard to distinguish from the lognormal distribution [41].

Whereas the dominant part of the distribution in Fig 2B is well described by the lognormal distribution, there are evidently other contributions at lower expression values. The time-dependence of this contribution is visible in Fig 2A and suggests that the population contains a small group of bacteria, which respond much later and less strongly than the majority. We hypothesized that this fraction of cells is in a different physiological state, which appears consistent with the observation that the number of these cells does not grow significantly in contrast to the cells in the dominant part of the distribution, see Fig 2A. We therefore separated out these slow-growing ‘late-inducers’ from the dominant induced population using a Gaussian mixture model for the logarithm of the expression data (in Fig 2B, this is shown by the red and green lines). This procedure allowed us to extract, at each time point, the mean and variance of gene expression within the dominant part of the cell population, which appears to be homogeneous in its physiological state.

We next analyzed the noise characteristics within the dominant cell population (Text B in S1 File). From the mean,  $\langle p \rangle$ , and the variance,  $\sigma_p^2$ , of protein expression, we calculated the fractional noise  $\sigma_p^2/\langle p \rangle^2$ , which corresponds to the square of the coefficient of variation  $CV = \sigma_p/\langle p \rangle$ . This is plotted in Fig 2C against the mean expression level. Note that Fig 2C is a parametric plot, where both the fractional noise and the mean are functions of time. It indicates that  $\sigma_p^2/\langle p \rangle^2$  is approximately constant after reaching about one third of the maximal expression, i.e. from this point on the standard deviation increases proportional to the mean. The obtained  $CV \approx 0.17$  is about half of that obtained previously for *V. harveyi* autoinducer reporter systems [25]. The scaling of the fractional noise with the mean is often used to distinguish between intrinsic and extrinsic noise contributions. A recent high-throughput study with *E. coli* suggested that generally intrinsic noise is dominant at low expression levels, while extrinsic noise is dominant at high expression levels [45]. Our observation of constant fractional noise at high expression levels is consistent with the scaling expected for extrinsic noise.

At expression levels below one third of the maximal expression, the fractional noise in Fig 2C is not constant but increases roughly linearly with the mean. This behavior is neither consistent with extrinsic noise nor with intrinsic noise, which would predict a fractional noise that decreases with the mean. Strictly speaking, the scaling laws for intrinsic and extrinsic expression noise only apply to the steady-state, while the increasing regime of Fig 2C corresponds to the time period during which gene expression is dynamically ramping up. Nevertheless, the increasing fractional noise appears somewhat surprising given that existing models for time-dependent noisy gene expression [44] rather display a decrease in the fractional noise as the mean expression level rises. However, the precise stochastic dynamics of the initial induction process likely depends on many details including the dynamics of the reporter system, and it is unclear whether this period leads to any generic features that can be captured by a simplified mathematical model. In contrast, the last two thirds of the induction process nicely follow the generic extrinsic scaling.

### Extraction of response curves from single cell trajectories

Up to now, we characterized the induction response of our bacteria only on the colony level. We first focused on the temporal evolution of the mean gene expression (Fig 1), and then determined the statistical variation of gene expression levels within the population (Fig 2). The

latter analysis demonstrated that the population is in fact quite heterogeneous, and thus the response of individual cells potentially could be different from the mean behavior.

We therefore tracked the gene expression dynamics of individual cells and determine the response curve of a single homogeneous subpopulation (for Details on Video Analysis cf. Text A in S1 File) and the establishment of Single Cell lineages (Fig E in S1 File)). In order to filter out cells with a specific induction behavior, we classified cells via their expression level at the end of the experiment and excluded trajectories of all cells outside of the targeted subpopulation. From the fluorescence time traces we then calculated the full temporal dynamics of the production rate  $\alpha$  for each cell. As before, we utilized the maximum of this value ( $\max_t \alpha(t)$ ) as a measure for the induction level of the cells. As an alternative measure, we also calculated the mean production rate  $\langle \alpha(t) \rangle_t$  for each cell.

In Fig 3 we compare the distributions obtained for each observable, which are both fit well by a lognormal distribution. We extracted the average and standard deviation of these distributions as a function of AHL concentration. This allowed us to plot induction response curves

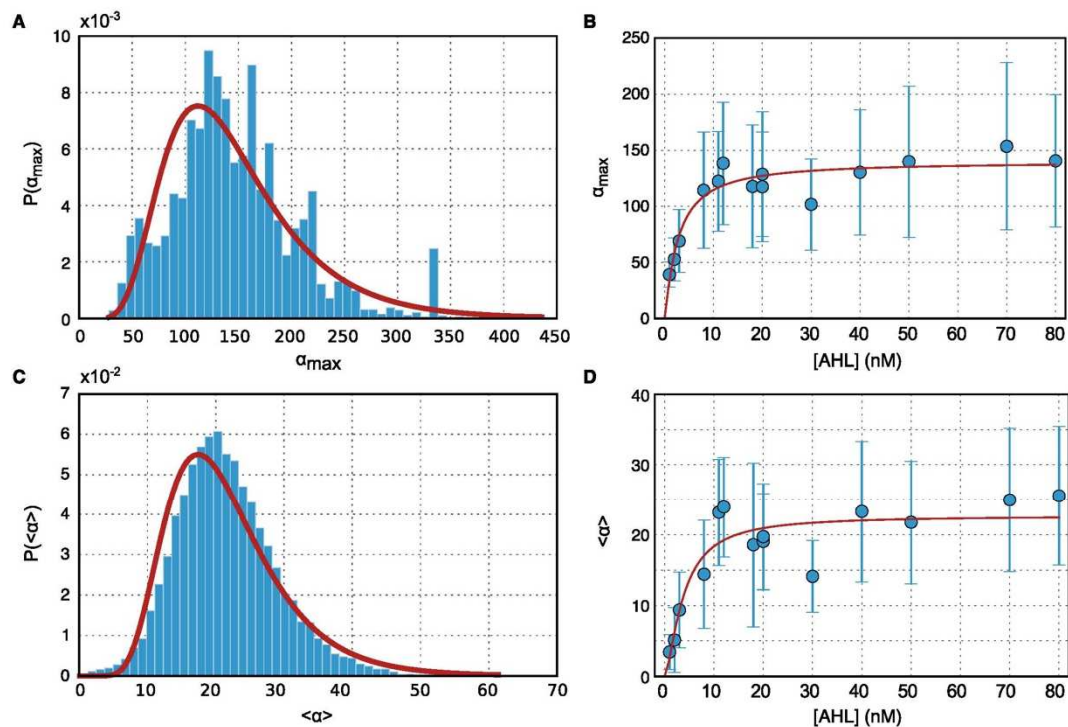


**Fig 3. Distribution of gene expression rates  $\alpha$  determined from single cell trajectories.** (A) Histogram of the maximum gene expression  $\alpha_{\max} = \max_t \alpha(t)$  for each single cell trajectory (AHL = 50 nM), and a lognormal MLE fit to  $P(\alpha_{\max})$  (red line). (B) Plot of the average and standard deviation of the distribution  $P(\alpha_{\max})$ . The red line is a regression curve generated by fitting a Hill function to the data. (C) Histogram of the average expression  $\langle \alpha(t) \rangle$  for each single cell trajectory (AHL = 50 nM) and a lognormal MLE fit to  $P(\langle \alpha(t) \rangle)$ . (D) Plot of the average and standard deviation of the distribution  $P(\langle \alpha(t) \rangle)$ —the red line represents the best fit with a Hill curve.

doi:10.1371/journal.pone.0145829.g003



such as in Fig 1C, but now based on single cell data—and with error bars. For  $\max_t \alpha(t)$ , a fit with a Hill curve results in  $K = 2.7 \pm 0.6$  nM and  $n = 1.2 \pm 0.3$ , while for  $\langle \alpha(t) \rangle_t$  we obtain values of  $K = 3.8 \pm 1.2$  nM and  $n = 1.5 \pm 0.6$ .

The latter values thus represent the induction threshold and Hill exponent obtained from the average expression rates of single bacteria belonging to a single subpopulation, and should therefore be the ‘most reliable’ estimate of these parameters for our system. While the obtained values are in agreement with those fit to the bulk response curve (Fig 3C) within statistical error, we observe that the predicted response is at a higher cooperativity and lower threshold. This is consistent with the fact that the late inducer population effectively lowers the observed average fluorescence per mass unit, resulting in a (predicted) more gradual response curve in the bulk case. Focusing only on quickly induced cells we obtain a sharper response, suggesting that the heterogeneity in the population smoothes out the response curve.

### Quantification of AHL concentrations in a sender-receiver system

We next attempted to quantify the chemical communication between bacterial sender and receiver cells within the microfluidic chambers (Fig 4). While receiver cells were the same AHL sensing bacteria as described above, sender cells were equipped with a plasmid containing a gene for LuxI, an AHL-synthase, and red fluorescent protein (RFP) as a fluorescent marker. Thus the sender cells were capable of locally producing a QS signal, which can spread into the microfluidic environment and induce GFP expression in the receiver cells. We performed a series of experiments, in which we loaded small numbers of senders and receivers into chemostat microchambers at varying initial ratios  $r$ , and monitored their growth and communication using time-lapse microscopy as before.

A quantitative analysis of these sender-receiver experiments is complicated by a variety of issues. First, there is no simple sensor available for *in situ* sensing of AHL except for the receiver bacteria as ‘cellular sensors’ themselves. Furthermore, both the senders and receivers are growing and dynamic, and thus at any given time the signal output depends on the history of the system and the specifics of the experiment (such as sender/receiver ratio  $r$ , growth and expression rate). In order to determine the effective AHL concentration (or ‘sender strength’) for each experiment individually, we therefore have to resort to a model of gene expression dynamics in the system.

In the model, the production of the AHL synthase LuxI is described by

$$\frac{d}{dt} [\text{LuxI}](t) = \alpha_l r N(t) - \lambda [\text{LuxI}](t). \quad (4)$$

Here  $\alpha_l$  is the LuxI production rate,  $N$  is the total number of receiver bacteria and  $[\text{LuxI}]$  is the mean concentration of LuxI molecules in the microfluidic chamber at time  $t$ . The rate  $\lambda$  accounts for degradation/dilution of LuxI, and  $r$  is the sender/receiver ratio, which can be different in each experiment and due to cell division may vary over time. AHL is then produced from LuxI with rate  $\alpha_a$  and distributes within the chamber through diffusion. We further neglect AHL decay, but assume a constant outflow from the chamber proportional to  $C$ :

$$\frac{d}{dt} [\text{AHL}](t) = \alpha_a [\text{LuxI}](t) - C [\text{AHL}](t) \quad (5)$$

In the exponential growth phase—when  $N(t) = N_0 e^{rt}$ , the above equations can be solved for  $[\text{AHL}]$  analytically. For small enough growth, degradation, and dilution rates ( $\gamma, \lambda, C$ ), the resulting expression for the concentration  $[\text{AHL}]$  at time  $t$  can be approximated by  $[\text{AHL}](t) \simeq 1/2 \alpha_a \alpha_l r N_0 t^2$  (cf. Text C in S1 File). Intuitively, this can be understood as follows: at any

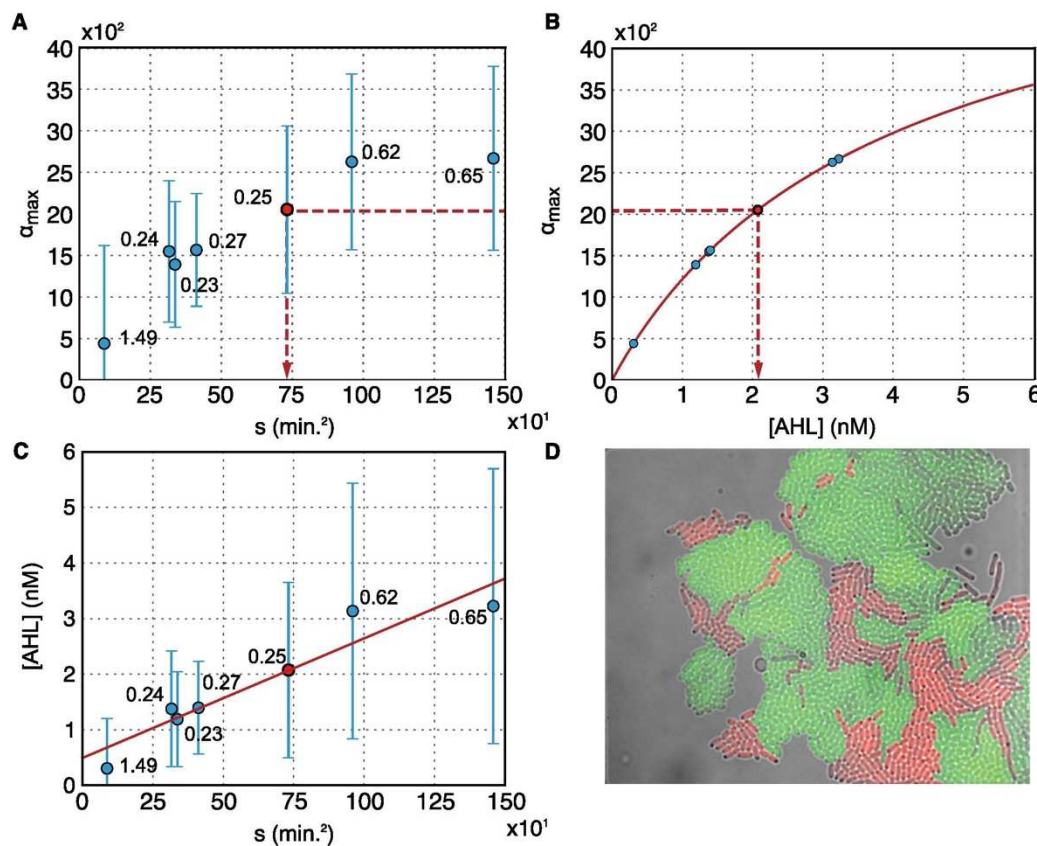


**Fig 4.** (A) Maximum GFP induction for 7 select experiments as a function of the effective AHL production constant  $s = \langle r \rangle t_{\max}^2$ . The sender strength parameter  $s$  in the experiments was varied via the sender/receiver ratio  $r$ . Nominally, the initial ratios were chosen to be  $r = 0.067, 0.142, 0.33$ , and  $1$  (corresponding to sender fractions of 6.25%, 12.5%, 25%, and 50%, resp.), but due to cell division and dynamics within the bacterial traps, the ratios varied over time—the resulting average ratios ( $\bar{r}$ ) are indicated for the single data points. Error bars represent standard deviations obtained from single cell gene expression histograms as in Fig 3. (B) Determination of effective AHL concentration for the 7 experiments using the calibration curve acquired in the ‘receiver only’ experiments with constant  $[\text{AHL}]$ . (C) The parameter  $s$  and the effective AHL concentration in the traps can be related as indicated by the broken lines in part A and B of the figure (for the red colored example point). A linear fit to the data following Eq (6) is shown as a red line, error bars are obtained from the standard deviations in (A) via error propagation. (D) Example image of a microfluidic trap containing sender (red) and receiver (green) bacteria.

doi:10.1371/journal.pone.0145829.g004

time  $t$  there will be a number of sites producing AHL proportional to  $t$  (due to population growth). Integration with respect to time results in a total AHL production in the chamber proportional to  $t^2$ . The proportionality constant ( $\alpha_a \alpha_l r N_0 / 2$ ) depends on the AHL and LuxI production rates and the initial sender population size.

The sender-receiver ratio  $r$  and the times  $t$  at which AHL concentration is measured are not constant from experiment to experiment. For each experiment we therefore fix the measurement time  $t$  to be the time at which senders are maximally induced ( $t_{\max}$ ), and the sender-receiver ratio is estimated by averaging  $r(t)$  in the interval  $[0, t_{\max}]$ . In order to be able to

compare different sender-receiver experiments, we bundle these experimental parameters into the variable  $s = \langle r \rangle t_{\max}^2$ . This procedure allows us to set up a calibration curve that relates the parameter  $s$  to the effective amount of AHL in the chamber:

$$\text{AHL}_{\text{eff}}(s) = \frac{1}{2} \alpha_n \alpha_t N_0 s \quad (6)$$

Under the assumption that AHL diffuses quickly through the microchamber (estimates for its diffusion coefficient  $D$  are in the range from 100 to 1000  $\mu\text{m}^2/\text{s}$  [9, 46–48]) such that each cell is exposed to the same concentration [AHL], the GFP expression rate of the receiver cells is given by:

$$\alpha \equiv \frac{d}{dt}[\text{GFP}](t) = \alpha_s \frac{[\text{AHL}]^n(t)}{[\text{AHL}]^n(t) + K_g^n}, \quad (7)$$

where  $n$  and  $K_g$  are the Hill exponent and threshold for AHL induction determined above.

We can now match any experimentally determined GFP expression rate  $\alpha$  to a parameter  $s$  characterizing each experiment (Fig 4B). At the same time,  $\alpha$  can be matched to an effective AHL concentration via Eq (7) (Fig 4C). As explained in Fig 4D, this also establishes a relationship between AHL and the parameter  $s$ , which can be used to characterize the sender strength of the sender bacteria according to Eq (6). In practice, we might want to determine the ‘effective’ AHL concentration in a sender-receiver experiment, compare data from two different experiments, or we might ask whether two experiments are comparable at all. Our results indicate that this could be done using a similar procedure as that detailed above, i.e., via determination via a parameter  $s$  that depends on the sender ratio in the population and grows *quadratically* with time.

## Conclusions

We have quantitatively studied gene induction by the diffusible quorum sensing inducer N-3-oxo-C6-homoserine lactone in genetically modified receiver bacteria, in which the expression of green fluorescent protein was put under the control of the quorum sensing promoter  $P_{\text{lux}}$ . In order to characterize gene expression dynamics on the single cell level, we performed experiments in microfluidic chemostats and monitored bacteria by fluorescence video microscopy. Using customized image analysis software, we were able to track large numbers of bacteria over extended periods of time, determine bacterial lineages and filter out subpopulations within a heterogeneous population.

We then quantitated the single cell response of bacteria to varying amounts of inducer using different methods. We followed the temporal evolution of the full statistical distribution of gene expression activities in bacterial populations, which allowed us to identify several subpopulations of bacteria with distinct induction behavior. Response curves derived from the mean behavior of the microchamber populations agree well with those obtained in bulk gene expression, except for a lower induction threshold which is attributed to the different growth conditions in the chemostat. We also constructed response curves from single cell trajectories, which enabled us to focus on the dominant sub-population with homogeneous induction behavior. Analysis of this homogenous, major sub-population resulted in a slightly steeper response to the autoinducer (larger Hill exponent) than for the whole population. Small numbers of cells appeared to respond much later to added AHL, which could be attributed to a strongly reduced growth rate. Gene expression noise in receiver bacteria was found to be extrinsic in nature, consistent with previous studies of other bacterial communication systems. Somewhat surprisingly, the coefficient of variation was found to dynamically ramp up in the initial (non-steady



state) phase of growth in the chamber, but remained constant after approximately 1/3 of the maximum gene expression was reached.

We also applied our methodology to the characterization of bacterial microchambers containing both AHL senders (expressing the autoinducer synthase LuxI) and receivers, where we used the receivers themselves as highly sensitive bioreporters for AHL. Based on a simple gene expression model of the sender-receiver system and the response curves obtained in the receiver-only experiments, we were able to determine the effective AHL concentration established by the senders in the microchambers, and also assign an effective 'sender strength' to them. The sender strength can be adjusted by the sender/receiver ratio in the chambers, but due to statistical fluctuations this ratio can fluctuate over time and vary from experiment to experiment. In addition to this ratio, the effective AHL concentration in a chamber is approximately proportional to  $t^2$ , which is due to the combined effect of sender cell growth and simultaneous AHL production.

Taken together, we quantified both the response of the receiver cells as well as the emitting power of sender cells on the colony and single-cell level. This contributes a better characterization of this important inter-bacterial communication channel for rationally designed synthetic biology applications that takes the stochastic nature of gene expression into account. The same approach and methods can be used to characterize natural quorum sensing systems in quantitative detail to further elucidate the communication behavior in bacterial communities.

## Supporting Information

**S1 File. Supplementary Text A–C, Supplementary Figs A–F.** Text A, Image processing. Text B, Gene expression noise. Text C, Sender—receiver system. Fig A, Schematic overview of the bacterial sender-receiver system. *Sender cells*: As indicated, in the presence of IPTG repressor protein LacI is not bound to the lac promoters  $P_{LacUV5}$  on the bacterial genome and  $P_{T7lac}$  on the sender plasmid. T7 RNA polymerase is then expressed, which in turn leads to the expression of AHL synthase LuxI and fluorescent reporter protein RFP from the plasmid. LuxI catalyzes the production of the quorum sensing signal N-3-oxo-C6-homoserine lactone (AHL), which can freely pass through the bacterial cell wall. *Receiver cells* constitutively express activator LuxR from the receiver plasmid. In the presence of AHL, LuxR activates GFP expression, which is under the control of the lux promoter  $P_{lux}$ . In the first set of experiments in the main paper, only receiver cells are used and AHL is manually added to the culture medium to induce gene expression. Fig B, Microfluidic chemostats. (A) The microfluidic chemostat consists of a gradient mixer (adopted from Ref. 55 of the main paper), which generates linear concentration gradients of chemicals supplied through inlets 1 and 2, respectively. Eight gradient exits are connected to a total of  $2 \times 8$  microfluidic channels, which contain trapping regions for bacteria (similar to Ref. 8 of the main paper). In the experiments, the concentration of AHL was varied in 1 nM steps in the range 0 – 21 nM, and in 10 nM steps in the range 20 – 90 nM. (B) Top view of a supply channel (blue) with trap region (grey). (C) Side view (not drawn to scale) showing the reduced height of the trap region, which only allows bacterial growth in a single layer. Fig C, Calibration of the gradient mixer system. We performed a series of calibration experiments (with flow rates 40, 80, 160 and 320  $\mu\text{l/h}$ ) to evaluate the quality of the concentration gradient generated by the microfluidic mixer shown in Fig B in S1 File. In these experiments the right reservoir was loaded with buffer solution containing 10  $\mu\text{M}$  fluorescein and the left reservoir with pure buffer (0  $\mu\text{M}$ ). After establishment of a steady gradient, we measured the fluorescence in the trap regions. The background-subtracted fluorescence values were then plotted against the nominal concentrations expected for the traps. As shown in the figure (which is obtained for the 160  $\mu\text{l/h}$  case), indeed a linear concentration gradient is generated. A



linear regression fit to these values (fixed at  $0\mu\text{M}$ ) allows us to estimate the concentration errors. The maximum relative deviation from the nominal concentration is found to be  $\approx 20\%$  in all experiments performed. Fig D, Overview of the image analysis procedure. (A) A composite brightfield and fluorescence image, cropped to display only the microchamber contents. The program workflow is demonstrated by focusing on the red highlighted area of the picture, a region with dimensions  $21.6 \times 12.4 \mu\text{m}^2$ . (B) Once the brightfield image is imported, contrast is enhanced and resolution increased. (C) Background detection is performed via a hybrid method combining adaptive thresholding and geometry information. (D) Cell markers are created using gradient information and geometric priors, refined using the watershed method. (E) A statistical classifier is used to remove mis-segmented cells. (F-I) Using the maximum overlap method, cell lineages are reconstructed (see also Fig D in S1 File). A cell division event is highlighted in (F-G); and propagated forward in (H-I). The user can correct tracking errors manually in the application. Fig E, Example of a cell lineage extracted using the segmentation software. The lineage is first automatically calculated by using the maximum overlap method on the segmented cells, as described in the main text. The segmentation method is conservative in detecting cell divisions, which means that already divided cells may be detected as a single cell for a few frames longer. This explains the observed cell division timings in the above lineage tree. After this step a correction heuristic is applied which finds potential mother-daughter mismatches by searching for fluorescence fluctuations twice as large as the calculated noise in a typical trajectory. For presentational clarity any branches which do not reach the final frame (due to mismatches) were manually edited out of the above plot. Fig F, Bulk analysis of gene induction by AHL using plate reader measurements. (A) Background subtracted absorbance of growing bacterial cultures for AHL concentrations ranging from 0 nM to 100 nM. (B) Corresponding background subtracted fluorescence intensities for the different AHL concentrations. (C) Maximum gene expression rate  $\alpha_{\text{max}}$  obtained for the different AHL concentrations as explained in the main text. The solid line is a fit with a Hill curve with Hill exponent  $n = 0.97 \pm 0.08$  and induction threshold  $K = 13.9 \pm 1.7 \text{ nM}$ . (PDF)

## Acknowledgments

The authors acknowledge financial support by the European Commission FP7 (grant no. 248919—BACTOCOM) and the Deutsche Forschungsgemeinschaft (Cluster of Excellence Nanosystems Initiative Munich—NIM). UG acknowledges support by the DFG priority program SPP 1617.

## Author Contributions

Conceived and designed the experiments: A. Meyer A. Mückl FCS. Performed the experiments: A. Meyer A. Mückl. Analyzed the data: TR A. Meyer KK UG FCS. Contributed reagents/materials/analysis tools: TR KK. Wrote the paper: TR A. Meyer UG FCS.

## References

1. Fuqua C, Greenberg EP. Listening in on bacteria: acyl-homoserine lactone signalling. *Nat Rev Mol Cell Bio.* 2002; 3(9):685–95.
2. Waters CM, Bassler BL. Quorum Sensing: Cell-to-Cell Communication in Bacteria. *Annu Rev Cell Dev Bi.* 2005; 21(1):319–346. doi: [10.1146/annurev.cellbio.21.012704.131001](https://doi.org/10.1146/annurev.cellbio.21.012704.131001)
3. Weiss R, Knight TF Jr. Engineered Communications for Microbial Robotics. In: Condon AE, Rozenberg G, editors. *DNA Computing, 6th International Workshop on DNA-Based Computers, DNA6*. vol. 2054 of *Lecture Notes in Computer Science*. Springer; 2000. p. 1–16.

4. You LC, Cox RS, Weiss R, Arnold FH. Programmed population control by cell-cell communication and regulated killing. *Nature*. 2004; 428(6985):868–871. PMID: [15064770](#)
5. Balagadde FK, You LC, Hansen CL, Arnold FH, Quake SR. Long-term monitoring of bacteria undergoing programmed population control in a microchemostat. *Science*. 2005; 309(5731):137–140. doi: [10.1126/science.1109173](#) PMID: [15994559](#)
6. Basu S, Gerchman Y, Collins CH, Arnold FH, Weiss R. A synthetic multicellular system for programmed pattern formation. *Nature*. 2005; 434(7037):1130–4. PMID: [15858574](#)
7. Sohka T, Heins R, Phelan R, Greisler J, Townsend C, Ostermeier M. An externally tunable bacterial band-pass filter. *P Natl Acad Sci USA*. 2009; 106(25):10135–10140. doi: [10.1073/pnas.0901246106](#)
8. Danino T, Mondragón-Palomino O, Tsimring L, Hasty J. A synchronized quorum of genetic clocks. *Nature*. 2010; 463(7279):326–330. PMID: [20090747](#)
9. Tabor JJ, Salis HM, Simpson ZB, Chevalier AA, Levskaya A, Marcotte EM, et al. A Synthetic Genetic Edge Detection Program. *Cell*. 2009 Jun; 137(7):1272–1281. PMID: [19563759](#)
10. Tamsir A, Tabor JJ, Voigt CA. Robust multicellular computing using genetically encoded NOR gates and chemical 'wires'. *Nature*. 2011; 469(7329):212–215. PMID: [21150903](#)
11. Weitz M, Mückl A, Kapsner K, Berg R, Meyer A, Simmel FC. Communication and Computation by Bacteria Compartmentalized within Microemulsion Droplets. *J Am Chem Soc*. 2014; 136(1):72–75. doi: [10.1021/ja411132w](#) PMID: [24358940](#)
12. Elowitz MB, Levine AJ, Siggia ED, Swain PS. Stochastic gene expression in a single cell. *Science*. 2002; 297(5584):1183–1186. doi: [10.1126/science.1070919](#) PMID: [12183631](#)
13. Golding I, Paulsson J, Zawilski S, Cox E. Real-time kinetics of gene activity in individual bacteria. *Cell*. 2005; 123(6):1025–1036. PMID: [16360033](#)
14. Kaern M, Elston TC, Blake WJ, Collins JJ. Stochasticity in gene expression: from theories to phenotypes. *Nat Rev Genet*. 2005; 6(6):451–464. PMID: [15883588](#)
15. Raj A, van Oudenaarden A. Nature, Nurture, or Chance: Stochastic Gene Expression and Its Consequences. *Cell*. 2008; 135(2):216–226. PMID: [18957198](#)
16. Munsky B, Neuert G, van Oudenaarden A. Using gene expression noise to understand gene regulation. *Science*. 2012; 336(6078):183–7. doi: [10.1126/science.1216379](#) PMID: [22499939](#)
17. Tsimring LS. Noise in biology. *Rep Prog Phys*. 2014; 77(2):026601. Available from: <http://iopscience.iop.org/0034-4885/77/2/026601>. PMID: [24444693](#)
18. Silander OK, Nikolic N, Zaslaver A, Bren A, Kikoin I, Alon U, et al. A Genome-Wide Analysis of Promoter-Mediated Phenotypic Noise in *Escherichia coli*. *PLoS Genet*. 2012; 8(1):e1002443. Available from: <http://dx.doi.org/10.1371/journal.pgen.1002443>. doi: [10.1371/journal.pgen.1002443](#) PMID: [22275871](#)
19. Paulsson J. Models of stochastic gene expression. *Phys Life Rev*. 2005; 2(2):157–175. doi: [10.1016/j.plrev.2005.03.003](#)
20. Friedman N, Cai L, Xie XS. Linking stochastic dynamics to population distribution: An analytical framework of gene expression. *Phys Rev Lett*. 2006; 97(16). doi: [10.1103/PhysRevLett.97.168302](#)
21. Huh D, Paulsson J. Non-genetic heterogeneity from stochastic partitioning at cell division. *Nat Genet*. 2011; 43(2):95–100. PMID: [21186354](#)
22. Huh D, Paulsson J. Random partitioning of molecules at cell division. *P Natl Acad Sci USA*. 2011; 108(36):15004–15009. doi: [10.1073/pnas.1013171108](#)
23. Cox CD, Peterson GD, Allen MS, Lancaster JM, McCollum JM, Austin D, et al. Analysis of noise in quorum sensing. *Omics: a journal of integrative biology*. 2003; 7(3):317–34. doi: [10.1089/153623103322452422](#) PMID: [14583119](#)
24. Tanouchi Y, Tu D, Kim J, You L. Noise Reduction by Diffusional Dissipation in a Minimal Quorum Sensing Motif. *PLoS Computational Biology*. 2008; 4(8):e1000167. doi: [10.1371/journal.pcbi.1000167](#) PMID: [18769706](#)
25. Long T, Tu KC, Wang Y, Mehta P, Ong NP, Bassler BL, et al. Quantifying the Integration of Quorum-Sensing Signals with Single-Cell Resolution. *PLoS Biol*. 2009; 7(3):e68. doi: [10.1371/journal.pbio.1000068](#) PMID: [19320539](#)
26. Wang Y, Tu KC, Ong NP, Bassler BL, Wingreen NS. Protein-level fluctuation correlation at the microcolony level and its application to the *Vibrio harveyi* quorum-sensing circuit. *Biophysical Journal*. 2011; 100(12):3045–53. PMID: [21689539](#)
27. Locke JCW, Elowitz MB. Using movies to analyse gene circuit dynamics in single cells. *Nat Rev Microbiol*. 2009; 7(5):383–392. PMID: [19369953](#)
28. Groisman A, Lobo C, Cho H, Campbell JK, Dufour YS, Stevens AM, et al. A microfluidic chemostat for experiments with bacterial and yeast cells. *Nat Methods*. 2005; 2(9):685–689. PMID: [16118639](#)



29. Bennett MR, Hasty J. Microfluidic devices for measuring gene network dynamics in single cells. *Nat Rev Genet.* 2009; 10(9):628–638. PMID: [19668248](#)
30. Yan L, Allen MS, Simpson ML, Saylor GS, Cox CD. Direct quantification of N-(3-oxo-hexanoyl)-L-homoserine lactone in culture supernatant using a whole-cell bioreporter. *Journal of microbiological methods.* 2007; 68(1):40–5. PMID: [16916554](#)
31. Hense BA, Kuttler C, Müller J, Rothballer M, Hartmann A, Kreft JU. Does efficiency sensing unify diffusion and quorum sensing? *Nat Rev Microbiol.* 2007; 5(3):230–9. PMID: [17304251](#)
32. West SA, Winzer K, Gardner A, Diggle SP. Quorum sensing and the confusion about diffusion. *Trends Microbiol.* 2012; 20(12):586–594. doi: [10.1016/j.tim.2012.09.004](#) PMID: [23084573](#)
33. Cormack B, Valdivia R, Falkow S. FACS-optimized mutants of the green fluorescent protein (GFP). *Gene.* 1996; 173(1):33–38. PMID: [8707053](#)
34. Dertinger SKW, Chiu DT, Jeon NL, Whitesides GM. Generation of Gradients Having Complex Shapes Using Microfluidic Networks. *Anal Chem.* 2001; 73(6):1240–1246. doi: [10.1021/ac001132d](#)
35. Wang Q, Niemi J, Tan CM, You L, West M. Image segmentation and dynamic lineage analysis in single-cell fluorescence microscopy. *Cytom Part A.* 2010; 77A(1):101–110. Available from: <http://doi.wiley.com/10.1002/cyto.a.20812>.
36. Rämö P, Sacher R, Snijder B, Begemann B, Pelkmans L. CellClassifier: supervised learning of cellular phenotypes. *Bioinformatics.* 2009 Nov; 25(22):3028–3030. doi: [10.1093/bioinformatics/btp524](#) PMID: [19729371](#)
37. Urbanowski ML, Lostroh CP, Greenberg EP. Reversible acyl-homoserine lactone binding to purified *Vibrio fischeri* LuxR protein. *J Bacteriol.* 2004; 186(3):631–7. doi: [10.1128/JB.186.3.631-637.2004](#) PMID: [14729687](#)
38. Haseltine EL, Arnold FH. Implications of Rewiring Bacterial Quorum Sensing. *Applied and Environmental Microbiology.* 2008; 74(2):437–445. doi: [10.1128/AEM.01688-07](#) PMID: [18039819](#)
39. Carbonell-Ballester M, Duran-Nebreda S, Montanez R, Sole R, Macia J, Rodriguez-Caso C. A bottom-up characterization of transfer functions for synthetic biology designs: lessons from enzymology. *Nucleic Acids Res.* 2014; 42(22):14060–14069. doi: [10.1093/nar/gku964](#) PMID: [25404136](#)
40. Koch AL. The logarithm in biology 1. Mechanisms generating the log-normal distribution exactly. *J Theor Biol.* 1966 Nov; 12(2):276–290. doi: [10.1016/0022-5193\(66\)90119-6](#) PMID: [5972197](#)
41. Koch AL. The logarithm in biology: II. Distributions simulating the log-normal. *J Theor Biol.* 1969 May; 23(2):251–268. doi: [10.1016/0022-5193\(69\)90040-X](#) PMID: [5821531](#)
42. Berg OG. A model for the statistical fluctuations of protein numbers in a microbial population. *J Theor Biol.* 1978; 71(4):587–603. doi: [10.1016/0022-5193\(78\)90326-0](#) PMID: [96307](#)
43. Ozbudak EM, Thattai M, Kurtser I, Grossman AD, van Oudenaarden A. Regulation of noise in the expression of a single gene. *Nat Genet.* 2002 May; 31(1):69–73. doi: [10.1038/ng869](#) PMID: [11967532](#)
44. Shahrezaei V, Swain PS. Analytical distributions for stochastic gene expression. *Proc Natl Acad Sci USA.* 2008 Nov; 105(45):17256–17261. doi: [10.1073/pnas.0803850105](#) PMID: [18988743](#)
45. Taniguchi Y, Choi PJ, Li GW, Chen H, Babu M, Hearn J, et al. Quantifying *E. coli* proteome and transcriptome with single-molecule sensitivity in single cells. *Science.* 2010 Jul; 329(5991):533–538. doi: [10.1126/science.1188308](#) PMID: [20671182](#)
46. Hense BA, Müller J, Kuttler C, Hartmann A. Spatial heterogeneity of autoinducer regulation systems. *Sensors.* 2012; 12(4):4156–4171. PMID: [22666024](#) doi: [10.3390/s120404156](#)
47. Dilanji GE, Langebrake JB, De Leenheer P, Hagen SJ. Quorum activation at a distance: spatiotemporal patterns of gene regulation from diffusion of an autoinducer signal. *J Am Chem Soc.* 2012 Mar; 134(12):5618–5626. doi: [10.1021/ja211593q](#) PMID: [22372494](#)
48. Choi WS, Ha D, Park S, Kim T. Synthetic multicellular cell-to-cell communication in inkjet printed bacterial cell systems. *Biomaterials.* 2011 Apr; 32(10):2500–2507. doi: [10.1016/j.biomaterials.2010.12.014](#) PMID: [21208654](#)

### 2.2. Communication and computation by bacteria compartmentalized within microemulsion droplets

We encapsulated genetically modified *E. coli* within water-in-oil droplets. The sender strain was able to produce autoinducer I molecules 3-oxo-C6-HSL (here AHL) and red fluorescent protein (RFP) upon induction with IPTG. The receiver strain answered with the expression of GFP in the presence of the quorum sensing molecule AHL. The spatially separated bacteria strains performed different communication modes across emulsion droplets by sending and detecting the signal molecules.

In our experimental setup, we addressed three communication paths. First, we studied AHL droplets inducing encapsulated AHL-receiver bacteria in proximity. From time-lapse fluorescent microscopy movies and tracking of individual droplet we gained information about the time course of each position, size and intensity for different AHL concentrations. With this data on hand and a simple reaction-diffusion model (initial parameters were partly obtained from bulk measurements) we found distance dependent gene induction and reduced effective diffusion coefficient of  $D_{\text{eff}} = 2 \mu\text{m}^2 \text{s}^{-1}$  for AHL compared to solely aqueous medium.

Since we demonstrated that small, amphiphilic molecules such as AHL were partly soluble in our surfactant/oil mix, we expanded our experiments to further suitable chemicals such as IPTG. Due to its slight amphiphilic character and capability to diffuse through cell membranes, we tested whether IPTG reservoir droplets induce sender bacteria droplets.

Indeed, time-lapse videos with RFP as reporter gene, confirmed the induction process and temporal evolution towards IPTG-receiver cell droplets further apart from the inducer droplets. However, due to its less beneficial octanol/water partitioning coefficient, an even lower effective diffusion coefficient of  $D_{\text{eff}} = 0.05 \mu\text{m}^2 \text{s}^{-1}$  was determined for IPTG compared to AHL.

The communication scenario between AHL-sending and AHL-receiving cells in spatially separated droplets confirmed the reduction of diffusivity for AHL.

As a final experiment and to show the integration of a multi-channel system with our bacterial droplet communicator, we introduced an AND-gate circuit in our receiver cells. The integration of a two-input chemical signal, namely AHL and IPTG was studied and the transfer functions determined as in the previous experiments.

The following copy of the original research article (7) shows the above-summarized results in detail. Supplemental figures, tables and methods can be found in the [Appendix](#). For supplemental movies, please refer to the publishing journal.

## Communication and Computation by Bacteria Compartmentalized within Microemulsion Droplets

Maximilian Weitz,<sup>‡</sup> Andrea Mückl,<sup>‡</sup> Korbinian Kapsner, Ronja Berg, Andrea Meyer, and Friedrich C. Simmel\*

Physics Department E14 and ZNN/WSI, Technische Universität München, Am Coulombwall 4a, D-85748 Garching, Germany

### S Supporting Information

**ABSTRACT:** Amphiphilic inducer molecules such as *N*-acyl-L-homoserine lactones (AHLs) or isopropyl- $\beta$ -D-thiogalactopyranoside (IPTG) can be utilized for the implementation of an artificial communication system between groups of *E. coli* bacteria encapsulated within water-in-oil microemulsion droplets. Using spatially extended arrays of microdroplets, we study the diffusion of both AHL and IPTG from inducer-filled reservoirs into bacteria-containing droplets, and also from droplets with AHL producing sender bacteria into neighboring droplets containing receiver cells. Computational modeling of gene expression dynamics within the droplets suggests a strongly reduced effective diffusion coefficient of the inducers, which markedly affects the spatial communication pattern in the neighborhood of the senders. Engineered bacteria that integrate AHL and IPTG signals with a synthetic AND gate gene circuit are shown to respond only in the presence of both types of sender droplets, which demonstrates the potential of the system for genetically programmed pattern formation and distributed computing.

Quorum sensing (QS) is a mode of chemical communication between bacteria mediated by diffusible inducer molecules called autoinducers (AIs). In a typical QS system, AIs are produced by an AI synthase, whose production is itself controlled by the presence of AI. Due to the membrane-penetrating nature of the AIs, AI-inducible genes may also be influenced in neighboring bacteria, which facilitates the induction of genes in a cell-density dependent manner, hence the name “quorum sensing”.<sup>1</sup> QS has been identified both in gram negative as well as in gram positive bacteria, with different classes of AIs.<sup>2</sup> Chemically, the AI-1 class AIs are *N*-acyl-L-homoserine lactones (AHLs), which are found in gram negative bacteria. Specifically, the AI-1 of the bacterium *Aliivibrio fischeri*<sup>3</sup> used in the present work—regulating the LuxR-LuxI system—is the amphiphilic molecule *N*-(3-oxohexanoyl)-L-homoserine lactone (3OC6HSL).

In the context of synthetic biology, bacterial QS systems have been frequently utilized as a means of communication between engineered bacteria. In a seminal work, Weiss and Knight<sup>4</sup> artificially separated the QS system of *A. fischeri* into “sender” and “receiver” parts, and were therefore able to realize the first synthetic bacterial communication system. Based on this sender-receiver system, various gene circuits were engineered,

such as a population control system,<sup>5</sup> pattern-forming systems,<sup>6</sup> or distributed bacterial computing.<sup>7</sup> Artificial microenvironments and microfluidics<sup>8</sup> have been previously used to investigate spatial aspects of cell-to-cell communication via QS. For instance, QS between groups of bacteria was studied using inkjet printing,<sup>9</sup> fiberoptic microarrays<sup>10</sup> or by microfluidic confinement within small aqueous droplets.<sup>11</sup> Recently, also signaling between bacteria confined in an emulsion droplet to a neighboring compartment within a microfluidic double droplet trap was shown,<sup>12</sup> a mechanism that is also used in our work.

Here, we utilize a genetically engineered QS-based sender-receiver system, but also the conventional inducer/repressor module isopropyl- $\beta$ -D-thiogalactopyranoside (IPTG)/LacI to implement a spatially extended communication system between *E. coli* bacteria encapsulated within large populations of water-in-oil emulsion droplets (cf. Figures S1 and S2). We find that both AHL (3OC6HSL) and IPTG partly dissolve in the oil phase (Figures S5 and S6). The resulting slow diffusion of the inducers from compartment to compartment establishes two chemical communication channels between the droplets, which can be directly demonstrated using computational bacteria that process AHL and IPTG signals as inputs of a simple genetic AND gate. Integration of several slowly diffusing signals within a droplet population using synthetic gene regulatory circuits is expected to enable programmable pattern formation<sup>6a</sup> and distributed computing<sup>7,13</sup> on a shorter length scale than in aqueous medium.<sup>14</sup>

We first investigated the influence of inducer-filled “reservoir” droplets without bacteria on gene expression in “receiver cells” in neighboring droplets (Figure 1A). Emulsion droplets were formed using a microfluidic flow-focusing device made of PDMS, in which an aqueous phase was mixed with fluorocarbon oil containing a nonionic, biocompatible surfactant.<sup>15</sup> A schematic representation of the receiver genetic circuit is shown in Figure 1b. Receiver bacteria constitutively expressed the *A. fischeri* QS regulatory protein LuxR, which acts as an activator of gene expression upon binding to AHL. As a read-out for the presence of AHL, the expression of green fluorescent protein (GFP) was put under the control of the AHL-inducible promoter pLuxR. Cell densities were chosen sufficiently low to ensure that either no or only few bacteria were present within each droplet initially.

Received: October 31, 2013

Published: December 20, 2013



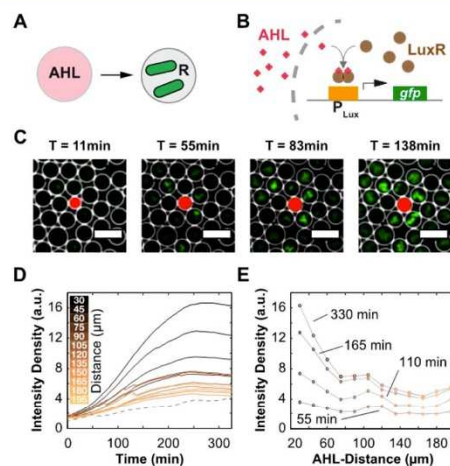


**Figure 1.** (A) Receiver bacteria in the presence of AHL reservoir droplets. (B) Receiver gene circuit. AHL enters a receiver cell through the cell membrane (dashed line) and binds to constitutively expressed LuxR. LuxR:AHL dimers activate expression of GFP. (C) Fluorescence microscopy time series of receiver cells close to an AHL reservoir droplet (red). White circles are derived from bright field (BF) images and represent droplet surfaces. AHL diffuses from reservoir to receiver droplets and induces gene expression in a distant dependent manner (scale bar, 50  $\mu\text{m}$ ; dark droplets close to reservoirs do not contain cells, cf. Figure S2 for higher magnification and BF). (D) Evolution of the average fluorescence intensity of droplets containing receiver cells for different distances from the next nearest reservoir droplet. An appropriately scaled fluorescence time trace from a control experiment with uninduced receiver cells is included for comparison (dashed line). (E) Intensity profiles for different times obtained from the traces in (D).

In Figure 1C, images extracted from a fluorescence microscopy time-lapse movie of a reservoir droplet surrounded by receiver cell droplets are shown, which confirm that gene expression is first induced in droplets adjacent to the reservoirs and starts later in receiver droplets further apart. Gene expression experiments in bulk showed that in the presence of AHL pLuxR-controlled GFP production follows an activation function  $\sim 1/(1 + K_{\text{AHL}}^n/[AHL]^n)$ , with a threshold concentration of  $K_{\text{AHL}} \approx 15$  nM, and a Hill exponent of  $n = 1.6$  (Figure S3). The inducer concentration in the reservoir droplets was therefore chosen to be  $[AHL] = 200$  nM, i.e., more than 10 times the induction threshold.

In order to study the spatiotemporal dynamics of gene expression, in Figure 1D the change of fluorescence collected from 1405 bacteria-filled droplets grouped according to their distance to the next nearest AHL reservoir droplets (in total 91) is shown as a function of time (cf. Figure S1 for image processing). As the droplets roughly arrange in a hexagonally closed packed lattice, the mean distance between reservoir droplets is estimated to be  $\approx 66$   $\mu\text{m}$ . Thus, the curves only approximately reflect the true distance dependence of gene expression that would be caused by an isolated reservoir droplet. Fluorescence profiles for different distances from reservoir droplets 55, 110, 165, and 330 min after initiation of the experiment are shown in Figure 1E. A clear response of

receiver bacteria is visible up to distances of  $\sim 100$   $\mu\text{m}$  from the reservoir droplets. Qualitatively, inducers diffuse away from the source droplets and induce GFP expression in neighboring receiver droplets. Due to depletion of the reservoirs, decay of inducers and gene products and also due to limited growth of the bacteria in the droplets, gene activation is only transient, leading to the particular shape of the response curves displayed in Figure 1D,E. Figure 1D can be understood more quantitatively in terms of a simple reaction–diffusion (RD) model (SI section 4.7, Figures S8 and S9), yet only with the assumption of a strongly reduced effective diffusivity of AHL on the order of  $D_{\text{eff}} \approx 1$   $\mu\text{m}^2/\text{s}$  as compared to the bulk case, for which diffusivities in the range of  $D_{\text{bulk}} \approx 100$ – $1000$   $\mu\text{m}^2/\text{s}$  are typically assumed.<sup>9,13a,14,16</sup> As discussed in SI section 4.7, this may be explained by varying diffusion coefficients in the different phases, the permeability of the interfaces, and also by geometrical effects.

In order to address the question, whether communication takes place mainly through the interface formed by surfactants between droplets in direct physical contact or via free diffusion through the oil phase, we performed a series of control experiments (Figure S5). We found that 3OC6HSL partly dissolves in the oil phase, which is in accordance with its slight hydrophobicity characterized by an octanol/water partitioning coefficient ( $\log P$ ) in the range 0.2–2,<sup>17</sup> and we also found gene induction in isolated receiver droplets not in physical contact with senders. It is thus conceivable that transport occurs both directly through the interface between touching droplets and via the oil phase.

We reasoned that a droplet-to-droplet induction might also be possible with a conventional inducer such as IPTG, in particular as its chemical structure also suggests an amphiphilic nature<sup>18</sup> (for the IPTG activation function, cf. Figure S4 and SI section 4.5). Experiments equivalent to those with AHL were performed with IPTG-containing droplets and droplets with corresponding receiver bacteria, which contained a gene for a red fluorescent protein (RFP) under the control of a Lac promoter. Indeed, expression of RFP was observed in these bacteria only in the presence of reservoir droplets (see Figure S7). We found that also IPTG partitions into the oil phase (Figure S6), and the dynamics of gene expression was again consistent with a strongly reduced effective diffusion coefficient for the inducer (Figure S10).

In order to demonstrate spatially extended chemical communication between bacteria within droplet arrays, we also performed experiments, in which we exchanged inducer-filled reservoir droplets by droplets containing bacteria expressing the AHL synthase LuxI (“sender cells”, Figure 2A). The genetic module responsible for AHL synthesis is shown in Figure 2B. As expected, the fluorescence in receiver cells increases as sender cells synthesize AHL, which is transduced through the emulsion (Figure 2C). Analysis of signals recorded from 1679 receiver droplets mixed with 13 sender droplets again reveals distance-dependent GFP expression levels of receiver cells as shown in Figure 2D. This gene activation pattern is very well reproduced by our RD model when reservoirs with a finite supply are exchanged for permanently producing inducer sources (Figure S11).

With two diffusible inducer molecules available, we investigated an emulsion mixture of droplets containing engineered bacteria, which responded to the simultaneous presence of IPTG and AHL as inputs (Figure 3A). To this end, a genetic AND gate was constructed, in which IPTG induced

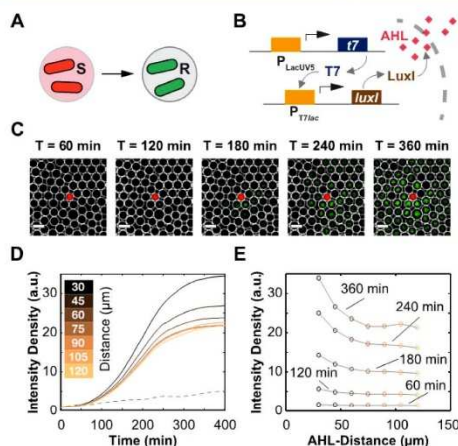


**Figure 2.** (A) Receiver bacteria in the presence of droplets containing sender cells. (B) Sender gene circuit. A T7 RNA polymerase expressed from an IPTG inducible promoter drives the expression of AHL synthase LuxI. AHL diffuses through the cell membrane (dashed line) into the extracellular medium. (C) Fluorescence microscopy time series recorded from receiver cells in the proximity of a sender droplet (red). AHL spreads by diffusion and activates GFP expression in receiver cells (green). Scale bar, 25  $\mu\text{m}$ . (D) Evolution of the average fluorescence intensity of droplets containing receiver cells for various distances from the next nearest sender-containing droplet. A fluorescence time trace from a control experiment with uninduced receiver cells is also shown (dashed line). (E) Intensity profile at different times corresponding to the traces shown in (D).

expression of LuxR, while AHL activated GFP expression via binding to LuxR (Figure 3B). We first characterized the operation of the AND gate circuit in bulk experiments (SI section 4.5), from which the dose–response function depicted in Figure 3C was extracted. As designed, GFP expression was high only in the presence of both inducers. We then studied the response of droplets containing AND-gate bacteria in the presence of reservoir droplets with low inducer concentrations ( $[\text{AHL}] = 20 \text{ nM}$ ,  $[\text{IPTG}] = 200 \mu\text{M}$ ). In Figure 3D, the corresponding population mean of single droplet fluorescence time traces are shown. As desired, encapsulated AND gate bacteria express GFP only when both AHL and IPTG filled reservoir droplets are present, whereas expression remains low in the absence of one or both inducers. Fluorescence microscopy images of AND-gate bacteria droplets in the presence of either no, one, or both types of inducer droplets taken 18 h after initiation of the experiment are shown in Figure 3E. As expected, green fluorescence is high only when both inducer filled droplets are present. For reservoir droplets with higher inducer concentrations—and thus larger “diffusion range”—also spatial effects can be observed. The AND gate response for this case as a function of distance to the nearest AHL and IPTG reservoirs is shown in Figure S14.

We have shown that amphiphilic inducer molecules such as the QS signal 3OC6HSL or the conventional inducer IPTG can establish chemical communication between chemical reservoirs and small groups of bacteria encapsulated within water-in-oil microemulsion droplets, and this presumably holds true also for other amphiphilic compounds, e.g., antibiotics. Using engi-

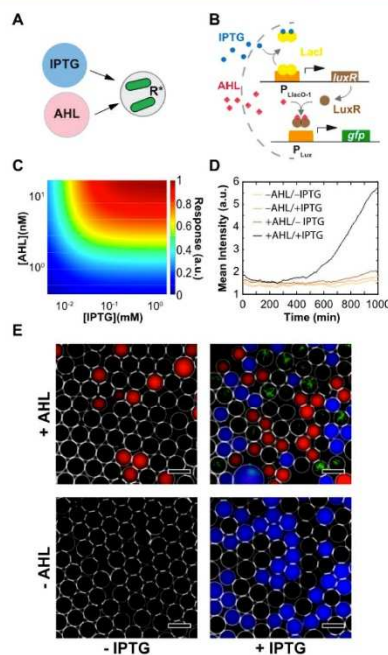


**Figure 3.** (A) Receiver bacteria containing a genetic AND gate. AHL and IPTG diffuse from reservoir droplets to a receiver droplet with engineered bacteria containing a genetic AND gate. (B) AND-gate gene circuit in the presence of both input molecules. IPTG enters the bacterial cell, binds to the Lac repressor LacI and thus induces expression of LuxR. AHL then binds to LuxR and thus activates expression of GFP. (C) Response of the genetic AND-gate to varying input molecule concentrations. The diagram shows the fit of a two-dimensional input function to values determined in bulk measurements (SI section 4.5). (D) Fluorescence time traces of droplet populations containing computational receiver bacteria in the presence (+) or absence (−) of inducer-filled reservoir droplets (for single droplet traces see Figure S12). (E) Fluorescence microscopy images arranged in a truth table (BF images in Figure S13). AND-gate bacteria express GFP when both AHL (red) and IPTG (blue) reservoir droplets are present. Scale bar, 50  $\mu\text{m}$ .

neered computational bacteria, several of such signals sent out from distinct reservoir droplets can be integrated within receiver droplets in a context-dependent manner. As natural QS occurs in complex environments such as biofilms,<sup>1c,16</sup> emulsion systems may actually be used as models for the study of bacterial communication in heterogeneous media. Apart from this, a small, potentially tunable diffusivity for bacterial communication could be of considerable interest for applications in synthetic biology. Several studies have explored genetically programmed structure formation in the past,<sup>6a,13a</sup> resulting in patterns on a millimeter length scale. Tuning of the diffusion coefficient to smaller values would reduce the patterning length scale by a factor  $(D_0/D_{\text{eff}})^{1/2}$ , which is of order  $\sim 10$  in our case.

An additional interesting feature of a droplet-based bacterial communication system is the fact that communication takes



place between small and spatially separated groups of bacteria. In principle, different types (even species) of bacteria with potentially different environmental requirements could be prepared in different droplets, and their interactions studied without mixing of the bacteria themselves.

Another aspect of compartmentalization is the fact that chemical signals are sent out or received by small groups of bacteria, which is expected to average out fluctuations caused by single cell variability.<sup>19</sup> Previous studies on distributed computing based on spatially separated, communicating microcolonies<sup>7,13b</sup> have emphasized the fact that such averaging makes bacterial computing more robust than in alternative concepts based on intracellular (single cell) computing. A distributed bacterial computer implemented in microemulsions potentially could be faster and operate with reduced space requirements.

## ■ ASSOCIATED CONTENT

### Supporting Information

Materials, methods, additional data, and modeling. This material is available free of charge via the Internet at <http://pubs.acs.org>.

## ■ AUTHOR INFORMATION

### Corresponding Author

[simmel@tum.de](mailto:simmel@tum.de)

### Author Contributions

<sup>‡</sup>The first two authors contributed equally.

### Notes

The authors declare no competing financial interest.

## ■ ACKNOWLEDGMENTS

We gratefully acknowledge financial support through the European Commission FP7 grant no. 248919 (BACTOCOM), the Nanosystems Initiative Munich (NIM), and the Elitenetzwerk Bayern. We thank S. Gude for initiating experiments.

## ■ REFERENCES

- (1) (a) Müller, M. B.; Bassler, B. L. *Annu. Rev. Microbiol.* **2001**, *55*, 165. (b) Fuqua, C.; Greenberg, E. P. *Nat. Rev. Mol. Cell Biol.* **2002**, *3*, 685. (c) Hense, B. A.; Kuttler, C.; Müller, J.; Rothballer, M.; Hartmann, A.; Kreft, J. U. *Nat. Rev. Microbiol.* **2007**, *5*, 230.
- (2) Waters, C. M.; Bassler, B. L. *Annu. Rev. Cell Dev. Biol.* **2005**, *21*, 319.
- (3) Urbanczyk, H.; Ast, J. C.; Higgins, M. J.; Carson, J.; Dunlap, P. V. *Int. J. Syst. Anal. Evol. Microbiol.* **2007**, *57*, 2823.
- (4) Weiss, R.; Knight, T. F., Jr. In *DNA Computing, 6th International Workshop on DNA-Based Computers, DNA6*; Condon, A. E., Rozenberg, G., Eds.; Springer: Berlin, 2000; Vol. 2054, p 1.
- (5) You, L. C.; Cox, R. S.; Weiss, R.; Arnold, F. H. *Nature* **2004**, *428*, 868.
- (6) (a) Basu, S.; Gerchman, Y.; Collins, C. H.; Arnold, F. H.; Weiss, R. *Nature* **2005**, *434*, 1130. (b) Sohka, T.; Heins, R.; Phelan, R.; Greisler, J.; Townsend, C.; Ostermeier, M. *Proc. Natl. Acad. Sci. U.S.A.* **2009**, *106*, 10135.
- (7) Tamsir, A.; Tabor, J. J.; Voigt, C. A. *Nature* **2011**, *469*, 212.
- (8) Danino, T.; Mondragón-Palomino, O.; Tsimring, L.; Hasty, J. *Nature* **2010**, *463*, 326.
- (9) Choi, W. S.; Ha, D.; Park, S.; Kim, T. *Biomaterials* **2011**, *32*, 2500.
- (10) Whitaker, R. D.; Pember, S.; Wallace, B. C.; Brodley, C. E.; Walt, D. R. *J. Biol. Chem.* **2011**, *286*, 21623.
- (11) (a) Boedicker, J. Q.; Vincent, M. E.; Ismagilov, R. F. *Angew. Chem., Int. Ed.* **2009**, *48*, 5908. (b) Shim, J.-u.; Patil, S. N.; Hodgkinson, J. T.; Bowden, S. D.; Spring, D. R.; Welch, M.; Huck, W. T. S.; Hollfelder, F.; Abell, C. *Lab Chip* **2011**, *11*, 1132.
- (12) Bai, Y.; Patil, S.; Bowden, S.; Poulter, S.; Pan, J.; Salmond, G.; Welch, M.; Huck, W.; Abell, C. *Int. J. Mol. Sci.* **2013**, *14*, 10570.
- (13) (a) Tabor, J. J.; Salis, H. M.; Simpson, Z. B.; Chevalier, A. A.; Levskaya, A.; Marcotte, E. M.; Voigt, C. A.; Ellington, A. D. *Cell* **2009**, *137*, 1272. (b) Regot, S.; Macia, J.; Conde, N.; Furukawa, K.; Kjellén, J.; Peeters, T.; Hohmann, S.; Nadal, E. d.; Posas, F.; Solé, R. *Nature* **2011**, *469*, 207.
- (14) Dilanji, G.; Langebrake, J.; De Leenheer, P.; Hagen, S. *J. Am. Chem. Soc.* **2012**, *134*, 5618.
- (15) Holtze, C.; Rowat, A. C.; Agresti, J. J.; Hutchison, J. B.; Angile, E. E.; Schmitz, C. H. J.; Koster, S.; Duan, H.; Humphry, K. J.; Scanga, R. A.; Johnson, J. S.; Pisignano, D.; Weitz, D. A. *Lab Chip* **2008**, *8*, 1632.
- (16) Hense, B. A.; Müller, J.; Kuttler, C.; Hartmann, A. *Sensors* **2012**, *12*, 4156.
- (17) (a) Li, X.; Fekete, A.; Englmann, M.; Gotz, C.; Rothballer, M.; Frommberger, M.; Buddrus, K.; Fekete, J.; Cai, C.; Schroder, P.; Hartmann, A.; Chen, G.; Schmitt-Kopplin, P. *J. Chromatogr. A* **2006**, *17*, 1. (b) Davis, B. M.; Jensen, R.; Williams, P.; O'shea, P. *PLoS One* **2010**, *5*, e13522. (c) Kamaraju, K.; Smith, J.; Wang, J.; Roy, V.; Sintim, H.; Bentley, W.; Sukharev, S. *Biochemistry* **2011**, *50*, 6983.
- (18) Matias, P. M.; Jeffrey, G. A. *Carbohydr. Res.* **1986**, *153*, 217.
- (19) Raj, A.; van Oudenaarden, A. *Cell* **2008**, *135*, 216.



### 2.3. Chemical communication between bacteria and cell-free gene expression systems within linear chains of emulsion droplets

Inside of a capillary, we loaded picoliter-sized emulsion droplets to arrange them in a linear manner. The droplets were generated by the aid of a microfluidic device and filled with either bacteria or a cell-free transcription/translation reaction mix. In the presents of both chemical input signals AHL and IPTG, a genetic AND-gate circuit, developed in Weitz *et al* (7), reported the expression of green fluorescent protein (GFP). We also utilized genetically modified bacteria to synthesize and ‘send out’ AHL. AHL was also produced *in situ* in our cell-free system. Here we modified the cell-free reaction mix with the AHL-precursor *S*-adenosyl methionine (SAM) and T7 RNA polymerase to attain sufficient amounts of the inducer. With this setup, we encapsulated and arranged different kinds of droplets to achieve various sender-receiver communication chains from ‘bacteria to cell-free’ or *vice versa*.

First, we connected a droplet chain to an inducer reservoir and found in our 1D geometry spatially differentiated gene expression patterns due to the formation of an inducer gradient along neighboring reporter droplets. The dynamics varied between cell-free and bacteria reporter systems, assuming bacterial growth causing the effect. Compared to cell-free gene expression, bacteria droplets were also more affected by oxygen evolution through our fluorinated oil. However, by varying inducer concentrations we could control the number of droplets being induced. By combining AHL and IPTG sender droplets, it was also possible to spatially confine gene expression only to AND gate bacteria close to them.

With this ‘sensor’ device we were further able to estimate the diffusion coefficient for the quorum sensing molecule AHL. We shed light on the understanding of how AHL diffuses through a water-in-oil barrier. We used bulk measurements (microtiter plate experiments) in the  $\mu\text{l}$ -regime to obtain the GFP expression strength for known AHL concentrations and estimated the local AHL concentration of the gene expression pattern of our droplets to obtain the apparent diffusion coefficient ( $D_a$ ). For  $[\text{AHL}] = 200 \text{ nM}$  and  $[\text{AHL}] = 1 \mu\text{M}$  we found  $D_a \approx 0.1 \mu\text{m}^2 \text{ s}^{-1}$ , while for the  $[\text{AHL}] = 10 \mu\text{M}$  we got a higher  $D_a$  of about  $\approx 25 \mu\text{m}^2 \text{ s}^{-1}$ . These findings can be explained by grouping AHL transport into two different modes. Based on our surfactant/oil mix, partitioning effects are the main course of action to transport the molecules within the emulsion for high concentrations of AHL. The alternative transport mechanism for lower AHL concentrations is micelle-mediated diffusion which occurs with approximately  $1 \mu\text{m}^2 \text{ s}^{-1}$ . For detailed explanation see the discussion part in [chapter 3](#).

The following copy of the original research article (11) shows the above-summarized results in detail. Supplemental figures, tables and methods can be found in the [Appendix](#). For supplemental movies, please refer to the publishing journal.



## Integrative Biology

## PAPER

View Article Online

View Journal



Cite this: DOI: 10.1039/c5ib00301f

## Chemical communication between bacteria and cell-free gene expression systems within linear chains of emulsion droplets†

M. Schwarz-Schilling,‡<sup>a</sup> L. Aufinger,‡<sup>a</sup> A. Mückl<sup>a</sup> and F. C. Simmel<sup>\*,ab</sup>Received 20th November 2015,  
Accepted 11th January 2016

DOI: 10.1039/c5ib00301f

www.rsc.org/biology

Position-dependent gene expression in gradients of morphogens is one of the key processes involved in cellular differentiation during development. Here, we study a simple artificial differentiation process, which is based on the diffusion of genetic inducers within one-dimensional arrangements of 50 µm large water-in-oil droplets. The droplets are filled with either bacteria or cell-free gene expression systems, both equipped with genetic constructs that produce inducers or respond to them via expression of a fluorescent protein. We quantitatively study the coupled diffusion-gene expression process and demonstrate that gene expression can be made position-dependent both within bacteria-containing and cell-free droplets. By generating diffusing quorum sensing signals *in situ*, we also establish communication between artificial cell-free sender cells and bacterial receivers, and *vice versa*.

## Insight, innovation, integration

The creation of synthetic multicellular structures composed of artificial and chemical cells, which have the ability to respond to their environment is a topic of increasing interest in synthetic biology. Such systems could be used to create soft, adaptive structures and materials that differentiate in response to environmental cues or morphogens. Here we demonstrate a simple form of spatial differentiation within linear chains of emulsion droplets that are filled either with bacteria or with cell-free gene expression systems. Confinement of genetic inducers to diffuse in only one dimension enables strong coupling of neighboring droplet cells. As an application, we establish chemical communication between cell-free systems and bacteria acting as senders and receivers, and *vice versa*.

## Introduction

Over the past decade, the investigation of bacterial growth, gene expression or population dynamics in artificially structured micro-environments have become increasingly popular,<sup>1</sup> as they allow researchers to follow the dynamics of individual cells within a population over time, and also to precisely control their spatial, temporal, and chemical boundary conditions. In this context, the combination of fluorescence microscopy methods and microfluidic techniques has been shown to be particularly versatile.<sup>2</sup> Microfabricated bacterial traps have been applied to monitor gene expression dynamics over extended periods of time,<sup>3,4</sup> and study, *e.g.* stochastic effects in gene expression,<sup>5–7</sup> or the synchronization of bacterial oscillators.<sup>8</sup> Microfluidic environments have also been

used to study the growth of bacteria<sup>9,10</sup> or perform evolutionary experiments.<sup>11,12</sup> Other experiments were designed to control bacterial shape,<sup>13</sup> or study biofilm formation and bacterial adhesion properties.<sup>14</sup> Microfluidic techniques have been also frequently used for compartmentalization studies, in which single or small numbers of cells were isolated from their environment and also from each other. This has been recently utilized in single cell genomic studies,<sup>15</sup> where the genomic content of a single cell is amplified directly within the compartment using droplet PCR.<sup>16,17</sup>

In previous work, we used picolitre-sized water-in-oil emulsion droplets to compartmentalize small bacterial consortia and study their response to small diffusible inducer molecules.<sup>18</sup> This was based on the finding that inducers such as IPTG or the quorum sensing signal *N*-(3-oxo-hexanoyl)-L-homoserine lactone (abbreviated 3-oxo-C6-HSL or simply AHL) could permeate through the separating oil phase and thus diffuse from one microcompartment into another. In this system, engineered “sender bacteria” in one droplet could communicate with “receiver bacteria” in neighbouring compartments.<sup>19,20</sup> Gene expression in bacteria equipped

<sup>a</sup> Technical University of Munich, Physics Department E14 and ZNN/WSL, Am Coulombwall 4a, 85748 Garching, Germany. E-mail: [simmel@tum.de](mailto:simmel@tum.de)

<sup>b</sup> Nanosystems Initiative Munich, Schellingstr. 4, 80539 München, Germany

† Electronic supplementary information (ESI) available: Supplementary methods, data, and modeling. See DOI: 10.1039/c5ib00301f

‡ Authors have contributed equally to this work.

with a genetic “AND gate” was switched on only in the presence of both IPTG and AHL containing reservoir droplets.

Compartmentalized bacterial consortia are of particular interest for applications in synthetic biology. For instance, compartmentalization could be used to create systems, in which several bacterial species interact and cooperate, which might be incompatible in co-culture (due to different growth conditions or predation of one species on the other). Furthermore, hybrid systems could be created, in which some droplets contain cell-free gene expression systems, while others contain bacteria, or simply nutrients or other chemicals. One vision for such systems could be the creation of a semi-synthetic super-organism composed of spatially arranged “droplet cells”, which have the ability of position-dependent gene expression, and thus spatial differentiation and pattern formation.<sup>21–23</sup>

In the present work we study spatially distributed gene expression in strictly linear arrangements of microdroplet compartments. A quasi one-dimensional geometry allows for a better control of boundary conditions, and also facilitates a straightforward analysis of the experiments. One of the most important aspects for our present study is the stronger mutual coupling of neighbouring compartments in a 1D geometry.

We not only studied microdroplets containing bacteria, but also emulsion droplets filled with cell-free gene expression systems<sup>24–29</sup> as well as hybrid systems. In experiments with compartmentalized bacteria, gene expression dynamics is strongly affected by bacterial cell growth in the droplets. By contrast, cell-free systems display different gene expression dynamics,<sup>30</sup> as the gene products are not diluted by cell growth. An obvious advantage of cell-free systems is the presence of the whole transcription and translation machinery and the simultaneous lack of an own genetic agenda. Cell-free systems can thus be programmed by simply feeding synthetic DNA without interference with an existing genetic background.<sup>24,26,31</sup> The scope of cell-free systems can be easily expanded by the addition of supplementary components such as enzymes and their substrates, crowding agents,<sup>32</sup> or other chemicals. Encapsulation of cell-free systems thus results in flexible biochemical compartments, which inherit some of their characteristics from bacteria. We demonstrate that in the context of our linear microdroplet geometries, cell-free and bacterial systems can be even made to communicate with each other.

## Results and discussion

Our experiments are based on two simple synthetic gene circuits. As explained in Fig. 1a, expression of green fluorescent protein (*GFPmut3\**) is activated only in the presence of both inducer molecules IPTG and AHL. In this respect, the gene construct on the reporter plasmid approximates the function of a logical AND gate. The second gene construct is termed “sender” since it can synthesize AHL in the presence of IPTG as shown in Fig. 1b. Operating the AND gate circuit within gradients of inducer molecules can be used to generate spatially differentiated gene expression. In order to study this effect, we produced

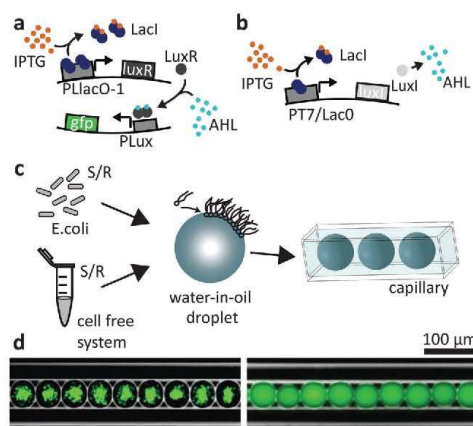


Fig. 1 Overview of genetic circuits and experimental setup. (a) A genetic AND gate that responds to the inducers IPTG and AHL: IPTG induces expression of the transcriptional activator LuxR, which is under the control of a lac promoter. Only in the presence of AHL, LuxR activates the expression of GFP, which is controlled by a lux promoter. (b) The sender circuit comprises a gene for the AHL synthase LuxI under the control of a lac promoter. Gene induction with IPTG leads to LuxI production and thus generation of the quorum sensing inducer AHL. (c) *E. coli* or cell-free systems with the AND gate or sender plasmid are encapsulated in water-in-oil droplets, which are arranged in a squared glass capillary (side length = 50  $\mu\text{m}$ ). (d) Fluorescence microscopy images of droplets in a glass capillary overlaid with inverted bright field images, which show the droplet surface and the capillary in white. Encapsulated *E. coli* bacteria (left) and cell-free systems (right) both contain the AND gate. The droplets are filled with 10 mM IPTG and 200 nM AHL, resulting in the expression of GFP (shown in green).

picolitre-sized emulsion droplets (diameter  $d \approx 40\text{--}50\text{ }\mu\text{m}$ ), containing either the cell free transcription/translation mix or bacteria using a microfluidic droplet generation system (see Experimental section). In order to create a linear arrangement of such compartments, the droplets were loaded into a squared capillary with a side length of 50  $\mu\text{m}$  (Fig. 1c and d). Hence, diffusion of inducer molecules was effectively confined to the dimension along the long axis of the capillary.

### Inducer response in the cell free system

We first studied the bulk response of the AND gate plasmid in the cell-free system to the inducer molecules IPTG and AHL in bulk in titration experiments (for the characterization in *E. coli* cf. ref. 18). To this end, we fitted the maximum rate of GFP expression as a function of the inducer concentrations with a Hill curve. We found that the response of the AND gate to varying concentrations of IPTG (for constant [AHL]) did not follow a typical induction behaviour. This may be caused by batch-to-batch variations of the cell-free system,<sup>33</sup> and is further related to the fact that in the cell-free system the concentration of the lac repressor LacI relative to the plasmid concentration (7.5 nM) is not sufficient<sup>26</sup> (Fig. S2, ESI†). By contrast, the AND gate displayed a proper, slightly cooperative



response to AHL (Hill exponent  $n \approx 1.8$ ) with an induction threshold of  $K_a \approx 9.9$  nM (Fig. S1, ESI†). These values are within the range previously found for AHL induction in bacteria.<sup>18</sup> In the cell-free context, further analysis therefore mainly focused on the response of the AND gate to AHL.

### 1D droplet chains connected to an inducer reservoir

In order to characterize the diffusion of the inducers within our 1D geometry, we studied the spatial variation of gene expression in the droplet chains as a function of only one of the two inducer molecules, *i.e.*, the AND gate droplets were only used as sensors or “receiver” droplets. The dispersed phase was first saturated with one of the inducers (either 200 nM AHL or 10 mM IPTG), and then a fixed concentration of the other inducer was established at one end of a droplet chain. This was accomplished by placing a droplet-filled capillary into a reservoir solution containing both the saturated and the second inducer molecule. The volume of the reservoir was created much larger than the interior volume of the capillary ( $V_{\text{reservoir}}/V_{\text{capillary}} \approx 10^3$ ). As the diffusion coefficient of the inducer inside the aqueous reservoir is much larger than the (apparent) diffusivity in the water-in-oil emulsion ( $D_{\text{reservoir}}/D_{\text{capillary}} > 10\text{--}100$ , *cf.* discussion below), the inducer concentration at the opening of the capillary can be assumed constant. Furthermore, due to the length of the capillaries ( $l \geq 1$  cm) and the time scale of our observations ( $t \leq 15$  h) one can safely assume zero inducer concentration sufficiently far inside the capillary. This will result in the formation of a gradient in the inducer concentration along the aligned droplets, which can be observed *via* GFP expression using an epifluorescence microscope.

A representative image time series recorded from cell-free receiver droplets inside a capillary connected to a reservoir with [AHL] = 1  $\mu\text{M}$  is shown in Fig. 2a. As AHL diffuses into the capillary, GFP expression is sequentially induced in the droplets, starting with the compartments closest to the reservoir. The temporal progress of GFP production as a function of distance to the reservoir (Fig. 2b) reflects the AHL dependence of GFP expression expected from the bulk experiments – larger distances correspond to lower AHL concentrations and thus slower expression kinetics. As the encapsulated cell-free system has a limited run-time of  $\approx 5\text{--}6$  hours, droplets at a distance too far to be reached by AHL within this time were not induced at all.

In fact, the number of droplets which are induced within a given time span can be simply controlled by the inducer concentration in the reservoir (Fig. 2c). Larger concentrations lead to larger diffusion fluxes, resulting in the induction of an increasing number of droplets. For large fluxes, however, the spatial differentiation of neighbouring droplets is less pronounced (Fig. S6, ESI†).

We found similar behaviour as in Fig. 2 also for linear chains of droplets filled with bacterial AHL receivers (Fig. S7, ESI†), but with slightly different dynamics, mainly due to bacterial growth within the droplets (*cf.* ref. 18).

Experiments with IPTG reservoirs of varying concentrations generally did not lead to a clear spatial differentiation (see Fig. S8, ESI† for [IPTG] = 10 mM), which presumably is caused

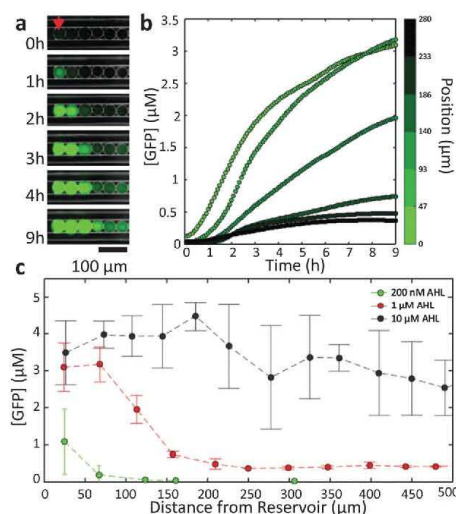


Fig. 2 AHL reservoir with cell-free droplets. (a) Fluorescence microscopy time series of droplets containing the cell-free gene expression system with the AND gate plasmid. The capillary is connected to a reservoir with [AHL] = 1  $\mu\text{M}$ . Reservoir and droplets are saturated with 10 mM IPTG. The first droplet at the oil/reservoir interface is marked with a red arrow at  $t = 0$  h. As AHL diffuses into the capillary the expression of GFP is induced (green). (b) Temporal progress of GFP expression in the droplets. The colour bar indicates the distance from the reservoir. Each data point is the average of two measurements. (c) GFP concentration at  $t = 9$  h in droplets as function of the distance from the capillary opening for three different AHL reservoir concentrations (dashed lines are guides for the eye). Each data point is the average of two to three different positions. Error bars indicate the standard deviation.

by the leakiness of the lac promoter and the lack of sufficient LacI for the cell-free system (*cf.* Fig. S2, ESI†).

### Quantitative considerations

For programmed pattern formation, it is of interest to tune the apparent diffusion coefficient of the “morphogens” and thus the corresponding patterning length scale. To this end a quantitative understanding of the diffusion properties of AHL within a heterogeneous medium such as a water-in-oil emulsion is necessary. We used the GFP expression strength in cell-free droplets as reporter for the local AHL concentration and estimated its apparent diffusion coefficient  $D_a$ . Surprisingly, for the reservoirs with [AHL] = 200 nM and [AHL] = 1  $\mu\text{M}$  we obtain values around  $D_a \approx 0.1 \mu\text{m}^2 \text{ s}^{-1}$ , while for the reservoir with [AHL] = 10  $\mu\text{M}$  we found a higher  $D_a$  of about  $\approx 25 \mu\text{m}^2 \text{ s}^{-1}$  (Fig. S3 and S4, ESI†). This discrepancy indicates that gene activation proceeds through different mechanisms for low and high reservoir concentrations.

In general, transport of molecules within a water-in-oil emulsion based on our specific surfactant and fluorocarbon oil is dominated by partitioning effects (the droplets are not expected to form adhesive bilayers at their interface,<sup>34</sup> for a discussion see ESI†). Thus, inducer molecules partition from

the reservoir into the oil phase, diffuse through the oil and then enter droplets in the capillaries. An alternative mechanism involves diffusive transport of inducer *via* surfactant micelles.<sup>35</sup> Whereas the diffusion coefficient through oil is expected to be reduced compared to the aqueous phase ( $D_{\text{aqueous}} \approx 100\text{--}1000 \mu\text{m}^2 \text{ s}^{-1}$ <sup>36–38</sup>) by a factor of  $\approx 4$  (due to its higher viscosity), diffusion *via* micelles has been measured to proceed with a diffusion coefficient of  $D_{\text{micelle}} \approx 1 \mu\text{m}^2 \text{ s}^{-1}$ .<sup>35</sup>

Apparently, for the lower reservoir concentrations ( $[\text{AHL}] = 200 \text{ nM}$ ,  $1 \mu\text{M}$ ) droplet induction is dominated by micelle diffusion. By contrast, for the  $[\text{AHL}] = 10 \mu\text{M}$  reservoir, a large enough amount of AHL partitions into the oil phase to elicit a “fast” and more global response in the capillaries (for a discussion see ESI†).

It is also important to consider effects, which are caused by the geometry of our experimental set-up. The linear arrangement of droplets in glass capillaries confines the inducer molecules to effectively diffuse in 1D and thus enforces their sequential diffusion through neighbouring droplets. In the absence of a bulk phase – acting as diffusion sink – this creates a relatively strong coupling between neighbouring droplets compared to other geometries. For instance, in a close-packed geometry an inducer-filled droplet is surrounded by two nearest neighbours in 1D, while it has six and even twelve neighbours in 2D and 3D, respectively, which would result in a correspondingly faster dilution. We can thus observe spatial effects over much longer distances in 1D than in our previous work based on a 2D arrangement of droplets in contact with a bulk oil phase.<sup>18</sup>

#### Inducer reservoir droplets

In the following set of experiments, we localized GFP expression by introducing inducer-filled reservoir droplets rather than using a macroscopic reservoir. To this end, one inducer was distributed globally to all droplets, while the second inducer was encapsulated only in dedicated droplets. In the presence of AHL sender droplets ( $[\text{AHL}] = 200 \text{ nM}$ ), GFP expression was induced only in nearest neighbour droplets containing bacteria and IPTG (Fig. 3a). In stark contrast, in the case of IPTG reservoir droplets ( $[\text{IPTG}] = 10 \text{ mM}$ ) GFP expression in droplets containing AND gate bacteria with saturating AHL concentration was not restricted to neighbouring droplets (Fig. 3b). However, in the absence of IPTG reservoir droplets in a capillary, no GFP production is observed at all. Using a combination of AHL and IPTG sender droplets, it was possible to spatially confine gene expression only to AND gate bacteria close to the reservoir droplets (Fig. 3c).

#### Communication between bacteria and artificial cellular compartments

We finally studied communication between the cell-free and bacterial droplets. As shown in Fig. 4a, cell-free sender droplets equipped with a LuxI encoding sender plasmid generate enough AHL to elicit a gene expression response in neighbouring droplets containing AND gate bacteria. To this end, the cell-free medium actually had to be supplemented with *S*-adenosyl methionine (SAM), which is a precursor for AHL not contained

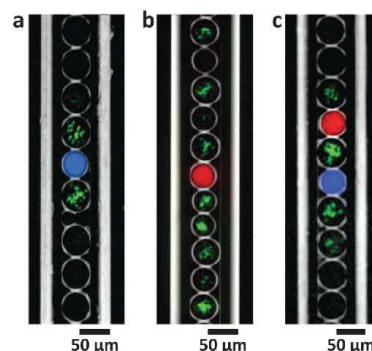


Fig. 3 Inducer reservoir droplets. Fluorescence microscopy images of bacterial AND gate droplets in the presence of (a) an AHL reservoir droplet (blue,  $[\text{AHL}] = 200 \text{ nM}$ ) with IPTG globally, (b) an IPTG reservoir droplet (red,  $[\text{IPTG}] = 10 \text{ mM}$ ) and AHL globally. (c) Gene expression of bacterial AND gate operated localized by a reservoir droplet of AHL (blue,  $[\text{AHL}] = 200 \text{ nM}$ ) and in the vicinity of IPTG reservoir droplet (red,  $[\text{IPTG}] = 10 \text{ mM}$ ).

in sufficient quantities in the conventional cell extract. In order to further increase the “sender strength” of the cell-free droplets, additional T7 RNA polymerase was added, which resulted in an enhanced production of LuxI (Fig. 4b and Fig. S1b, ESI†). The kymograph representation of Fig. 4a indicates that – as expected – the response is stronger and starts earlier in droplets in the direct vicinity of the cell free sender droplets.

We also found, that the intensity of the GFP signal was higher towards the end of the capillary compared with the centre (Fig. 4b). We assume that the growth of bacteria within the emulsion droplets is actually limited by the availability of oxygen. Since oxygen can dissolve and transfer through fluorinated oil, bacterial growth is prolonged towards the end of the capillaries, resulting in a stronger overall GFP production. This effect was not observed for cell-free gene expression in droplets.

The direction of communication can also be reversed by encapsulating LuxI producing sender bacteria that generate AHL and thus induce gene expression in cell-free receiver droplets (Fig. 4c). For “bacterial-to-cell-free” droplet communication, a clear difference between gene expression in nearest neighbour receivers and receivers more remote from the sender droplets could be resolved (Fig. 4d).

## Experimental

### Preparation of the cell-free gene expression system

Crude S30 cell extract was obtained by beat beating a BL21-Rosetta2(DE3) mid-log phase culture with 0.1 mm glass beads in a Minilys device (Peglab, Germany) as described in ref. 39. Instead of 3-phosphoglyceric acid (3-PGA), phosphoenolpyruvate (PEP) was utilized as an energy source<sup>40</sup> in the composite buffer (50 mM Hepes pH 8, 1.5 mM ATP and GTP, 0.9 mM CTP and UTP, 0.2 mg ml<sup>−1</sup> tRNA, 26 μM coenzyme A,



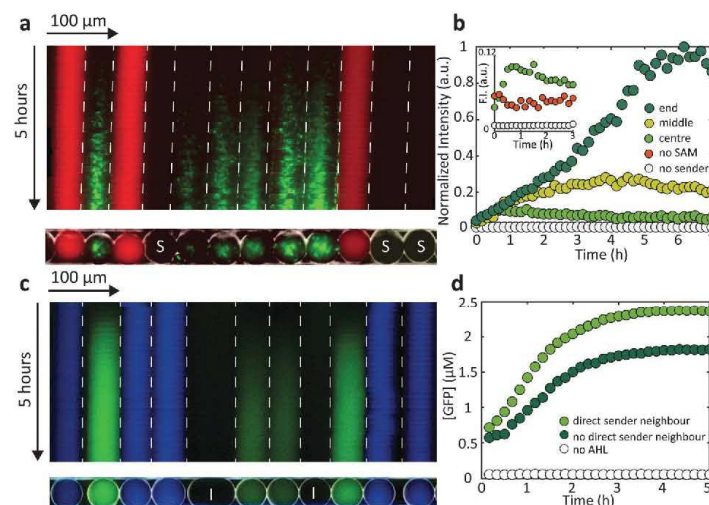


**Fig. 4** Communication between cell-free and bacterial droplets. (a) A kymograph of a fluorescence microscopy image of bacterial AND gate droplets (green), cell free sender droplets, with the sender plasmid (no colour) and IPTG inducer droplets (red, [IPTG] = 50 mM). Sender droplets produce AHL and activate GFP expression (green). (b) Time traces of normalized GFP fluorescence intensity of bacterial AND gate droplets averaged from  $\approx 20$  droplets for different positions inside the capillary. Prolonged bacterial growth, attributed to more oxygen towards the ends of the capillary increases the GFP signal. (c) Kymograph of a fluorescence microscopy image of cell free AND gate droplets activated by bacterial sender droplets (blue) and IPTG inducer droplets (no colour, [IPTG] = 50 mM). (d) Time traces of the GFP concentration in cell free AND gate droplets with and without AHL sender droplets as direct neighbours.

0.33 mM NAD, 0.75 mM cAMP, 68  $\mu$ M folic acid, 1 mM spermidine, 30 mM PEP, 1 mM DTT, 2% PEG-8000). All components were stored at  $-80^{\circ}\text{C}$  before thawing on ice. The composition of a single cell-free reaction was: 33% (v/v) S30 cell extract mixed with 42% (v/v) buffer and 25% (v/v) DNA plus additives. Each final reaction mix was supplemented with 13.3 mM maltose for ATP regeneration.<sup>41</sup> 300  $\mu$ M of *S*-(5'-adenosyl)-L-methionine chloride dihydrochloride (Sigma-Aldrich, #A7007) and 1  $\mu$ l of T7 polymerase (Epicentre, TM910K) was added to the cell free sender droplets. LacI was His-tagged and purified by gravity-flow chromatography with Ni-NTA Agarose Beads (Qiagen).

#### Bacterial strains and culture media

The receiver (AND gate) plasmid was cloned into *Escherichia coli* DH5 $\alpha$ Zi (ExpressSys) and the sender plasmid into *E. coli* BL21(DE3)pLysS (Promega) as described previously.<sup>18</sup> As culture media, Luria-Bertani (LB) medium (Carl Roth, #X968.1) and M9 minimal supplemented with 20 mM glucose and 300  $\mu$ g ml<sup>-1</sup> thiamine hydrochloride (Sigma-Aldrich, #T1270) were used. For IPTG reservoir experiments with AND gate bacteria, M9 minimal medium was supplemented with 0.4% (w/v) glycerol instead of glucose. Cells from glycerol stock were grown overnight in Falcon tubes with 5 ml LB medium containing 100  $\mu$ g ml<sup>-1</sup> carbenicillin (Carl Roth) and 30  $\mu$ g ml<sup>-1</sup> chloramphenicol (Carl Roth) at 37  $^{\circ}\text{C}$  shaken at 250 rpm. The overnight cultures were diluted to an initial optical density ( $\text{OD}_{600\text{nm}}$ ) of 0.01 in Falcon tubes containing fresh LB or M9 minimal medium (Sigma-Aldrich, #M6030) for

sender or receiver cells, respectively (LB medium is autofluorescent in the GFP channel) with 50% reduced antibiotic concentrations. Before encapsulation of bacteria into emulsion droplets, the cultures were incubated for 2–3 h until an  $\text{OD}_{600\text{nm}}$  of 0.1–0.2 was reached. Sender bacteria droplets were grown in LB medium supplemented with 1 mM IPTG, two hours before encapsulation.

#### Microfluidics

For the generation of droplets, we utilized a microfluidic flow-focusing geometry, which was defined using soft lithographic techniques and the elastomer polydimethylsiloxane (PDMS). PDMS devices were micromolded from silicon masters containing the channel structures, which were defined using the negative photoresist Epocore 20 (micro resist technology, Germany). The cured microfluidic device was bonded onto a glass cover slide after oxygen plasma treatment and baked at 200  $^{\circ}\text{C}$  for 3 hours.<sup>42</sup> To avoid cross contamination, each droplet species was produced in a separate device. Fluid flows were generated with a pressure controller OB-1K (Elveflow, France) and appropriate PTFE-tubings (inner diameter: 0.8 mm). Pressures were set between 150–300 mbar. The droplet device was loaded with the carrier oil Fluorinert FC-40 (Sigma-Aldrich, Germany) blended with 2% (w/w) surfactant (EA, RainDance Technologies, USA) and focused with the appropriate aqueous phase. The critical micelle concentration of the surfactant is  $\approx 0.02$ –0.04%.<sup>35</sup> The reservoirs and the collection tubes for the cell free system were placed on ice during droplet production. Different species of droplets were collected separately

and then mixed in a new test tube in defined volume ratios with a pipette. Filling of the capillaries with droplets is described in detail in the ESI† (Fig. S9). For capillary measurements with inducer reservoirs, the capillary ends were placed in a chamber containing the reservoir solution. The chamber was built with two stripes of melted parafilm on a glass slide, immediately covered with another glass slide. The chambers were sealed with silicone vacuum grease and nail polisher.

#### Bulk characterization

Cell-free expression of GFP was characterized *via* plate reader measurements (BMG FLUOstar Optima) using 15 µl reaction volumes in 384-well plates.

#### Microscopy

Video microscopy of droplets containing only bacteria was performed with an inverted epifluorescence microscope IX81 (Olympus, Japan) using a 10× magnification objective, an EMCCD camera (iXon3, Andor, UK), and a mercury fluorescence excitation light source (X-Cite 120Q, Excelitas Technologies, USA). The microscope was equipped with an incubator box (Okolab, Italy) to maintain a temperature of  $T = 37^\circ\text{C}$ . All time-lapse microscopy measurements containing the cell-free system, also in combination with bacteria, were conducted on an IX71 microscope (Olympus, Japan) using a 10× objective, a CCD camera (LucaR, Andor, UK) and a 4-wavelength fluorescence LED source (Thorlabs, USA). The samples were thermostatted at  $30^\circ\text{C}$  using a heating plate (Tokai Hit Co. Ltd, Japan).

#### Data analysis

Image analysis is performed using a customized automated droplet tracking software programmed in MATLAB.<sup>43</sup> Extracted fluorescence and position data was further processed as described in detail in S7, ESI†.

## Conclusions

We have demonstrated spatially differentiated gene expression in linear chains of emulsion droplets containing either bacteria or cell-free gene expression systems. Spatial effects can be either achieved by establishing concentration gradients of genetic inducers such as AHL and IPTG *via* macroscopic reservoirs or local sender droplets. For low inducer concentrations, the apparent diffusion coefficient of AHL is reduced by several orders of magnitude, consistent with micelle-mediated transport between neighbouring droplets. Confinement to an effective 1D geometry leads to a stronger chemical coupling of neighbouring droplets and an extended spatial range of the inducer molecules. This also enabled us to establish communication between cell-free sender droplets and neighbouring bacterial receiver droplets and, conversely, between sender bacteria and cell-free receivers.

Our experiments represent a step towards artificial multicellular hybrid systems, in which the “cells” are constituted either by encapsulated bacterial consortia, artificial cells containing

cell-free gene expression systems, or supplementary cells with chemical supplies, nutrients, *etc.* The 1D geometry utilized in this work could prove particularly useful to achieve spatial differentiation in such systems, to generate interesting spatiotemporal effects, and thus emulate simple developmental processes in an artificial context.

## Acknowledgements

We gratefully acknowledge financial support by the DFG Research Training Group GRK2062 “Molecular Principles of Synthetic Biology” and the DFG Cluster of Excellence NIM. We wish to thank Michael Heymann and Yannick Rondelez for useful experimental tips.

## References

- 1 F. J. H. Hol and C. Dekker, *Science*, 2014, **346**, 1251821.
- 2 J. C. W. Locke and M. B. Elowitz, *Nat. Rev. Microbiol.*, 2009, **7**, 383–392.
- 3 F. K. Balagadde, L. C. You, C. L. Hansen, F. H. Arnold and S. R. Quake, *Science*, 2005, **309**, 137–140.
- 4 M. R. Bennett and J. Hasty, *Nat. Rev. Genet.*, 2009, **10**, 628–638.
- 5 M. B. Elowitz, A. J. Levine, E. D. Siggia and P. S. Swain, *Science*, 2002, **297**, 1183–1186.
- 6 I. Golding, J. Paulsson, S. Zawilski and E. Cox, *Cell*, 2005, **123**, 1025–1036.
- 7 L. S. Tsimring, *Rep. Prog. Phys.*, 2014, **77**, 026601.
- 8 T. Danino, O. Mondragón-Palomino, L. Tsimring and J. Hasty, *Nature*, 2010, **463**, 326–330.
- 9 P. Wang, L. Robert, J. Pelletier, W. L. Dang, F. Taddei, A. Wright and S. Jun, *Curr. Biol.*, 2010, **20**, 1099–1103.
- 10 L. Boitard, D. Cottinet, C. Kleinschmitt, N. Bremond, J. Baudry, G. Yvert and J. Bibette, *Proc. Natl. Acad. Sci. U. S. A.*, 2012, **109**, 7181–7186.
- 11 J. E. Keymer, P. Galajda, C. Muldoon, S. Park and R. H. Austin, *Proc. Natl. Acad. Sci. U. S. A.*, 2006, **103**, 17290–17295.
- 12 J. E. Keymer, P. Galajda, G. Lambert, D. Liao and R. H. Austin, *Proc. Natl. Acad. Sci. U. S. A.*, 2008, **105**, 20269–20273.
- 13 J. Männik, R. Driessen, P. Galajda, J. E. Keymer and C. Dekker, *Proc. Natl. Acad. Sci. U. S. A.*, 2009, **106**, 14861–14866.
- 14 K. Drescher, Y. Shen, B. L. Bassler and H. A. Stone, *Proc. Natl. Acad. Sci. U. S. A.*, 2013, **110**, 4345–4350.
- 15 T. Kalisky and S. Quake, *Nat. Methods*, 2011, **8**, 311–314.
- 16 M. Nakano, J. Komatsu, S. Matsuura and K. Takashima, *et al.*, *J. Biotechnol.*, 2003, **102**, 117–124.
- 17 R. Williams, S. G. Peisajovich, O. J. Miller, S. Magdassi, D. S. Tawfik and A. D. Griffiths, *Nat. Methods*, 2006, **3**, 545–550.
- 18 M. Weitz, A. Mückl, K. Kapsner, R. Berg, A. Meyer and F. C. Simmel, *J. Am. Chem. Soc.*, 2014, **136**, 72–75.
- 19 R. Weiss, T. F. Knight, A. E. Condon and G. Rozenberg, *DNA Computing, 6th International Workshop on DNA-Based Computers, DNA6*, 2000, **2054**, 1–16.

- 20 R. Weiss, S. Basu, S. Hooshangi, A. Kalmbach, D. Karig, R. Mehreja and I. Netravali, *Nat. Comput.*, 2003, **2**, 47–84.
- 21 M. Isalan, C. Lemerle and L. Serrano, *PLoS Biol.*, 2005, **3**, 488–496.
- 22 S. Basu, Y. Gerchman, C. H. Collins, F. H. Arnold and R. Weiss, *Nature*, 2005, **434**, 1130–1134.
- 23 J. J. Tabor, H. M. Salis, Z. B. Simpson, A. A. Chevalier, A. Levskaya, E. M. Marcotte, C. A. Voigt and A. D. Ellington, *Cell*, 2009, **137**, 1272–1281.
- 24 Y. Shimizu, A. Inoue, Y. Tomari, T. Suzuki, T. Yokogawa, K. Nishikawa and T. Ueda, *Nat. Biotechnol.*, 2001, **19**, 751–755.
- 25 V. Noireaux, R. Bar-Ziv and A. Libchaber, *Proc. Natl. Acad. Sci. U. S. A.*, 2003, **100**, 12672–12677.
- 26 J. Shin and V. Noireaux, *ACS Synth. Biol.*, 2012, **1**, 29–41.
- 27 Z. Z. Sun, C. A. Hayes, J. Shin, F. Caschera, R. M. Murray and V. Noireaux, *J. Visualized Exp.*, 2013, 1–15, DOI: 10.3791/50762.
- 28 E. Sokolova, E. Spruijt, M. M. K. Hansen, E. Dubuc, J. Groen, V. Chokkalingam, A. Piruska, H. A. Heus and W. T. S. Huck, *Proc. Natl. Acad. Sci. U. S. A.*, 2013, **110**, 11692–11697.
- 29 P. Torre, C. D. Keating and S. S. Mansy, *Langmuir*, 2014, **30**, 5695–5699.
- 30 H. Niederholtmeyer, V. Stepanova and S. J. Maerkl, *Proc. Natl. Acad. Sci. U. S. A.*, 2013, **110**, 15985–15990.
- 31 D. C. Harris and M. C. Jewett, *Curr. Opin. Biotechnol.*, 2012, **23**, 672–678.
- 32 C. Tan, S. Saurabh, M. P. Bruchez, R. Schwartz and P. Leduc, *Nat. Nanotechnol.*, 2013, **8**, 602–608.
- 33 M. K. Takahashi, J. Chappell, C. A. Hayes, Z. Z. Sun, J. Kim, V. Singhal, K. J. Spring, S. Al-Khabouri, C. P. Fall, V. Noireaux, R. M. Murray and J. B. Lucks, *ACS Synth. Biol.*, 2015, **4**, 503–515.
- 34 A. R. Thiam, N. Bremond and J. Bibette, *Langmuir*, 2012, **28**, 6291–6298.
- 35 Y. Skhiri, P. Gruner, B. Semin, Q. Brosseau, D. Pekin, L. Mazutis, V. Goust, F. Kleinschmidt, A. El Harrak, J. B. Hutchison, E. Mayot, J.-F. Bartolo, A. D. Griffiths, V. Taly and J.-C. Baret, *Soft Matter*, 2012, **8**, 10618.
- 36 W. S. Choi, D. Ha, S. Park and T. Kim, *Biomaterials*, 2011, **32**, 2500–2507.
- 37 G. Dilanji, J. Langebrake, P. De Leenheer and S. Hagen, *J. Am. Chem. Soc.*, 2012, **134**, 5618–5626.
- 38 B. A. Hense, J. Müller, C. Kuttler and A. Hartmann, *Sensors*, 2012, **12**, 4156–4171.
- 39 Z. Z. Sun, C. A. Hayes, J. Shin, F. Caschera, R. M. Murray and V. Noireaux, *J. Visualized Exp.*, 2013, e50762, DOI: 10.3791/50762.
- 40 D.-M. Kim and J. R. Swartz, *Biotechnol. Bioeng.*, 2001, **74**, 309–316.
- 41 F. Caschera and V. Noireaux, *Biochimie*, 2014, **99**, 162–168.
- 42 S. Kaneda, K. Ono, T. Fukuba, T. Nojima, T. Yamamoto and T. Fujii, *Anal. Sci.*, 2012, **28**, 39.
- 43 K. Kapsner and F. C. Simmel, *ACS Synth. Biol.*, 2015, **4**, 1136–1143.



### 3 Discussion

#### 3.1. Gene induction quantitation at the single cell level

In this section, I discuss the relations and consequences between gene expression at the single-cell level and cell-to-cell variability. We quantitatively determined the dynamic gene expression of receiver bacteria responding to the quorum sensing inducer N-3-oxo-C6-homoserine lactone (AHL) upon gene activation via the lux promoter ( $p_{lux}$ ). In microfluidic chemostats, we monitored the expression of green fluorescence protein (GFP) on the single cell level. We quantified in a further study, the reversibly switching of filamentation in *E. coli* cells based on a QS controllable CRISPR/dCas9 gene circuit.

We determined bacterial lineages and subpopulations with distinct induction behavior within a heterogeneous population of AHL/ $p_{lux}$  receiver bacteria. We obtained response curves for single cell trajectories as well as from bulk characterization (microtiter plate (MTP) experiments). The mean behavior from the total microchamber population well agreed with those obtained from bulk gene expression, although the induction threshold in the chemostat was lower than in bulk. This difference may be caused by an individual physiological state that cells experience in the microfluidic setup compared to MTP experiments. Microfluidic approaches prevent the accumulation of waste products and thus provide controllable cellular microenvironments.

As in our study, typical values of the AHL/ $p_{lux}$  system have been found also in other quantitative studies and resulted in cooperativity exponents of around 1 – 1.5 and activation thresholds in the range of 5 – 15 nM (4,222,223). The identified Hill exponent for the average expression rates of single cell data proved to be more cooperative than in bulk determination. For this, the evaluation was performed with the dominant homogenous subpopulation, extracted by a Gaussian fit from a time-dependent probability histogram of the fluorescence level, comprising the entire population at a constant induction level (50 nM AHL). This resulting lognormal probability (logarithmic scale on x-axis) precisely coincides with the main subpopulation distribution. From the theoretical perspective, lognormal distributions can be applied to describe the quantity in stochastic systems such as bacteria, because the steady-state concentration of the fluorescent protein GFP is determined by several independent kinetic rates that do not correlate much under statistical considerations (224,225). In this case, the limiting distribution comprises four rates, the ones for mRNA synthesis and degradation as well as protein translation and degradation. May also other distributions such as the negative binominal (226) and the Gamma distribution (227) apply under certain assumptions to depict gene expression variability. Indeed, in our study, a small fraction of bacterial cells appeared to respond much later and with less gene activation to the provided autoinducer molecules. The time-dependence of those ‘late inducers’ was clearly visible from single cell data, but was not described by lognormal function covering the majority of the cells. We could attribute this behavior to a strongly reduced growth rate and therefore excluded these slow-growing cells from further analysis of the noise characteristics and focused on the dominant bacterial part of the distribution which reflects in our opinion the ‘most reliable’ parameters for quantitation. The sharper response curve for single cell data and the corresponding larger Hill exponent can be traced back to the fact that the late inducer cells effectively lowers the measured average fluorescence, resulting in a more gently rising transfer curve. Thus, we limited our

calculations on receiver cells that showed specific induction behavior and homogenous expression levels.

Factors that contribute to noise can be from intrinsic or extrinsic nature (126). The square of the coefficient of variation (fractional noise) is often used to distinguish between both. We could attribute gene expression noise in receiver bacteria to extrinsic factors, which is consistent with previous studies of other bacterial communication systems (4). However, to our surprise, we observed a linear increase of the fractional noise with the mean, during the period of gene expression initiation. In this ‘out of steady-state’ phase, the scaling laws corresponding to intrinsic and extrinsic noise do not apply. In this case, the predicted behavior for the fractional noise should decline as the mean expression level rises (227). Nonetheless, gene induction behavior depends on many factors including the dynamics of the used reporter system which might lead to various unspecific phenotypes that are challenging to capture by a simple mathematical model.

As we considered in our model parameters, Ozbudak et al. (228) have shown that the quantity of noise depends on the relationship between transcription and translation rates. At high transcription rate, the resulting variability in protein levels is low, but when transcription is slowed down and the translation rate is raised, the stochastic gene expression profile gets far noisier, even when the mean expression level remains unchanged (228). Thus, experimental data on mRNA levels could help to understand more deeply the behavior of our system. However, after the initial induction process, the fractional noise followed a common extrinsic scaling behavior. Even though, we could assign noise to its conceptually origin, multiple other factors can contribute or prevent gene expression variability. Interestingly, genes involved in essential cellular functions such as protein synthesis and degradation have been reported to be much less variable (229). In special, this is often attributed to cells that inhere a circadian rhythm or other oscillatory networks. Such a robustness implies that crucial tasks require and possess techniques, that precisely control protein output levels (67). In fact, mechanisms that minimize or compensate noise and thus cell-to-cell variability in gene expression have been identified in their natural context. This include, for instance, negative feedback systems which have been proved to be valuable instruments to reduce noise (230). It would be interesting to implement an autoregulation system in our sender-receiver cells based on a second QS signal type.

Next to the quantitation of noise, we determined the effective AHL concentration sensed between an AHL-producing sender strain and receiver cells, co-cultured in a microfluidic chamber. The AHL synthase LuxI and a red fluorescent marker protein (RFP) were encoded on a plasmid. Thus, sender cells equipped with this plasmid locally produced the QS signal molecule inducing GFP expression in the receiver cells. We exploited the receiver cells as a simple sensor for *in situ* AHL detection. Our approach allows the comparison of data from two different experiments or the evaluation whether two experiments are comparable at all. To do so, we considered a variety of issues such as the sender/receiver ratio, the growth of both individual strains as well as the expression rates of our reporter proteins in our dynamic system. We resorted to a gene expression model that bundled these experimental parameters into a single variable that grows quadratically with time. We could relate any experimentally determined GFP expression rate to the effective amount of AHL via the introduced variable.

### 3.2. AHL mediated communication in microenvironments

In our work, we quantitatively elucidate AHL mediated quorum sensing through micro-emulsion droplets. We performed a number of different communication modes between bacteria and cell-free compartments with the goal to send and receive the signal molecules between neighboring confinements. The communication system was arranged in large arrays of droplets and in one-dimensional droplet chains.

We have shown that inducer molecules possessing an amphiphilic character such as the quorum sensing signal 3-oxo-C6-HSL (AHL) or the frequently applied inducer IPTG can establish chemical communication between inducer reservoirs and small groups of bacteria confined within water-in-oil emulsion droplets. In the distance-dependent gene expression experiments, we found reduced effective diffusion coefficient ( $D_{\text{eff}}$ ) over orders of magnitude for IPTG ( $D_{\text{eff}} = 0.05 \mu\text{m}^2/\text{s}$ ) and for AHL ( $D_{\text{eff}} = 2.0 \mu\text{m}^2/\text{s}$ ) at the first instance. In agreement with a higher octanol/water (ow) partitioning coefficient for AHL, we found a higher value for the effective diffusion coefficient for the QS molecule than for IPTG. In aqueous medium, the typical values for diffusivity of small molecules can be expected between  $100 - 1000 \mu\text{m}^2/\text{s}$  (8,231,232).

The dynamic viscosity of the fluorinated oil with a value of 4.1 mPa/s (110,233) can only explain reduction of diffusivity at the order of 4. In another scenario, the formation of surfactant bilayers between adjacent droplets can reduce the diffusivity proportional to the ratio of the droplet radius to their contact area (234). Indeed, the permeability between droplets principally depends on the partitioning between the oil and the water phase, which in turn is a result of the surfactant concentration. The chemical properties of the surfactant, however, do not expect bilayer formation at the droplet interface. The copolymeric tail moieties, arranged in triblocks, were designed for optimal emulsion stability and solubility in the continuous phase (110), reducing the adhesion energy between the monolayers (235). The droplet boundaries are further stabilized by uncharged head groups, which are unlikely to hinder diffusion (236).

Thus, we thought, a more elaborate droplet arrangement technique and an expanded experimental setup would be required to describe the diffusion properties of inducer compounds through the heterogeneous environment of water-in-oil emulsions.

Consequently, in our linear droplet setup within capillaries, we shed light on the dissemination of AHL through the emulsions. Our data indicated that gene activation in the droplets proceeds probably by two mechanisms for low and high inducer concentrations. The dominant mode for AHL concentrations above  $10 \mu\text{M}$  is partitioning from the reservoir into the oil and back into the aqueous phase of droplets in direct vicinity, sequentially inducing the inclosing receiver unit. The resulting apparent diffusion coefficient ( $D_a$ ) of around  $25 \mu\text{m}^2/\text{s}$  can be explained by the decrease of diffusivity due to the viscosity of the oil under the assumption that  $D_a$  is proportional to  $D_{\text{oil}}$  and thus predominantly depends on the permeability even though partition constants are low (237). By contrast, if partitioning into the oil is too low for low inducer concentrations, the alternative mechanism involves micelle-mediated transport (95). A typical diffusion coefficient for surfactant micelles is in the range of  $D_{\text{micelles}} = 1 \mu\text{m}^2/\text{s}$  (237). In our study, applied AHL concentrations up to  $1 \mu\text{M}$  displayed  $D_{\text{eff}} = 0.1 \mu\text{m}^2/\text{s}$ . Thus, the discrepancies between the apparent diffusion coefficients for high and low reservoir concentrations may assign to the different dissemination processes. The number of droplets in a series which are induced within a given time span can be simply controlled by the initial inducer concentration at the capillary inlet. However, bacterial growth influences gene expression dynamics. We observed prolonged growth of bacteria next to the ends of capillaries than in the center. The

fluorinated oil has biocompatible properties and allows oxygen solubility and transfer (110), which influences growth of cells and thus expression dynamics. By contrast, cell-free gene expression in droplets did not show oxygen dependent behaviors. However, in encapsulated cell-free systems, depletion of resources and the accumulation of waste products is critical. Thus, we applied reaction-diffusion models only to the first 2h of the reaction. In principal, effects, which are caused by the reaction progress can be mathematically considered by time-dependent reaction constants. Depletion of AHL due to reversible binding to LuxR and degradation can be estimated by the consideration of the known dissociation constants and degradation rates for cell-free systems. Taking such temporary immobilized AHL into account under the assumption that LuxR concentrations maximal reach the micromolar range, the influence on the determined apparent diffusion coefficients at low inducer concentrations is negligible. The viscosity of the cell-free systems should be comparable to that of the *E. coli* cytoplasm. The molecular diffusion coefficients would be reduced by factors between 2 and 5 in cell-free droplets (238). In a loose sense, the cell-free compartments also imitate life-like behavior by producing or detecting information of contextual meaning.

As a perspective, our findings could help to continue experimental studies to debate about the purpose of quorum sensing and its evolutionary origin. For this an artificial environment such as microfluidics or encapsulation methods provide well-defined setups for a consortium of bacterial cells and QS mimicking systems such as cell-free reactions that communicate.

We presume that also other small molecules with amphiphilic character, like antibiotics, antioxidants, amino acids and many other biological active compounds can be disseminated across the compartments. Chloramphenicol, for instance, has a partitioning coefficient of  $\log K_{ow} = 1.14$  which is in the same range as AHL. The essential amino acid tryptophan displays a  $\log P_{ow}$  value of -1.06 which is higher than for IPTG ( $\log P_{ow} = 1.26$ ). If micelle-mediated transport is envisioned suitable concentration ranges could be determined for intended substances.

Moreover, various cell-like units can be arranged between bacteria and artificial cellular compartments. We demonstrated the potential for pattern formation and differentiation studies in a semi-synthetic organism consisting of spatially separated ‘droplet cells’. In principle, different species of bacteria could be prepared in individual droplet microreactors, and, although isolated from direct physical contact, their interaction studied due to the exchange of diffusible goods. With smaller diffusivity than in aqueous solutions, stable patterns at reduced length scale might be established. Other concepts include pattern formation studies in concepts with different strains in the same microenvironment that build commensal relationships, for instance.

The fact that a group of bacteria send or receive chemical signals in compartments helps to average out fluctuations, caused by single cell variability (67). Previous studies on distributed computing based on spatially separated, communicating microcolonies (55,58) have emphasized averaging, which makes bacterial computation more robust than alternative concepts based on intracellular (single cell) computing (7). A general drawback of artificial biological computers is speed, which can span over a wide range of timescales. The concept of heterotic computing (239), the rational combination of various computational pieces such as biological devices embedded in chemical solutions and wired to silicone- or quantum-based systems, can be used to exploit their individual strength and address future demands. Such combined substrates, assembled in series or in parallel can lead to novel hybrid computational systems. A distributed, artificial bacterial computer implemented in microemulsions potentially could be faster and operate with reduced space requirements.

## 4 References

1. Eldar A, Elowitz MB. Functional roles for noise in genetic circuits. *Nature*. 2010;467(7312):167–73.
2. Waters CM, Bassler BL. Quorum sensing: cell-to-cell communication in bacteria. *Annu Rev Cell Dev Biol*. 2005;21:319–46.
3. Cox CD, Peterson GD, Allen MS, Lancaster JM, McCollum JM, Austin D, et al. Analysis of Noise in Quorum Sensing. *OMICS: A Journal of Integrative Biology*. 2003 Sep 26;7(3):317–34.
4. Long T, Tu KC, Wang Y, Mehta P, Ong NP, Bassler BL, et al. Quantifying the Integration of Quorum-Sensing Signals with Single-Cell Resolution. Kishony R, editor. *PLoS Biol*. 2009 Mar 24;7(3):e1000068.
5. Wang Y, Tu KC, Ong NP, Bassler BL, Wingreen NS. Protein-Level Fluctuation Correlation at the Microcolony Level and Its Application to the *Vibrio harveyi* Quorum-Sensing Circuit. *Biophysical Journal*. Biophysical Society; 2011 Jun 22;100(12):3045–53.
6. Ramalho T, Meyer A, Mückl A, Kapsner K, Gerland U, Simmel FC. Single Cell Analysis of a Bacterial Sender-Receiver System. Meijler MM, editor. *PLoS ONE*. 2016 Jan 25;11(1):e0145829.
7. Weitz M, Mückl A, Kapsner K, Berg R, Meyer A, Simmel FC. Communication and Computation by Bacteria Compartmentalized within Microemulsion Droplets. *J Am Chem Soc*. 2014 Jan 8;136(1):72–5.
8. Choi WS, Ha D, Park S, Kim T. Biomaterials. *Biomaterials*. Elsevier Ltd; 2011 Apr 1;32(10):2500–7.
9. Whitaker RD, Pember S, Wallace BC. Single cell time-resolved quorum responses reveal dependence on cell density and configuration. *Journal of Biological ....* 2011.
10. Bai Y, Patil S, Bowden S, Poulter S, Pan J, Salmond G, et al. Intra-Species Bacterial Quorum Sensing Studied at Single Cell Level in a Double Droplet Trapping System. *IJMS*. 2013;14(5):10570–81.
11. Schwarz-Schilling M, Aufinger L, Mückl A, Simmel FC. Integrative Biology. *Integrative Biology*. Royal Society of Chemistry; 2016 Jan 17;;1–7.
12. Porcar M, Peretó J. *Synthetic Biology*. Springer; 2014. 1 p.
13. Pieper DH, Reineke W. Engineering bacteria for bioremediation. *Current Opinion in Biotechnology*. 2000.
14. Way JC, Collins JJ, Keasling JD, Silver PA. Integrating Biological Redesign: Where Synthetic Biology Came From and Where It Needs to Go. *CELL*. Elsevier Inc; 2014 Mar 27;157(1):151–61.
15. Benner SA, Yang Z, Chen F. Synthetic biology, tinkering biology, and artificial biology. What are we learning? *Comptes rendus - Chimie*. Academie des sciences; 2010 Aug 4;;1–16.
16. Lee SY, Park JM, Kim TY. Application of Metabolic Flux Analysis in Metabolic Engineering. 1st ed. Vol. 498, *Synthetic Biology Part B*. Elsevier Inc; 2011. 27 p.
17. Salis HM, Mirsky EA, Voigt CA. Automated design of synthetic ribosome binding sites to control protein expression. *Nature Biotechnology*. 2009;27(10):946–50.
18. Salis HM. The Ribosome Binding Site Calculator. 1st ed. Vol. 498, *Synthetic Biology Part B*. Elsevier Inc; 2011. 24 p.
19. Guimaraes JC, Rocha M, Arkin AP, Cambray G. D-Tailor: automated analysis and design of DNA sequences. *Bioinformatics*. 2014;30(8):1087–94.
20. Tinberg CE, Khare SD, Dou J, Doyle L, Nelson JW, Schena A, et al. Computational design of ligand-binding proteins with high affinity and selectivity. *Nature*. Nature Publishing Group; 2013 Sep 4;501(7466):212–6.
21. Robinson-Mosher A, Shinar T, Silver PA, Way J. Dynamics simulations for engineering macromolecular interactions. *Chaos*. 2013 May 31;23(2):025110–0.

## References

22. Juty N, Ali R, Glont M, Keating S, Rodriguez N, Swat MJ, et al. BioModels: Content, Features, Functionality, and Use. *CPT Pharmacometrics Syst Pharmacol*. 2015 Feb 26;4(2):55–68.
23. Kahl LJ, Endy D. A survey of enabling technologies in synthetic biology. *J Biol Eng*. 2013 May 10;7(1):13.
24. Leduc S. La biologie synthétique. A. Poinat; 1912.
25. Friedrich W, Knipping P, Laue M. Interferenzerscheinungen bei Röntgenstrahlen. *Annalen der Physik*. 1913.
26. Laue von M. Concerning the detection of X-ray interferences. Nobel lecture; 1915.
27. Bernal JD, Hodgkin DC. X-Ray Photographs of Crystalline Pepsin. *Nature*. London; 1934 Feb 19;:794–5.
28. FRANKLIN RE, GOSLING RG. Molecular configuration in sodium thymonucleate. *Nature*. 1953 Apr;171(4356):740–1.
29. WATSON JD, CRICK FH. Molecular structure of nucleic acids; a structure for deoxyribose nucleic acid. *Nature*. 1953 Apr;171(4356):737–8.
30. Oparin AI. *The Origin of Life*. Courier Corporation; 1924. 1 p.
31. Rode BM, Fitz D, Jakschitz T. The first steps of chemical evolution towards the origin of life. *Chem Biodivers*. 2007 Nov 30;4(12):2674–702.
32. Pross A, Pascal R. The origin of life: what we know, what we can know and what we will never know. *Open Biology*. 2013 Mar 6;3(3):120190–0.
33. BESSMAN MJ, LEHMAN IR, SIMMS ES, KORNBERG A. Enzymatic synthesis of deoxyribonucleic acid. II. General properties of the reaction. *J Biol Chem*. 1958 Jul;233(1):171–7.
34. Olivera BM, Scheffler IE, LEHMAN IR. Enzymic joining of polynucleotides. IV. Formation of a circular deoxyadenylate-deoxythymidylate copolymer. *Journal of Molecular Biology*. 1968 Sep;36(2):275–85.
35. MONOD J, JACOB F. Teleonomic mechanisms in cellular metabolism, growth, and differentiation. *Cold Spring Harb Symp Quant Biol*. 1961;26:389–401.
36. Szybalska EH, Szybalski W. GENETICS OF HUMAN CELL LINES, IV. DNA-MEDIATED HERITABLE TRANSFORMATION OF A BIOCHEMICAL TRAIT.
37. Smith HO, Wilcox KW. A restriction enzyme from *Hemophilus influenzae*. I. Purification and general properties. *Journal of Molecular Biology*. 1970 Jul 27;51(2):379–91.
38. Smith HO, Kelly TJ. A restriction enzyme from *Hemophilus influenzae*. II. Base sequence of the recognition site. *Journal of Molecular Biology*; 1970.
39. Szybalski W, Skalka A. Nobel prizes and restriction enzymes. *Gene*. 1978 Nov;4(3):181–2.
40. Mullis KB, Faloona FA. Specific synthesis of DNA in vitro via a polymerase-catalyzed chain reaction. *Methods Enzymol*. 1987;155:335–50.
41. Venter JC, Adams MD, Myers EW, Li PW, Mural RJ, Sutton GG, et al. The Sequence of the Human Genome. *Science*. 2001 Feb;291(5):1304–51.
42. RAWIS RL. “Synthetic Biology” Makes Its Debut. *Chem Eng News*. 2000 Apr 24;78(17):49–53.
43. Elowitz MB, Leibler S. A synthetic oscillatory network of transcriptional regulators. *Nature*. Nature Publishing Group; 2000;403(6767):335–8.
44. Agarwal KL, Büchi H, Caruthers MH, Gupta N. Total synthesis of the gene for an alanine transfer ribonucleic acid from yeast. *Nature*. 1970.
45. Gibson DG, Glass JI, Lartigue C, Noskov VN, Chuang R-Y, Algire MA, et al. Creation of a bacterial cell controlled by a chemically synthesized genome. *Science*. 2010 Jul 1;329(5987):52–6.
46. Nielsen DR. Engineering microbial chemical factories to produce renewable “biomonomers.” 2012 Aug 28;:1–12.
47. Jinek M, Chylinski K, Fonfara I, Hauer M, Doudna JA, Charpentier E. A programmable dual-RNA-guided DNA endonuclease in adaptive bacterial immunity. *Science*. American Association for the Advancement of Science; 2012;337(6096):816–21.

48. Cyranoski D. CRISPR gene-editing tested in a person for the first time. *Nature*. 2016 Nov 24;:479.
49. Szybalski W. In vivo and in vitro initiation of transcription. *Adv Exp Med Biol*. 1974 Jun;44(1):23–4.
50. Mitchell M. Ubiquity symposium: Biological Computation. *Ubiquity*. ACM; 2011;2011(February).
51. Weitz M. Compartmentalization of Synthetic Biochemical Systems. Dissertation, Technical University of Munich, Physics Department. 2014 Jul 1;:1–189.
52. Fellermann H, Markovitch O, Gilfellow O, Madsen C, Phillips A. Toward Programmable Biology. *ACS Synth Biol*. 2016 Aug 19;5(8):793–4.
53. Benenson Y. Biomolecular computing systems: principles, progress and potential. *Nat Rev Genet*. Nature Publishing Group; 2012 Jun 12;13(7):455–68.
54. Cardelli L, Hernansaiz-Ballesteros RD, Dalchau N, Csikász-Nagy A. Efficient Switches in Biology and Computer Science. Stelling J, editor. *PLoS Comput Biol*. 2017 Jan 5;13(1):e1005100.
55. Tamsir A, Tabor JJ, Voigt CA. Robust multicellular computing using genetically encoded NOR gates and chemical “wires.” *Nature*. 2011 Dec 16;469(7329):212–5.
56. Gardner TS, Cantor CR, Collins JJ. Construction of a genetic toggle switch in *Escherichia coli*. *Nature*. 2000;403:339–42.
57. Friedland AE, Lu TK, Wang X, Shi D, Church G, Collins JJ. Synthetic Gene Networks That Count. *Science*. 2009 May 28;324(5931):1199–202.
58. Regot S, Macia J, Conde N, Furukawa K, Kjellén J, Peeters T, et al. Distributed biological computation with multicellular engineered networks. *Nature*. 2011 Dec 16;469(7329):207–11.
59. Farzadfard F, Lu TK. Genomically encoded analog memory with precise in vivo DNA writing in living cell populations. *Science*. 2014 Nov 13;346(6211):1256272–2.
60. Wong Ng J, Chatenay D, Robert J, Poirier MG. Plasmid copy number noise in monoclonal populations of bacteria. *Phys Rev E*. 2010 Jan 14;81(1):011909.
61. Raser JM, O’Shea EK. Noise in gene expression: origins, consequences, and control. *Science*. 2005;309(5743):2010–3.
62. Munsky B, Neuert G, van Oudenaarden A. Using gene expression noise to understand gene regulation. *Science*. 2012 Apr 12;336(6078):183–7.
63. Mitchell M. Complex systems - Network thinking. *Artif Intell*. 2006.
64. Hermoso SM. Synchronization and Chip Multiprocessing (CMP). 2006.
65. Zhang M, Shanbhag NR. Soft-Error-Rate-Analysis (SERA) Methodology. *IEEE Trans Comput-Aided Des Integr Circuits Syst*. 25(10):2140–55.
66. Amir Hosseini TRYM. A Fault-Aware Dynamic Routing Algorithm for On-Chip Networks. 2008 Apr 24;:1–4.
67. Raj A, van Oudenaarden A. Nature, Nurture, or Chance: Stochastic Gene Expression and Its Consequences. *CELL*. 2008 Oct;135(2):216–26.
68. SUGITA M. Functional analysis of chemical systems in vivo using a logical circuit equivalent. *J Theor Biol*. 1961 Oct;1:415–30.
69. Adleman LM. Molecular computation of solutions to combinatorial problems. *Science*. 1994 Nov 10;266(5187):1021–4.
70. Wang X, Liu J, Zheng Y, Li J, Wang H, Zhou Y, et al. An optimized yeast cell-free system: Sufficient for translation of human papillomavirus 58 L1 mRNA and assembly of virus-like particles. *Journal of Bioscience and Bioengineering*. 2008 Jul;106(1):8–15.
71. Guild K, Zhang Y, Stacy R, Mundt E, Benbow S, Green A, et al. laboratory communications. *Acta Cryst* (2011) F67, 1027–1031 [doi:101107/S1744309111032143]. International Union of Crystallography; 2011 Aug 31;:1–5.
72. Stech M, Quast RB, Sachse R, Schulze C, Wüstenhagen DA, Kubick S. A Continuous-Exchange Cell-Free Protein Synthesis System Based on Extracts from Cultured Insect Cells. Preiss T, editor. *PLoS ONE*. 2014 May 7;9(5):e96635.
73. Caschera F, Noireaux V. Preparation of amino acid mixtures for cell-free expression systems. *Biotech*. 2014 Dec 31;58(1):40–3.

## References

74. Zubay G, Lederman M, DeVries JK. DNA-directed peptide synthesis. 3. Repression of beta-galactosidase synthesis and inhibition of repressor by inducer in a cell-free system. *Proc Natl Acad Sci U S A*. 1967 Oct;58(4):1669–75.
75. Roberts BE, Gorecki M, Mulligan RC, Danna KJ, Rozenblatt S, Rich A. Simian virus 40 DNA directs synthesis of authentic viral polypeptides in a linked transcription-translation cell-free system. *Proc Natl Acad Sci U S A*. 1975 Apr 30;72(5):1922–6.
76. Steggles AW, Wilson GN, Kantor JA. Cell-free transcription of mammalian chromatin: transcription of globin messenger RNA sequences from bone-marrow chromatin with mammalian RNA polymerase. 1974.
77. Reichman M, Penman S. Stimulation of polypeptide initiation in vitro after protein synthesis inhibition in vivo in HeLa cells. *Proc Natl Acad Sci U S A*. 1973 Sep;70(9):2678–82.
78. Nevin DE, Pratt JM. A coupled in vitro transcription-translation system for the exclusive synthesis of polypeptides expressed from the T7 promoter. *FEBS Letters*. 1991.
79. Tabor S. Expression using the T7 RNA polymerase/promoter system. *Curr Protoc Mol Biol*. 2001 May;Chapter 16:Unit16.2.
80. Jewett MC. Non-standard amino acid incorporation into proteins using *Escherichia coli* cell-free protein synthesis. 2014 Jun 4;:1–7.
81. Shimizu Y, Inoue A, Tomari Y, Suzuki T, Yokogawa T, Nishikawa K, et al. Cell-free translation reconstituted with purified components. *Nat Biotechnol*. 2001 Aug;19(8):751–5.
82. Sun ZZ, Yeung E, Hayes CA, Noireaux V, Murray RM. Linear DNA for Rapid Prototyping of Synthetic Biological Circuits in an *Escherichia coli* Based TX-TL Cell-Free System. *ACS Synth Biol*. 2014 Jun 20;3(6):387–97.
83. Karzbrun E, Shin J, Bar-Ziv RH, Noireaux V. Coarse-Grained Dynamics of Protein Synthesis in a Cell-Free System. *Phys Rev Lett*. 2011 Jan;106(4):048104.
84. Niederholtmeyer H, Stepanova V, Maerkl SJ. Implementation of cell-free biological networks at steady state. *Proc Natl Acad Sci U S A*. 2013 Oct 1;110(40):15985–90.
85. Karzbrun E, Tayar AM, Noireaux V, Bar-Ziv RH. Programmable on-chip DNA compartments as artificial cells. *Science*. 2014 Aug 14;345(6198):829–32.
86. Smith MT, Wilding KM, Hunt JM, Bennett AM, Bundy BC. The emerging age of cell-free synthetic biology. *FEBS Letters*. Federation of European Biochemical Societies; 2014 Aug 25;588(17):2755–61.
87. Gibson DG, Young L, Chuang R-Y, Venter JC, Hutchison CA, Smith HO. Enzymatic assembly of DNA molecules up to several hundred kilobases. *Nat Meth*. 2009 Apr 12;6(5):343–5.
88. Cobb RE, Si T, Zhao H. Directed evolution: an evolving and enabling synthetic biology tool. *Current Opinion in Chemical Biology*. Elsevier Ltd; 2012 Aug 1;16(3-4):285–91.
89. Zhou H, Yong J, Gao H, Li T, Xiao H, Wu Y. Mannanase Man23 mutant library construction based on a novel cell-free protein expression system. *J Sci Food Agric*. 2016 Oct 13;45:1203.
90. Guillen Schlippe YV, Hartman MCT, Josephson K, Szostak JW. In Vitro Selection of Highly Modified Cyclic Peptides That Act as Tight Binding Inhibitors. *J Am Chem Soc*. 2012 Jun 27;134(25):10469–77.
91. Villarreal F, Tan C. Cell-free systems in the new age of synthetic biology. *Front Chem Sci Eng*. 2017 Jan 13.
92. Karim AS, Jewett MC. Metabolic Engineering. *Metabolic Engineering*. Elsevier; 2016 Jul 1;36(c):116–26.
93. Pardee K, Green AA, Ferrante T, Cameron DE, DaleyKeyser A, Yin P, et al. Paper-Based Synthetic Gene Networks. *CELL*. Elsevier Inc; 2014 Oct 21;:1–15.
94. Pardee K, Green AA, Takahashi MK, Braff D, Lambert G, Lee JW, et al. Rapid, Low-Cost Detection of Zika Virus Using Programmable Biomolecular Components. *CELL*. Elsevier Inc; 2016 May 19;165(5):1255–66.



95. Gruner P, Riechers B, Semin BIT, Lim J, Johnston A, Short K, et al. Controlling molecular transport in minimal emulsions. *Nature Communications*. Nature Publishing Group; 2016 Jan;7:1–9.
96. Edd JF, Di Carlo D, Humphry KJ, Köster S, Irimia D, Weitz DA, et al. Controlled encapsulation of single-cells into monodisperse picolitre drops. *Lab Chip*. 2008;8(8):1262.
97. Rakszewska A, Tel J, Chokkalingam V, Huck WT. One drop at a time: toward droplet microfluidics as a versatile tool for single-cell analysis. *Nature Publishing Group*; 2014 Sep 16;6(10):e133–11.
98. Miller OJ, Bernath K, Agresti JJ, Amitai G, Kelly BT, Mastrobattista E, et al. Directed evolution by in vitro compartmentalization. *Nat Meth*. 2006 Jul;3(7):561–70.
99. Ellefson JW, Meyer AJ, Hughes RA, Cannon JR, Brodbelt JS, Ellington AD. nbt.2714. *Nature Biotechnology*. Nature Publishing Group; 2013 Nov 3;32(1):97–101.
100. Lu W-C, Ellington AD. In vitro selection of proteins via emulsion compartments. *Methods*. 2013 Mar;60(1):75–80.
101. Lee M, Collins JW, Aubrecht DM, Sperling RA, Solomon L, Ha J-W, et al. Synchronized reinjection and coalescence of droplets in microfluidics. *Lab Chip*. 2014;14(3):509–13.
102. Chabert M, Dorfman KD, Viovy J-L. Droplet fusion by alternating current (AC) field electrocoalescence in microchannels. *Electrophoresis*. 2005 Oct;26(19):3706–15.
103. Abate AR, Hung T, Mary P. High-throughput injection with microfluidics using picoinjectors. 2010.
104. Link DR, Anna SL, Weitz DA, Stone HA. Geometrically Mediated Breakup of Drops in Microfluidic Devices. *Phys Rev Lett*. 2004 Feb 6;92(5):054503.
105. Chabert M, Viovy J-L. Microfluidic high-throughput encapsulation and hydrodynamic self-sorting of single cells. *Proc Natl Acad Sci U S A*. 2008 Mar 3;105(9):3191–6.
106. Link DR, Grasland-Mongrain E, Duri A, Sarrazin F, Cheng Z, Cristobal G, et al. Electric control of droplets in microfluidic devices. *Angew Chem Int Ed*. 2006 Apr 9;45(16):2556–60.
107. Chokkalingam V, Ma Y, Thiele J, Schalk W, Tel J, Huck WTS. An electro-coalescence chip for effective emulsion breaking in droplet microfluidics. *Lab Chip*. 2014;14(14):2398.
108. Christopher GF, Anna SL. TOPICAL REVIEW: Microfluidic methods for generating continuous droplet streams. *J Phys D: Appl Phys*. 2007 Oct;40(1):R319–36.
109. Lagus TP, Edd JF. A review of the theory, methods and recent applications of high-throughput single-cell droplet microfluidics. *J Phys D: Appl Phys*. 2013 Mar;46(1):114005.
110. Holtze C, Rowat AC, Agresti JJ, Hutchison JB, Angile FE, Schmitz CHJ, et al. Biocompatible surfactants for water-in-fluorocarbon emulsions. *Lab Chip*. 2008;8(10):1632.
111. Lee JN, Park C, Whitesides GM. Solvent Compatibility of Poly(dimethylsiloxane)-Based Microfluidic Devices. *Anal Chem*. 2003 Dec;75(23):6544–54.
112. Hildebrand JH, Cochran DRF. Liquid-Liquid Solubility of Perfluoromethylcyclohexane with Benzene, Carbon Tetrachloride, Chlorobenzene, Chloroform and Toluene. *J Am Chem Soc*. 1949 Jan;71(1):22–5.
113. Leman M, Abouakil F, Griffiths AD, Tabelaing P. Lab on a Chip. *Lab Chip*. Royal Society of Chemistry; 2015 Jan 17;15:753–65.
114. Thorsen T, Roberts RW, Arnold FH, Quake SR. Dynamic Pattern Formation in a Vesicle-Generating Microfluidic Device. *Phys Rev Lett*. American Physical Society; 2001 Apr;86:4163–6.
115. Shang L, Cheng Y, Zhao Y. Emerging Droplet Microfluidics. *Chem Rev*. 2017 Jun 12;117(12):7964–8040.
116. Turing AM. The Chemical Basis of Morphogenesis. *Philosophical Transactions of the Royal Society of London Series B*. 1952 Aug;237(6):37–72.
117. Murray JD. How the Leopard Gets its Spots. *Scientific American*. 1988 Mar;258:80–7.

## References

118. Chaplain MAJ. Reaction-diffusion pre-patterning and its potential role in tumour invasion. *Journal of Biological Systems*. World Scientific Publishing Co. Pte Ltd; 1995;3(4):929–36.
119. Lacalli TC. Modeling the *Drosophila* pair-rule pattern by reaction-diffusion: gap input and pattern control in a 4-morphogen system. *J Theor Biol*. 1990 May;144(2):171–94.
120. Allena R, Munoz JJ, Aubry D. Diffusion-reaction model for *Drosophila* embryo development. *Comput Methods Biomech Biomed Engin*. 2013;16(3):235–48.
121. Tabor JJ, Salis HM, Simpson ZB, Chevalier AA, Levskaya A, Marcotte EM, et al. A Synthetic Genetic Edge Detection Program. *CELL*. 2009;137(7):1272–81.
122. Xie Z, Wroblewska L, Prochazka L, Weiss R, Benenson Y. Multi-Input RNAi-Based Logic Circuit for Identification of Specific Cancer Cells. *Science*. 2011 Sep 1;333(6047):1307–11.
123. Tanouchi Y, Pai A, Buchler NE, You L. Programming stress-induced altruistic death in engineered bacteria. *Mol Syst Biol*. Nature Publishing Group; 2012 Nov 20;8:1–11.
124. Locke JCW, Elowitz MB. Using movies to analyse gene circuit dynamics in single cells. *Nature Publishing Group*. 2009 May;7(5):383–92.
125. Muzzey D, van Oudenaarden A. Quantitative Time-Lapse Fluorescence Microscopy in Single Cells. *Annu Rev Cell Dev Biol*. 2009 Nov;25(1):301–27.
126. Elowitz MB, Levine AJ, Siggia ED, Swain PS. Stochastic gene expression in a single cell. *Science*. 2002.
127. Newman CMH, Bettinger T. Gene therapy progress and prospects: ultrasound for gene transfer. *Gene Ther*. 2007 Feb 28;14(6):465–75.
128. Stewart EJ, Madden R, Paul G, Taddei F. Aging and death in an organism that reproduces by morphologically symmetric division. *PLoS Biol*. 2005 Jan 31;3(2):e45–5.
129. Talia SD, Skotheim JM, Bean JM, Siggia ED, Cross FR. The effects of molecular noise and size control on variability in the budding yeast cell cycle. *Nature*. 2007 Aug 23;448(7156):947–51.
130. Shapiro HM. *Practical Flow Cytometry*, Fourth Edition. John Wiley & Sons, Inc. 2003;:73–100.
131. Bjornson ZB, Nolan GP, Fantl WJ. Single-cell mass cytometry for analysis of immune system functional states. *Curr Opin Immunol*. 2013 Jul 31;25(4):484–94.
132. Melin J, Quake SR. Microfluidic large-scale integration: the evolution of design rules for biological automation. *Annu Rev Biophys Biomol Struct*. 2006 Dec 31;36:213–31.
133. Wang P, Robert L, Pelletier J, Dang WL, Taddei F, Wright A, et al. Robust Growth of *Escherichia coli*. *Current Biology*. 2010 Jun;20(12):1099–103.
134. Jiang X, Hu J, Petersen ER, Fitzgerald LA, Jackan CS, Lieber AM, et al. Probing single-to multi-cell level charge transport in *Geobacter sulfurreducens* DL-1. *Nature Communications*. 2013;4:2751.
135. Duncombe TA, Tentori AM, Herr AE. Microfluidics: reframing biological enquiry. *Nat Rev Mol Cell Biol*. Nature Publishing Group; 2015 Sep 1;16(9):554–67.
136. Sackmann EK, Fulton AL, Beebe DJ. The present and future role of microfluidics in biomedical research. *Nature*. Nature Publishing Group; 2014 Mar 5;507(7491):181–9.
137. Whitesides GM, Ostuni E, Takayama S, Jiang X, Ingber DE. Soft Lithography in Biology and Biochemistry. *Annu Rev Biomed Eng*. 2001 Aug;3(1):335–73.
138. McDonald JC, Duffy DC, Anderson JR, Chiu DT, Wu H, Schueller OJ, et al. Fabrication of microfluidic systems in poly(dimethylsiloxane). *Electrophoresis*. 2000 Jan;21(1):27–40.
139. Bennett MR, Hasty J. Microfluidic devices for measuring gene network dynamics in single cells. *Nat Rev Genet*. Nature Publishing Group; 2009;10(9):628–38.
140. Leung K, Zahn H, Leaver T, Konwar KM, Hanson NW, Pagé AP, et al. A programmable droplet-based microfluidic device applied to multiparameter analysis of single microbes and microbial communities. *Proc Natl Acad Sci U S A*. 2012 May 14;109(20):7665–70.
141. Amin R, Knowlton S, Hart A, Yenilmez B, Ghaderinezhad F, Katebifar S, et al. 3D-printed microfluidic devices. *Biofabrication*. 2016 Jun 1;8(2):022001.

142. Waheed S, Cabot JM, Macdonald NP, Lewis T, Guijt RM, Paull B, et al. Lab on a Chip. Lab Chip. Royal Society of Chemistry; 2016 May 19;16:1993–2013.
143. Ai H-W, Shaner NC, Cheng Z, Tsien RY, Campbell RE. Exploration of new chromophore structures leads to the identification of improved blue fluorescent proteins. *Biochemistry*. 2007 May 21;46(20):5904–10.
144. Shaner NC, Campbell RE, Steinbach PA, Ben N G Giepmans, Palmer AE, Tsien RY. Improved monomeric red, orange and yellow fluorescent proteins derived from *Discosoma* sp. red fluorescent protein. *Nat Biotechnol*. 2004 Nov 30;22(12):1567–72.
145. Holt LJ, Krutchinsky AN, Morgan DO. Positive feedback sharpens the anaphase switch. *Nature*. 2008 Jun 15;454(7202):353–7.
146. Skotheim JM, Di Talia S, Siggia ED, Cross FR. Positive feedback of G1 cyclins ensures coherent cell cycle entry. *Nature*. 2008 Jul 17;454(7202):291–6.
147. Dultz E, Zanin E, Wurzenberger C, Braun M, Rabut G, Sironi L, et al. Systematic kinetic analysis of mitotic dis- and reassembly of the nuclear pore in living cells. *J Cell Biol*. Rockefeller University Press; 2008 Mar 10;180(5):857–65.
148. Rosenfeld N, Young JW, Alon U, Swain PS, Elowitz MB. Gene regulation at the single-cell level. *Science*. 2005;307(5717):1962–5.
149. Kalisky T, Dekel E, Alon U. Cost–benefit theory and optimal design of gene regulation functions. *Phys Biol*. 2007 Dec 1;4(4):229–45.
150. Grilly C, Stricker J, Pang WL, Bennett MR, Hasty J. A synthetic gene network for tuning protein degradation in *Saccharomyces cerevisiae*. *Mol Syst Biol*. 2007;3:127.
151. Patterson GH. A Photoactivatable GFP for Selective Photolabeling of Proteins and Cells. *Science*. 2002 Sep 13;297(5588):1873–7.
152. Subach FV, Subach OM, Gundorov IS, Morozova KS, Piatkevich KD, Cuervo AM, et al. Monomeric fluorescent timers that change color from blue to red report on cellular trafficking. *Nat Chem Biol*. 2009 Jan 31;5(2):118–26.
153. Andersen JB, Sternberg C, Poulsen LK, Bjorn SP, Givskov M, Molin S. New unstable variants of green fluorescent protein for studies of transient gene expression in bacteria. *Appl Environ Microbiol*. 1998 Jun;64(6):2240–6.
154. Keiler KC, Waller PR, Sauer RT. Role of a peptide tagging system in degradation of proteins synthesized from damaged messenger RNA. *Science*. 1996;271:990.
155. Paige JS, Wu KY, Jaffrey SR. RNA Mimics of Green Fluorescent Protein. *Science*. 2011 Jul 29;333(6042):642–6.
156. Meijering E, Smal I, Dzyubachyk O, Olivo-Marin J-C. Time-Lapse Imaging. 2012 Dec 27;:1–32.
157. de Kievit TR, Iglewski BH. Bacterial quorum sensing in pathogenic relationships. *Infect Immun*. 2000 Aug 31;68(9):4839–49.
158. Zhu J, Miller MB, Vance RE, Dziejman M, Bassler BL, Mekalanos JJ. Quorum-sensing regulators control virulence gene expression in *Vibrio cholerae*. *Proc Natl Acad Sci U S A*. 2002 Mar 5;99(5):3129–34.
159. Rutherford ST, Bassler BL. Bacterial Quorum Sensing: Its Role in Virulence and Possibilities for Its Control. *Cold Spring Harbor Perspectives in Medicine*. 2012 Nov 1;2(11):a012427–7.
160. Skindersoe ME, Alhede M, Phipps R, Yang L, Jensen PO, Rasmussen TB, et al. Effects of Antibiotics on Quorum Sensing in *Pseudomonas aeruginosa*. *Antimicrobial Agents and Chemotherapy*. 2008 Sep 24;52(10):3648–63.
161. Hammer BK, Bassler BL. Quorum sensing controls biofilm formation in *Vibrio cholerae*. *Molecular Microbiology*. 2003 Aug 20;50(1):101–4.
162. Nealson KH. Autoinduction of bacterial luciferase. Occurrence, mechanism and significance. *Arch Microbiol*. 1977 Feb 4;112(1):73–9.
163. Miller MB, Bassler BL. Quorum sensing in bacteria. *Annu Rev Microbiol*. 2001 Jan 1;55:165–99.
164. Swift S, Throup JP, Williams P, Salmond G. Quorum sensing: a population-density component in the determination of bacterial phenotype. *Trends in biochemical ....* 1996.

## References

165. Rosenberg E, Keller KH, Dworkin M. Cell density-dependent growth of *Myxococcus xanthus* on casein. *Journal of Bacteriology*. 1977.
166. Minogue TD, Carlier AL, Koutsoudis MD, Bodman von SB. The cell density-dependent expression of stewartan exopolysaccharide in *Pantoea stewartii* ssp. *stewartii* is a function of EsaR-mediated repression of the *rcaA* gene. *Mol Microbiol*. 2005 Mar 31;56(1):189–203.
167. Hilton T, Rosche T, Froelich B, Smith B, Oliver J. Capsular Polysaccharide Phase Variation in *Vibrio vulnificus*. *Appl Environ Microbiol*. 2006 Nov 6;72(11):6986–93.
168. Barnard AML, Bowden SD, Burr T, Coulthurst SJ, Monson RE, Salmond GPC. Quorum sensing, virulence and secondary metabolite production in plant soft-rotting bacteria. *Philosophical Transactions of the Royal Society B: Biological Sciences*. 2007 Jul 29;362(1483):1165–83.
169. Daniels R, Vanderleyden J, Michiels J. Quorum sensing and swarming migration in bacteria. *FEMS Microbiol Rev*. 2004 Jun 1;28(3):261–89.
170. Atkinson S, Chang CY, Sockett RE, Camara M, Williams P. Quorum Sensing in *Yersinia enterocolitica* Controls Swimming and Swarming Motility. *Journal of Bacteriology*. 2006 Feb 1;188(4):1451–61.
171. Gantner S, Schmid M, DÄ¼rr C, Schuegger R, Steidle A, Hutzler P, et al. In situ quantitation of the spatial scale of calling distances and population density-independent N-acylhomoserine lactone-mediated communication by rhizobacteria colonized on plant roots. *FEMS Microbiology Ecology*. 2005 Jan 2;56(2):188–94.
172. Boedicker JQ, Vincent ME, Ismagilov RF. Microfluidic Confinement of Single Cells of Bacteria in Small Volumes Initiates High-Density Behavior of Quorum Sensing and Growth and Reveals Its Variability. *Angew Chem Int Ed*. 2009 Jul 27;48(32):5908–11.
173. Hense BA, Kuttler C, Müller J, Rothballer M, Hartmann A, Kreft J-U. Does efficiency sensing unify diffusion and quorum sensing? *Nat Rev Microbiol*. 2007 Feb 28;5(3):230–9.
174. Redfield RJ. Is quorum sensing a side effect of diffusion sensing? *Trends in Microbiology*. 2002 Aug;10(8):365–70.
175. Cornforth DM, Popat R, McNally L, Gurney J, Scott-Phillips TC, Ivens A, et al. Combinatorial quorum sensing allows bacteria to resolve their social and physical environment. *Proc Natl Acad Sci U S A*. 2014 Mar 18;111(11):4280–4.
176. Weiss R, Knight TF Jr. Engineered communications for microbial robotics. *DNA Computing, 6th International Workshop on DNA-Based Computers, DNA6*. 2000;2054:1–16.
177. You LC, Cox RS, Weiss R, Arnold FH. Programmed population control by cell-cell communication and regulated killing. *Nature*. 2004 Apr 22;428(6985):868–71.
178. Kobayashi H, Kærn M, Araki M, Chung K, Gardner TS, Cantor CR, et al. Programmable cells: interfacing natural and engineered gene networks. *Proc Natl Acad Sci U S A*. 2004 Jun 1;101(22):8414–9.
179. Brenner K, Karig DK, Weiss R, Arnold FH. Engineered bidirectional communication mediates a consensus in a microbial biofilm consortium. *Proc Natl Acad Sci U S A*. 2007 Oct 30;104(44):17300–4.
180. Weber W, Daoud-El Baba M, Fussenegger M. Synthetic ecosystems based on airborne inter- and intrakingdom communication. *Proc Natl Acad Sci U S A*. 2007 Jun 19;104(25):10435–40.
181. Basu S, Gerchman Y, Collins CH, Arnold FH, Weiss R. A synthetic multicellular system for programmed pattern formation. *Nature*. 2005 Apr 28;434(7037):1130–4.
182. Danino T, Mondragón-Palomino O, Tsimring L, Hasty J. A synchronized quorum of genetic clocks. *Nature*. 2010 Jan 21;463(7279):326–30.
183. Prindle A, Samayoa P, Razinkov I, Danino T, Tsimring LS, Hasty J. A sensing array of radically coupled genetic “biopixels.” *Nature*. Nature Publishing Group; 2011 Dec 20;481(7379):39–44.
184. Papenfort K, Bassler BL. Quorum sensing signal–response systems in Gram-negative bacteria. *Nature Publishing Group*. Nature Publishing Group; 2016 Sep 1;14(9):576–88.

185. Miller MB, Skorupski K, Lenz DH, Taylor RK, Bassler BL. Parallel quorum sensing systems converge to regulate virulence in *Vibrio cholerae*. *CELL*. 2002 Aug 9;110(3):303–14.
186. Bassler BL, Greenberg EP, Stevens AM. Cross-species induction of luminescence in the quorum-sensing bacterium *Vibrio harveyi*. *Journal of Bacteriology*. 1997 Jun;179(12):4043–5.
187. Surette MG, Miller MB, Bassler BL. Quorum sensing in *Escherichia coli*, *Salmonella typhimurium*, and *Vibrio harveyi*: a new family of genes responsible for autoinducer production. *Proc Natl Acad Sci U S A*. 1999 Feb 16;96(4):1639–44.
188. Xavier KB, Bassler BL. Interference with AI-2-mediated bacterial cell-cell communication. *Nature*. 2005 Sep 28;437(7059):750–3.
189. Schauder S, Shokat K, Surette MG, Bassler BL. The LuxS family of bacterial autoinducers: biosynthesis of a novel quorum-sensing signal molecule. *Mol Microbiol*. 2001 Jul;41(2):463–76.
190. Chen X, Schauder S, Potier N, Van Dorsselaer A. Structural identification of a bacterial quorum-sensing signal containing boron. *Nature*. 2002.
191. Miller ST, Xavier KB, Campagna SR, Taga ME, Semmelhack MF, Bassler BL, et al. *Salmonella typhimurium* recognizes a chemically distinct form of the bacterial quorum-sensing signal AI-2. *Molecular Cell*. 2004 Sep 10;15(5):677–87.
192. Pereira CS, Thompson JA, Xavier KB. AI-2-mediated signalling in bacteria. *FEMS Microbiol Rev*. 2013 Mar 1;37(2):156–81.
193. Duan K, Dammel C, Stein J, Rabin H, Surette MG. Modulation of *Pseudomonas aeruginosa* gene expression by host microflora through interspecies communication. *Molecular Microbiology*. 2003 Nov 17;50(5):1477–91.
194. Dunny GM, Leonard BA. Cell-cell communication in gram-positive bacteria. *Annu Rev Microbiol*. 1997;51:527–64.
195. Lyon GJ, Novick RP. Peptide signaling in *Staphylococcus aureus* and other Gram-positive bacteria. *Peptides*. 2004 Sep;25(9):1389–403.
196. Pottathil M, Lazazzera BA. The extracellular Phr peptide-Rap phosphatase signaling circuit of *Bacillus subtilis*. *Front Biosci*. 2003 Jan;8:d32–45.
197. Antiporta MH, Dunny GM. ccfA, the Genetic Determinant for the cCF10 Peptide Pheromone in *Enterococcus faecalis* OG1RF. *Journal of Bacteriology*. 2002 Feb 15;184(4):1155–62.
198. Fuqua C, Greenberg EP. Self perception in bacteria: quorum sensing with acylated homoserine lactones. *Current Opinion in Microbiology*. 1998 Apr;1(2):183–9.
199. Whitehead NA, Barnard AM, Slater H, Simpson NJ, Salmond GP. Quorum-sensing in Gram-negative bacteria. *FEMS Microbiol Rev*. 2001 Aug;25(4):365–404.
200. Engebrecht J, Silverman M. Identification of genes and gene products necessary for bacterial bioluminescence. 1984. pp. 4154–8.
201. Hanzelka BL, Greenberg EP. Quorum sensing in *Vibrio fischeri*: evidence that S-adenosylmethionine is the amino acid substrate for autoinducer synthesis. *Journal of Bacteriology*. 1996 Sep;178(17):5291–4.
202. Val DL, Cronan JE. In vivo evidence that S-adenosylmethionine and fatty acid synthesis intermediates are the substrates for the LuxI family of autoinducer synthases. *Journal of Bacteriology*. 1998 Apr 30;180(10):2644–51.
203. Fuqua C, Greenberg EP. Signalling: Listening in on bacteria: acyl-homoserine lactone signalling. *Nat Rev Mol Cell Biol*. 2002 Sep;3(9):685–95.
204. More MI, Finger LD, Stryker JL, Fuqua C, Eberhard A, Winans SC. Enzymatic synthesis of a quorum-sensing autoinducer through use of defined substrates. *Science*. 1996 Jun;272(5268):1655–8.
205. Watson WT, Minogue TD, Val DL, Bodman von SB, Churchill MEA. Structural Basis and Specificity of Acyl-Homoserine Lactone Signal Production in Bacterial Quorum Sensing. *Molecular Cell*. Cell Press; 2002 Mar 22;9(3):685–94.
206. Parsek MR, Val DL, Hanzelka BL, Cronan JE, Greenberg EP. Acyl homoserine-lactone quorum-sensing signal generation. *Proc Natl Acad Sci U S A*. 1999 Apr 13;96(8):4360–5.



## References

207. Kaplan HB, Greenberg EP. Diffusion of autoinducer is involved in regulation of the *Vibrio fischeri* luminescence system. *Journal of Bacteriology*. 1985 Sep 1;163(3):1210–4.
208. Evans K, Passador L, Srikumar R, Tsang E, Nezezon J, Poole K. Influence of the MexAB-OprM multidrug efflux system on quorum sensing in *Pseudomonas aeruginosa*. *Journal of Bacteriology*. 1998 Oct;180(20):5443–7.
209. Pearson JP, Van Delden C, Iglewski BH. Active efflux and diffusion are involved in transport of *Pseudomonas aeruginosa* cell-to-cell signals. *Journal of Bacteriology*. 1999 Feb;181(4):1203–10.
210. Smith D, Wang J-H, Swatton JE, Davenport P, Price B, Mikkelsen H, et al. Variations on a theme: diverse N-acyl homoserine lactone-mediated quorum sensing mechanisms in gram-negative bacteria. *Sci Prog*. 2006;89(Pt 3-4):167–211.
211. Li Z, Nair SK. Quorum sensing: How bacteria can coordinate activity and synchronize their response to external signals? *Protein Science*. 2012 Aug 21;21(10):1403–17.
212. Stevens AM, Dolan KM, Greenberg EP. Synergistic binding of the *Vibrio fischeri* LuxR transcriptional activator domain and RNA polymerase to the lux promoter region. 1994. pp. 12619–23.
213. Schauder S, Bassler BL. The languages of bacteria. *Genes Dev*. 2001 Jun 15;15(12):1468–80.
214. Pierson LS, Keppenne VD, Wood DW. Phenazine antibiotic biosynthesis in *Pseudomonas aureofaciens* 30-84 is regulated by PhzR in response to cell density. *Journal of Bacteriology*. 1994 Jul;176(13):3966–74.
215. Leadbetter JR, Greenberg EP. Metabolism of acyl-homoserine lactone quorum-sensing signals by *Variovorax paradoxus*. *Journal of Bacteriology*. 2000 Dec;182(24):6921–6.
216. Dong YH, Wang LH, Xu JL, Zhang HB, Zhang XF, Zhang LH. Quenching quorum-sensing-dependent bacterial infection by an N-acyl homoserine lactonase. *Nature*. 2001 Jun 13;411(6839):813–7.
217. Dong YH, Wang LH, Xu JL, Zhang HB, Zhang XF, Zhang LH. Quenching quorum-sensing-dependent bacterial infection by an N-acyl homoserine lactonase. *Nature*. 2001;411:813–7.
218. Givskov M, de Nys R, Manefield M, Gram L, Maximilien R, Eberl L, et al. Eukaryotic interference with homoserine lactone-mediated prokaryotic signalling. *Journal of Bacteriology*. 1996 Nov;178(22):6618–22.
219. Manefield M, Rasmussen TB, Henzter M, Andersen JB, Steinberg P, Kjelleberg S, et al. Halogenated furanones inhibit quorum sensing through accelerated LuxR turnover. *Microbiology*. 2002;148(Pt 4):1119–27.
220. O'Loughlin CT, Miller LC, Siryaporn A, Drescher K, Semmelhack MF, Bassler BL. A quorum-sensing inhibitor blocks *Pseudomonas aeruginosa* virulence and biofilm formation. *Proc Natl Acad Sci U S A*. 2013 Oct 28;110(44):17981–6.
221. Welsh MA, Eibergen NR, Moore JD, Blackwell HE. Small Molecule Disruption of Quorum Sensing Cross-Regulation in *Pseudomonas aeruginosa* Causes Major and Unexpected Alterations to Virulence Phenotypes. *J Am Chem Soc*. 2015 Feb 4;137(4):1510–9.
222. Urbanowski ML, Lostroh CP, Greenberg EP. Reversible acyl-homoserine lactone binding to purified *Vibrio fischeri* LuxR protein. *J Bacteriol*. 2004;186(3):631–7.
223. Haseltine EL, Arnold FH. Implications of Rewiring Bacterial Quorum Sensing. *Appl Environ Microbiol*. 2008 Jan 9;74(2):437–45.
224. Koch AL. The logarithm in biology. 1. Mechanisms generating the log-normal distribution exactly. *J Theor Biol*. 1966 Nov;12(2):276–90.
225. Koch AL. The logarithm in biology. II. Distributions simulating the log-normal. *J Theor Biol*. 1969 May;23(2):251–68.
226. Berg OG. A model for the statistical fluctuations of protein numbers in a microbial population. *J Theor Biol*. 1978 Apr 19;71(4):587–603.
227. Shahrezaei V, Swain PS. Analytical distributions for stochastic gene expression. Vol. q-bio.MN, arXiv.org. 2008. pp. 17256–61.

228. Ozbudak EM, Thattai M, Kurtser I, Grossman AD, van Oudenaarden A. Regulation of noise in the expression of a single gene. *Nat Genet.* 2002 Apr 22;31(1):69–73.
229. Batada NN, Hurst LD. Evolution of chromosome organization driven by selection for reduced gene expression noise. *Nat Genet.* 2007 Aug;39(8):945–9.
230. Becskei A, Serrano L. Engineering stability in gene networks by autoregulation. *Nature.* 2000 Jun 1;405(6786):590–3.
231. Hense BA, Müller J, Kuttler C, Hartmann A. Spatial Heterogeneity of Autoinducer Regulation Systems. *Sensors.* 2012 Mar 28;12(12):4156–71.
232. Langebrake JB, Dilanji GE, Hagen SJ, De Leenheer P. Traveling waves in response to a diffusing quorum sensing signal in spatially-extended bacterial colonies. *Journal of Theoretical Biology.* 2014 Dec;363:53–61.
233. Mazutis L, Griffiths AD. Selective droplet coalescence using microfluidic systems. *Lab Chip.* 2012;12(10):1800.
234. Vazquez M-V, Berezhkovskii AM, Dagdug L. Diffusion in linear porous media with periodic entropy barriers: A tube formed by contacting spheres. *The Journal of Chemical Physics.* 2008 Jul 28;129(4):046101.
235. Poulin P, Bibette J. Adhesion of Water Droplets in Organic Solvent. *Langmuir.* 1998 Oct;14(22):6341–3.
236. Thiam AR, Bremond N, Bibette J. From Stability to Permeability of Adhesive Emulsion Bilayers. *Langmuir.* 2012 Apr 17;28(15):6291–8.
237. Skhiri Y, Gruner P, Semin B, Brosseau Q, Pekin D, Mazutis L, et al. Dynamics of molecular transport by surfactants in emulsions. *Soft Matter.* 2012;8(41):10618.
238. Verkman AS. Solute and macromolecule diffusion in cellular aqueous compartments. *Trends in Biochemical Sciences.* 2002 Jan;27(1):27–33.
239. Kendon V, Sebald A, Stepney S. Heterotic computing: exploiting hybrid computational devices. *Phil Trans R Soc A.* 2015 Jun 15;373(2046):20150091.

## 5 Appendix

The following appendices comprise a copy of the originally supplemental information material of the publications described under section results.

## 5.1. Single cell analysis of a bacterial sender-receiver system

S1

*Ramalho et al., Single cell analysis of a bacterial sender-receiver system*

### S1 File

#### - Supplementary Texts:

- A Image processing
- B Gene expression noise
- C Sender - receiver system

#### - Supplementary Figures A - F

### A Image processing

#### Background

We developed a custom software application to automate the single cell analysis of brightfield images. Our goal was to strike a balance between accuracy, performance and ease of use. To do so, we evaluated several existing applications (CellProfiler [1], CellTracer [2], <http://cellcognition.org/etc>) and implemented the most useful features. Source code and binaries freely available here. We prioritized simplicity over flexibility by using a fixed image processing pipeline. We expect labs with similar workflows will be able to use our application with a minimal learning curve. In the following sections, a brief outline of the image analysis algorithm is given along with a rationale for the choice of the used methods.

#### Image preprocessing

The first step is image preprocessing. The user may define a subsection of the image stack to analyze which is then enhanced by applying well known filters: contrast enhancement, noise reduction, sharpening and resolution increase. Contrast is enhanced by calculating the brightness histogram; discarding all brightness values beneath a user-defined threshold and rescaling the brightness values such that the histogram now spans the full brightness range. Noise reduction is accomplished by the nonlocal means filter implemented in the OpenCV library [3]. The image is sharpened by subtracting the lowpass filtered image. Finally, the accuracy of many subsequent pipeline steps is increased if we work with a higher resolution image. Thus, the user has the option to double or quadruple the image resolution at this step.

#### Background detection

We found that optimal performance was achieved by combining the output of several simple thresholding methods. First, a global brightness threshold may be set by the user. Second, a local brightness threshold is used, where a pixel is marked as background if its brightness is above the local brightness average by a pre specified amount. The local average is computed around a window of pre-specified size which should match the typical length scale of the smallest axis of a cell. Finally, large areas with no cells which might elude the previous two methods are detached by employing a method similar to Wang et al [2], where prominent edges are detected and enlarged to outline the probable location of the cells; the complement of that area is marked as background.

### Cell detection

Given specified maximum bounds on width and height, cell markers are created by a multi-step procedure. Initially all connected regions of non-background pixels are assigned to a unique marker. Each region too big to be a single cell is then further segmented based on the brightness profile and cell geometry. This process uses a likelihood function, which assigns a likelihood for each of pixel to be part of the inside of a cell, taking into account the brightness, the brightness gradient, and the cell geometry (by using the distance transform). New markers are then assigned to connected regions of pixels above a certain likelihood threshold. This threshold is chosen to be the minimum value such that the regions of all markers obey the specified bound. The resulting regions are then expanded and refined using the watershed algorithm.

### Cell classification

Often, objects which are not cells are present in the microscopy image but are still detected as such due to similar brightness profiles as real cells. To overcome this problem, an optional final step of the operation pipeline entails the training of a support vector machine (SVM) to distinguish interesting cells from such outliers. This method has previously been used to distinguish cell phenotypes with success [4].

The process begins by taking each connected area of segmented pixels and calculating features summarizing its geometry and brightness, which will become a high dimensional data point  $d_i$  for the training set. Each point is selected by the user, who also marks each label as correct or incorrect directly on the user interface thereby associating each datapoint with a class  $C \in \{0, 1\}$ . The SVM algorithm then applies a nonlinear transformation to the feature space such that a hyperplane separating the two classes of points can be found. The implementation found in libSVM [5] has been used here. Empirically we determined that a dataset with around 50 points provides good classification performance. By visual inspection the user may validate the results and edit the training data to avoid over or under fitting.

### Lineage tracking

In order to track cells in time, a frame by frame tracking procedure was adopted. In each frame we determine a cell's parent by calculating the overlap between its assigned pixels and the pixels of detected cells in the previous frame. The cell label from the previous frame which maximizes this overlap is then set as the parent. If  $l_i^t$  is a boolean vector where pixels are marked as 1 if they belong to the  $i$ th label at frame  $t$  and 0 otherwise; the parent label for that label is defined as

$$p_{i,t} = \arg \max_{j \in \text{labels}(t-1)} \sum_{\text{pixels}} l_j^{t-1} l_i^t.$$

This method was compared to the minimization of the distance between the center of mass of a cell and those of its ancestors. If  $c_i^t$  is a 2d vector containing the center of mass of the  $i$ th label at frame  $t$ , then

$$p_{i,t} = \arg \min_{j \in \text{labels}(t-1)} c_j^{t-1} \cdot c_i^t.$$

Empirically the maximum overlap method performed better than the center of mass distance for all datasets we tried. As before, the user can inspect the generated trajectories and manually correct the lineage in case of error via a graphical user interface. This allowed us to automatically extract lineage data and single cell fluorescence trajectories as a function of time.



### Single cell trajectories

Fluorescence is extracted by summing measured intensity at each pixel for each channel. In this case we define

$$p^k = \sum_{i,j \in \mathcal{L}(k)} f_{i,j}$$

with  $f_{i,j}$  the intensity of a given pixel in the  $k$ th detected label, denoted by  $\mathcal{L}(k)$ . The area  $A$  of a cell can also be calculated by summing over all pixels in a label.

Once we have obtained the time trajectories of  $p^k(t)$  and  $A^k(t)$ , we can fit them using a smoothing spline to be able to calculate derivatives and then use  $\alpha^k(t) \sim \dot{p}^k(t)/\dot{A}^k(t)$ , as in the previous sections.

### Image analysis for sender-receiver experiments

The image analysis methodology for these experiments is largely parallel to the one for the receiver-only experiments. The cells are segmented using the image analysis program, and RFP and GFP fluorescences are extracted. A bivariate Gaussian mixture model is fit to the final frame to discover senders and receivers, and their lineage is backtracked throughout the experiment to obtain their induction trajectories. From these trajectories, GFP and RFP expression rates can be extracted.

### Comparison with other methods

Our single cell analysis yielded significantly better results than a naive analysis based on the public domain image processing program ImageJ [6]. Such an analysis was based on a thresholding procedure where all pixels of a brightfield image with brightness below a certain threshold are assigned as 'cell pixels' and that integrated area is taken as a proxy for cell mass. This procedure incurs the systematic error of adding the mass of dark objects to the cell mass, which means that the determined area values are not fully compatible with the determined fluorescence (objects which are not cells do not fluoresce). The response function obtained with this procedure appeared less accurate (Figure S3), however it was nevertheless qualitatively similar to the response shown in Fig. 1C of the main paper with the more elaborate procedure described above.

## B Gene expression noise

### Noise quantification

We analyzed the noise in our data on different levels. At the lowest level there are fluctuations in intensity level between the individual pixels corresponding to a cell. These fluctuations may be partially due to experimental error, but also inherent to inhomogeneity in gene expression in the cell. We calculate the average and standard deviation of a single cell's fluorescence as

$$\langle p^k \rangle = \sum_{i,j \in \mathcal{L}(k)} p_{i,j} / a^k \quad (1)$$

(using the notation introduced above) and

$$\sigma_{p^k}^2 = \sum_{i,j \in \mathcal{L}(k)} (p_{i,j} - \langle p^k \rangle)^2 / a^k, \quad (2)$$

where  $a^k = \sum_{i,j \in \mathcal{L}(k)} 1$ . Then there is the noise arising from heterogeneity between different individuals in a population, which can be calculated from the previous values,

$$\bar{p} = \sum_k \langle p^k \rangle / N, \quad (3)$$

$$\sigma_p^2 = \sum_k (\langle p^k \rangle - \bar{p})^2 / N. \quad (4)$$

Finally there is the temporal evolution noise. For each temporal trajectory, we can calculate a mean and standard deviation via the use of a smoothing filter. This relates the temporal noise for a single cell.

## C Sender-receiver system

The evolution equations

$$\frac{d}{dt}[\text{LuxI}](t) = \alpha_I r N(t) - \lambda [\text{LuxI}](t). \quad (5)$$

and

$$\frac{d}{dt}[\text{AHL}](t) = \alpha_a [\text{LuxI}](t) - C [\text{AHL}](t) \quad (6)$$

given in the main text can be solved analytically for exponential cell growth  $N(t) = N_0 e^{\gamma t}$ . The solution to the first equation is given by:

$$[\text{LuxI}](t) = \frac{N_0 \alpha_I r}{\gamma + \lambda} (e^{\gamma t} - e^{-\lambda t}) \quad (7)$$

Insertion into Eq.(7) can then be solved to yield:

$$[\text{AHL}](t) = \frac{N_0 \alpha_I r}{(\gamma + \lambda)(C + \gamma)(C - \lambda)} [C (e^{\gamma t} - e^{-\lambda t}) + \gamma (e^{-Ct} - e^{-\lambda t}) + \lambda (e^{-Ct} - e^{\gamma t})] \quad (8)$$

Expanding the exponentials for low values of  $C, \gamma, \lambda$  (up to terms of order  $t^2$ ) results in:

$$[\text{AHL}](t) \approx \frac{1}{2} N_0 \alpha_I \alpha_a r t^2, \quad (9)$$

as given in the main text.

## References

1. Carpenter A, Jones T, Lamprecht M, Clarke C, Kang I, Friman O, et al. CellProfiler: image analysis software for identifying and quantifying cell phenotypes. *Genome Biol.* 2006;7(10):R100.
2. Wang Q, Niemi J, Tan CM, You L, West M. Image segmentation and dynamic lineage analysis in single-cell fluorescence microscopy. *Cytom Part A.* 2010;77A(1):101–110. Available from: <http://doi.wiley.com/10.1002/cyto.a.20812>.
3. Bradski G. The OpenCV Library. *Dr Dobb's Journal of Software Tools.* 2000.
4. Rämö P, Sacher R, Snijder B, Begemann B, Pelkmans L. CellClassifier: supervised learning of cellular phenotypes. *Bioinformatics.* 2009 Nov;25(22):3028–3030.
5. Chang CC, Lin CJ. LIBSVM: A library for support vector machines. *ACM Trans Intell Syst Technol.* 2011;2:27:1–27:27.
6. Schneider CA, Rasband WS, Eliceiri KW. NIH Image to ImageJ: 25 years of image analysis. *Nat Meth.* 2012;9(7):671–675.

## Supplementary Figures

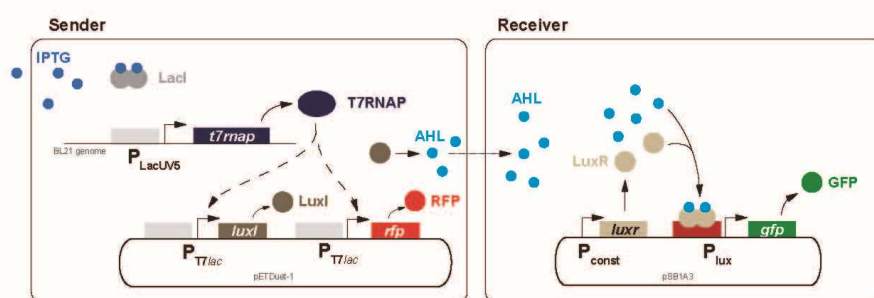


**Fig A.** Schematic overview of the bacterial sender-receiver system. *Sender cells*: As indicated, in the presence of IPTG repressor protein LacI is not bound to the lac promoters  $P_{LacUV5}$  on the bacterial genome and  $P_{T7lac}$  on the sender plasmid. T7 RNA polymerase is then expressed, which in turn leads to the expression of AHL synthase LuxI and fluorescent reporter protein RFP from the plasmid. LuxI catalyzes the production of the quorum sensing signal N-3-oxo-C6-homoserine lactone (AHL), which can freely pass through the bacterial cell wall. *Receiver cells* constitutively express activator LuxR from the receiver plasmid. In the presence of AHL, LuxR activates GFP expression, which is under the control of the lux promoter  $P_{lux}$ . In the first set of experiments in the main paper, only receiver cells are used and AHL is manually added to the culture medium to induce gene expression.

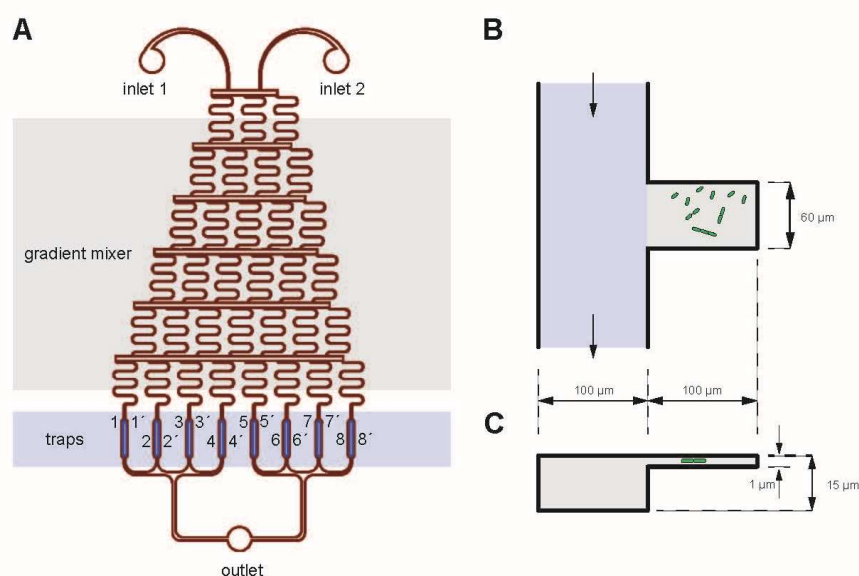


**Fig B.** Microfluidic chemostats. (A) The microfluidic chemostat consists of a gradient mixer (adopted from Ref. 55 of the main paper), which generates linear concentration gradients of chemicals supplied through inlets 1 and 2, respectively. Eight gradient exits are connected to a total of  $2 \times 8$  microfluidic channels, which contain trapping regions for bacteria (similar to Ref. 8 of the main paper). In the experiments, the concentration of AHL was varied in 1 nM steps in the range 0 – 21 nM, and in 10 nM steps in the range 20 – 90 nM. (B) Top view of a supply channel (blue) with trap region (grey). (C) Side view (not drawn to scale) showing the reduced height of the trap region, which only allows bacterial growth in a single layer.



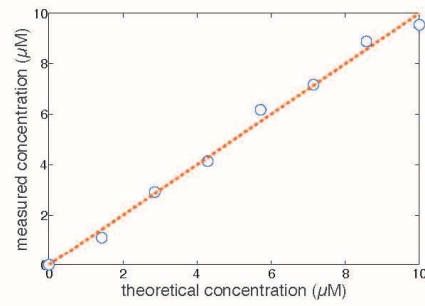


**Fig C.** Calibration of the gradient mixer system. We performed a series of calibration experiments (with flow rates 40, 80, 160 and 320  $\mu\text{l/h}$ ) to evaluate the quality of the concentration gradient generated by the microfluidic mixer shown in Fig. S2. In these experiments the right reservoir was loaded with buffer solution containing 10  $\mu\text{M}$  fluorescein and the left reservoir with pure buffer (0  $\mu\text{M}$ ). After establishment of a steady gradient, we measured the fluorescence in the trap regions. The background-subtracted fluorescence values were then plotted against the nominal concentrations expected for the traps. As shown in the figure (which is obtained for the 160  $\mu\text{l/h}$  case), indeed a linear concentration gradient is generated. A linear regression fit to these values (fixed at 0  $\mu\text{M}$ ) allows us to estimate the concentration errors. The maximum relative deviation from the nominal concentration is found to be  $\approx 20\%$  in all experiments performed.

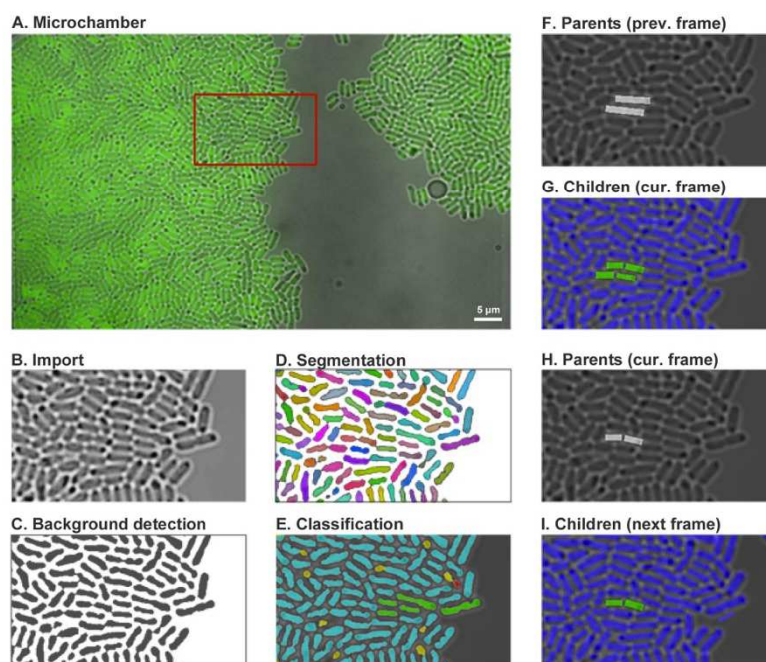


**Fig D.** Overview of the image analysis procedure. (A) A composite brightfield and fluorescence image, cropped to display only the microchamber contents. The program workflow is demonstrated by focusing on the red highlighted area of the picture, a region with dimensions  $21.6 \times 12.4 \mu\text{m}^2$ . (B) Once the brightfield image is imported, contrast is enhanced and resolution increased. (C) Background detection is performed via a hybrid method combining adaptive thresholding and geometry information. (D) Cell markers are created using gradient information and geometric priors, refined using the watershed method. (E) A statistical classifier is used to remove mis-segmented cells. (F-I) Using the maximum overlap method, cell lineages are reconstructed (see also Fig. S4). A cell division event is highlighted in (F-G); and propagated forward in (H-I). The user can correct tracking errors manually in the application.

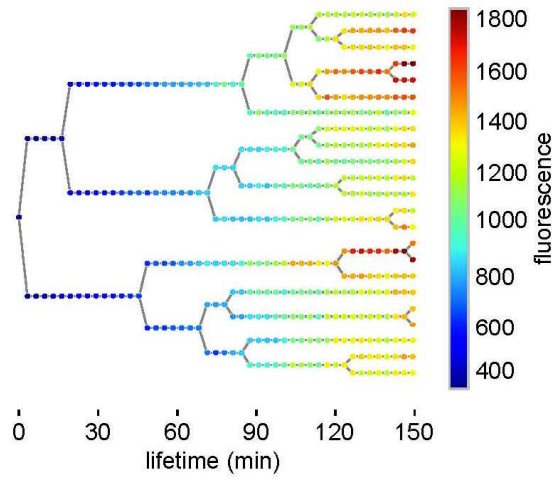


**Fig E.** Example of a cell lineage extracted using the segmentation software. The lineage is first automatically calculated by using the maximum overlap method on the segmented cells, as described in the main text. The segmentation method is conservative in detecting cell divisions, which means that already divided cells may be detected as a single cell for a few frames longer. This explains the observed cell division timings in the above lineage tree. After this step a correction heuristic is applied which finds potential mother-daughter mismatches by searching for fluorescence fluctuations twice as large as the calculated noise in a typical trajectory. For presentational clarity any branches which do not reach the final frame (due to mismatches) were manually edited out of the above plot.

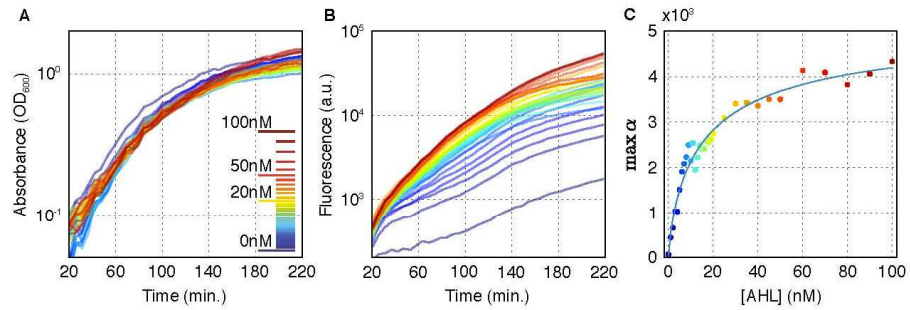


**Fig F.** Bulk analysis of gene induction by AHL using plate reader measurements. (A) Background subtracted absorbance of growing bacterial cultures for AHL concentrations ranging from 0 nM to 100 nM. (B) Corresponding background subtracted fluorescence intensities for the different AHL concentrations. (C) Maximum gene expression rate  $\alpha_{max}$  obtained for the different AHL concentrations as explained in the main text. The solid line is a fit with a Hill curve with Hill exponent  $n = 0.97 \pm 0.08$  and induction threshold  $K = 13.9 \pm 1.7$  nM.

## 5.2. Communication and computation by bacteria compartmentalized within microemulsion droplets

### Supporting Information

#### Communication and computation by bacteria compartmentalized within microemulsion droplets

---

Maximilian Weitz<sup>‡</sup>, Andrea Mückl<sup>‡</sup>, Korbinian Kapsner, Ronja Berg, Andrea Meyer, and Friedrich C. Simmel<sup>\*</sup>

Physics Department and ZNN/WSI, Technische Universität München, Garching, Germany

<sup>\*</sup>Corresponding author contact: email: [simmel@tum.de](mailto:simmel@tum.de), phone: +49 89 289 11610, fax: +49 89 289 11612, home page: <http://www.e14.ph.tum.de/>

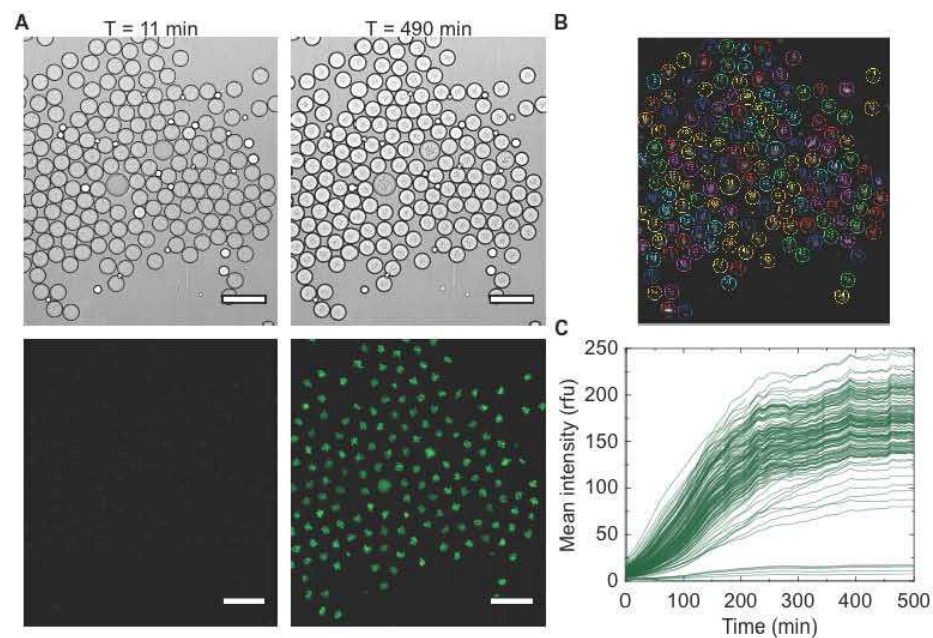
#### Table of contents

|  |           |
|--|-----------|
| <b>1 SUPPLEMENTARY FIGURES</b>                 | <b>2</b>  |
| <b>2 SUPPLEMENTARY TABLES</b>                  | <b>13</b> |
| <b>3 SUPPLEMENTARY MATERIALS</b>               | <b>14</b> |
| Bacterial strains and culture media.....       | 14        |
| <b>4 SUPPLEMENTARY METHODS</b>                 | <b>14</b> |
| 4.1 Cell growth.....                           | 14        |
| 4.2 Plasmid construction.....                  | 15        |
| 4.3 Generation of emulsions .....              | 15        |
| 4.4 Communication modes.....                   | 16        |
| 4.5 Characterization of genetic circuits ..... | 17        |
| 4.6 Time-lapse microscopy .....                | 19        |
| 4.7 Modeling.....                              | 19        |

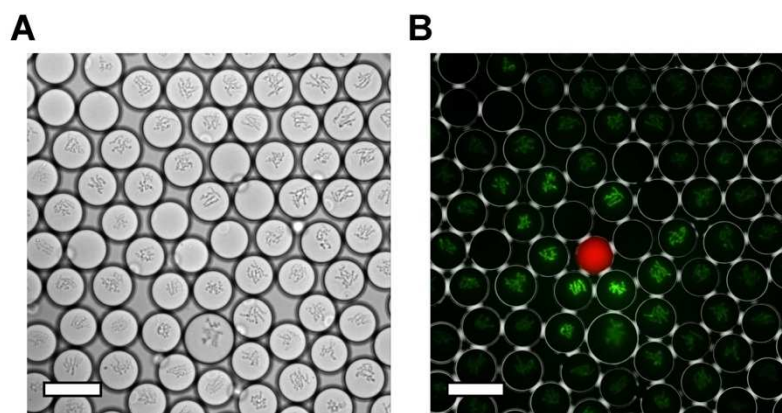
S1



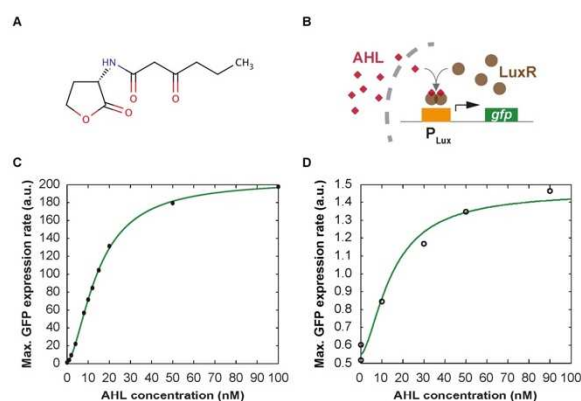
## 1 Supplementary Figures



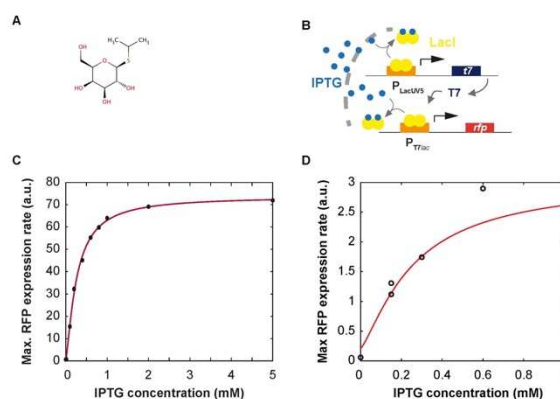
**SI Figure 1** Example image for expression of GFP in encapsulated *E. coli* cells, which were induced with 20 nM AHL before droplet generation. (A) Microscopy images in bright field (top) and fluorescence (bottom) mode at 11 min and 490 min after start of the experiment of 155 droplets containing receiver cells induced by 20 nM AHL. The scale bars are 100  $\mu\text{m}$ . (B) Fluorescence image overlaid with droplet boundaries found by the analysis software. (C) Fluorescence time traces of droplets shown in (A) normalized to their areas. Time traces remaining at low fluorescence values are from empty droplets.



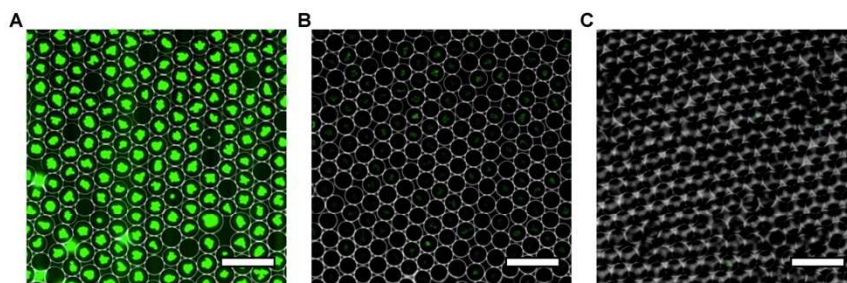
**SI Figure 2** Microscopy images in 40x magnification of droplets containing sender and receiver droplets shown in Fig. 2 in the main text. (A) Bright field image. (B) Merged images taken in GFP and RFP fluorescence mode overlaid by droplet boundaries obtained from inverted bright field images 18h after initiation of the experiment. The scale bar is 50  $\mu\text{m}$ .



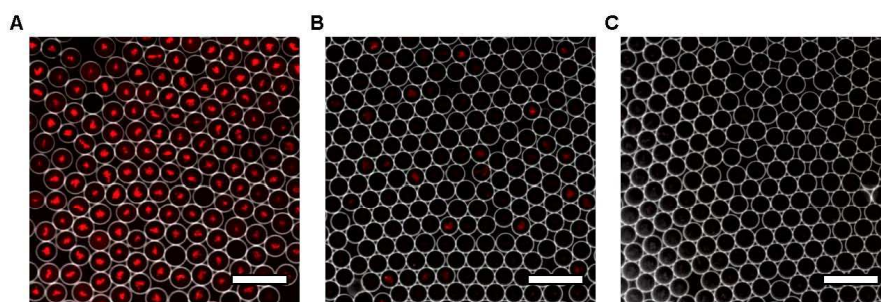
**SI Figure 3** Characterization of the AHL receiver module. (A) Chemical structure of 3OC6HSL. (B) Schematic illustration of the receiver gene circuit. AHL enters a receiver cell by permeation through the cell membrane (gray dashed line) and binds to constitutively expressed LuxR. LuxR:AHL complexes further dimerize and activate expression of a green fluorescent protein (GFP). (C) Transfer function for induction of GFP expression by AHL determined in bulk measurements on a plate reader. *Max. GFP expression rates* (black dots) are the largest value of the first derivative of  $OD_{600}$ -normalized GFP time traces for different AHL concentrations, typically around 2 h after addition of inducers. Fit of a Hill-curve results in a Hill exponent of 1.6 and  $K_{AHL} = 15$  nM. (D) Maximum GFP expression rates of receiver cells encapsulated within microdroplets with different AHL inducer concentrations (empty circles). Also shown is a scaled transfer function with the same Hill-exponent and induction threshold as derived from the bulk experiments shown in (C).



**SI Figure 4** Characterization of IPTG receiver circuit. (A) Chemical structure of isopropyl-β-D-thiogalactopyranoside. (B) Schematic illustration of the IPTG receiver genetic circuit. IPTG (blue) enters a receiver cell, sequesters the transcription repressor LacI (yellow), and activates expression of a red fluorescent protein (RFP). (C) Transfer function for induction of RFP expression by IPTG determined in bulk measurements on a plate reader. *Max. RFP expression rates* (black dots) are the largest value of the first derivative of OD<sub>600</sub>-normalized RFP time traces for different IPTG concentrations, typically after 2 h. Fit of a Hill-curve reveals a Hill exponent of 1.3 and  $K_{IPTG} = 0.26$  mM. (D) Maximum RFP expression rates of IPTG receiver cells encapsulated within microdroplets with different IPTG concentrations (empty circles). The continuous line is a scaled transfer function with the same Hill-exponent and threshold as for the bulk experiments shown in (C).

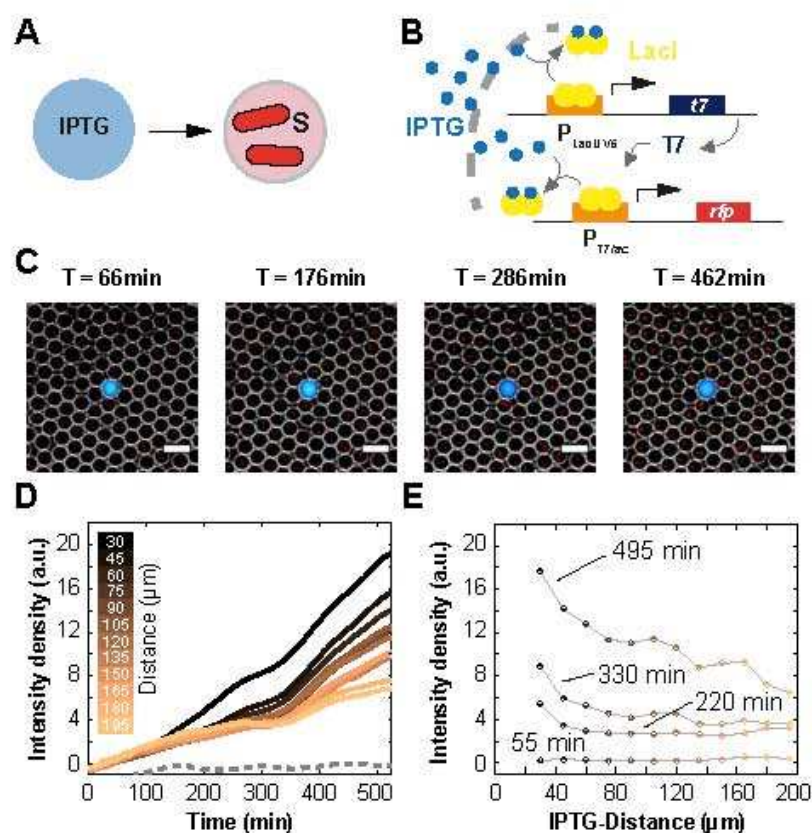


**SI Figure 5** Control experiment to investigate the solubility of 3OC6HSL in FC-40 oil. Fluorescence images are taken in GFP mode 12 h after encapsulation. Scale bars are 100 μm. (A) Encapsulated AHL receiver cells initially induced by mixing with 20 nM 3OC6HSL showing bright green fluorescence. (B) 3OC6HSL containing reservoir droplets were produced and incubated for 3 h. After incubation, only the oil phase was carefully extracted (without droplets) and transferred to a channel with droplets containing non-induced receiver cells. The latter were produced in fresh oil. (C) Droplets containing uninduced receiver cells. Droplet surfaces overlap because droplets did not arrange in a monolayer in this experiment. Due to the absence of incubated oil green fluorescence is considerably lower than in (B) indicating that 3OC6HSL was partly dissolved in oil during incubation.



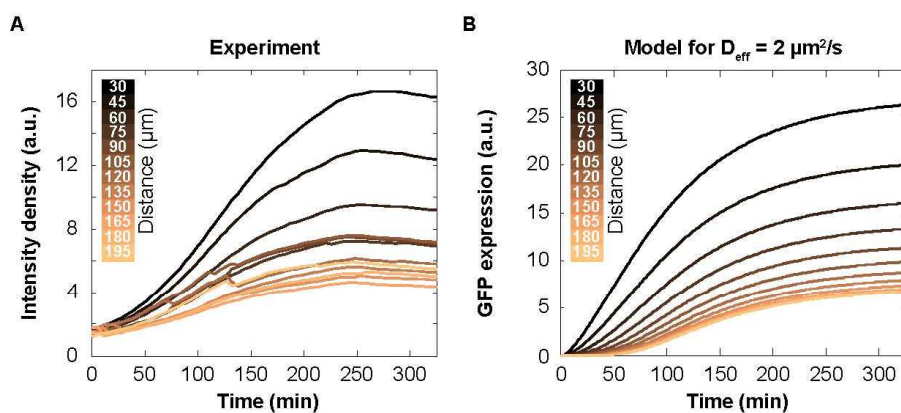
**SI Figure 6** Control experiment to investigate the solubility of IPTG in FC-40 oil. Fluorescence images are taken in RFP mode 12 h after encapsulation. Scale bars are 100  $\mu\text{m}$ . (A) Encapsulated IPTG receiver cells initially induced by mixing with 100 mM IPTG showing bright red fluorescence. (B) IPTG containing reservoir droplets were produced and incubated for 3 h. After incubation, only the oil phase was carefully extracted and transferred to a channel with droplets containing non-induced receiver cells. The latter were produced in fresh oil. (C) Droplets containing uninduced receiver cells. Due to the absence of incubated oil red fluorescence is considerably lower than in (B) indicating that IPTG was partly dissolved in oil during incubation.



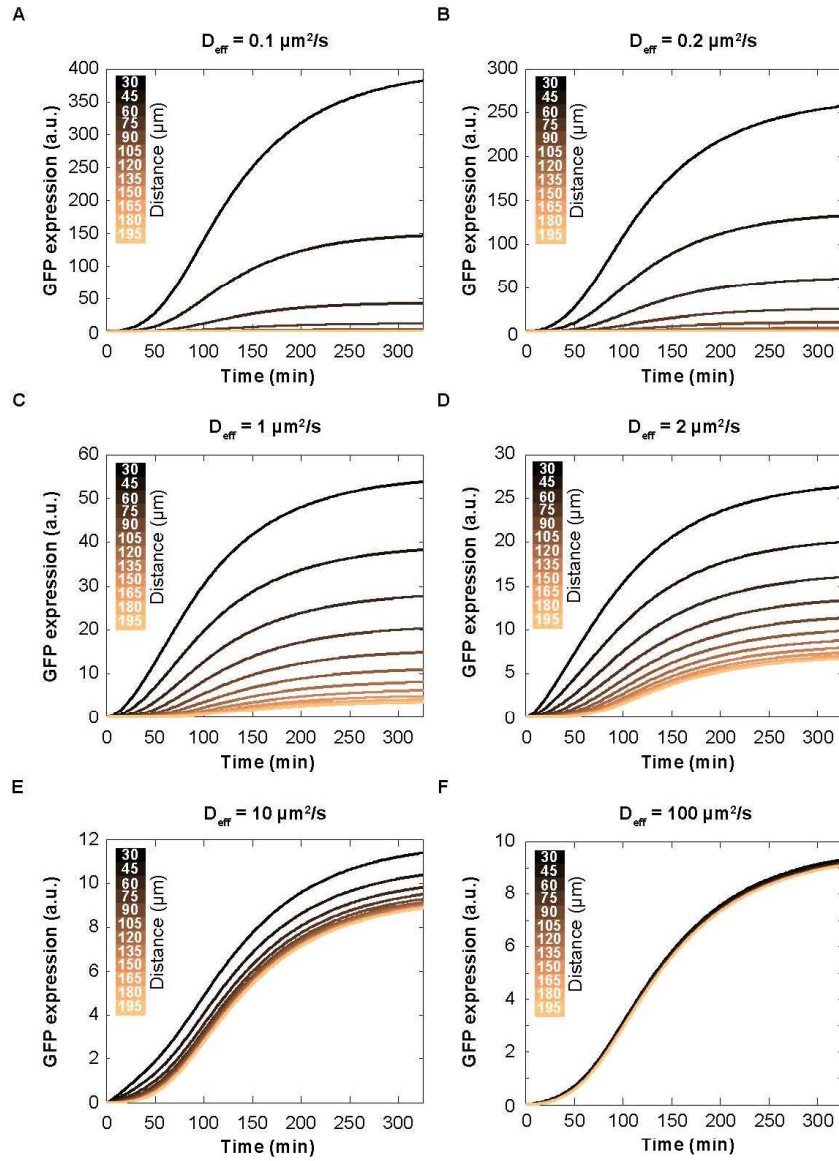


**SI Figure 7** Receiver bacteria in the presence of IPTG reservoir droplets. (A) Scheme of the transduction of IPTG from a reservoir droplet to a receiver droplet. (B) Schematic illustration of the receiver genetic circuit. IPTG enters a receiver cell by penetrating the cell membrane and sequestering the transcription repressor LacI, upon which expression of a red fluorescent protein is activated. (C) Microscopy time series in fluorescence mode of receiver cells in proximity of an IPTG reservoir droplet (blue). White circles represent droplet boundaries derived from inverted bright field images. IPTG is transduced through the oil phase upon diffusion and triggers the expression of a red fluorescent protein in receiver cells (red) as soon as a critical concentration is exceeded. The scale bar is 50  $\mu\text{m}$ . (D) Evolution of average fluorescence intensity of droplets containing receiver cells in dependence on the distance from IPTG reservoir droplets. The gray dashed line corresponds to the mean fluorescence of IPTG receiver cells in droplets in the absence of IPTG. (E) Intensity profile of traces shown in (D) after 55, 220, 330 and 495 min.

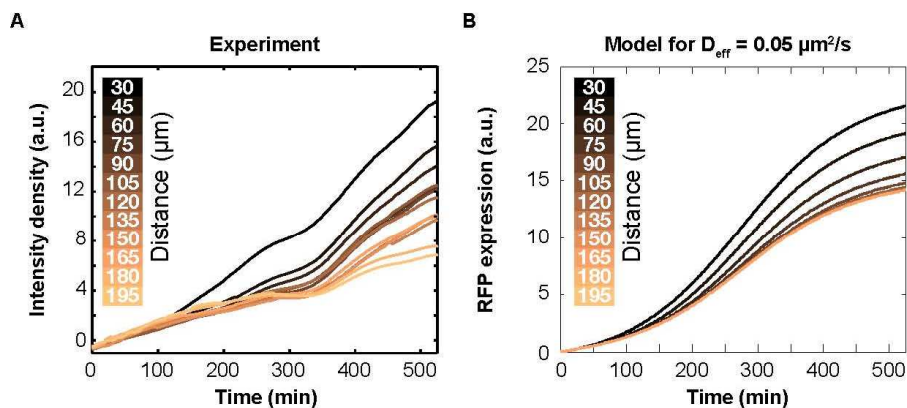




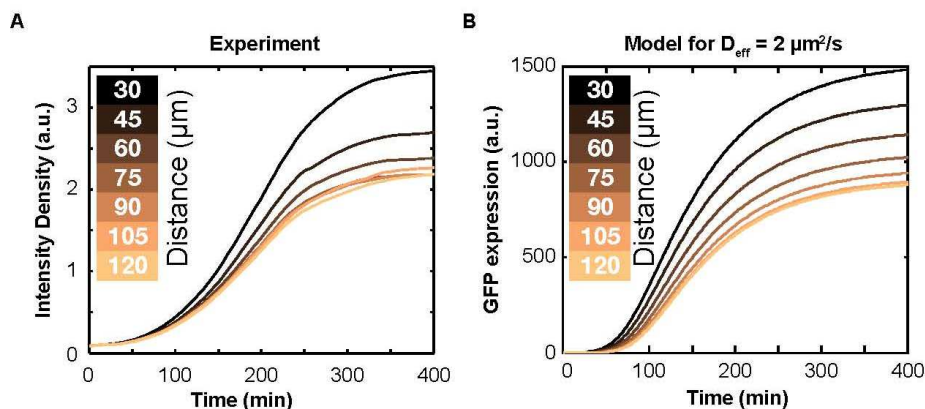
**SI Figure 8** Receiver bacteria in the presence of AHL reservoir droplets in experiment and model. Temporal evolution of the average GFP intensity of receiver bacteria in droplets in (A) the experiment and in (B) a simple theoretical model which assumes a reduced effective diffusion constant of  $D_{\text{eff}} = 2 \mu\text{m}^2/\text{s}$ . The distances of receiver cell droplets from the center of a reservoir droplet filled with 200 nM AHL are color-coded. For details see SI section **Modeling**.



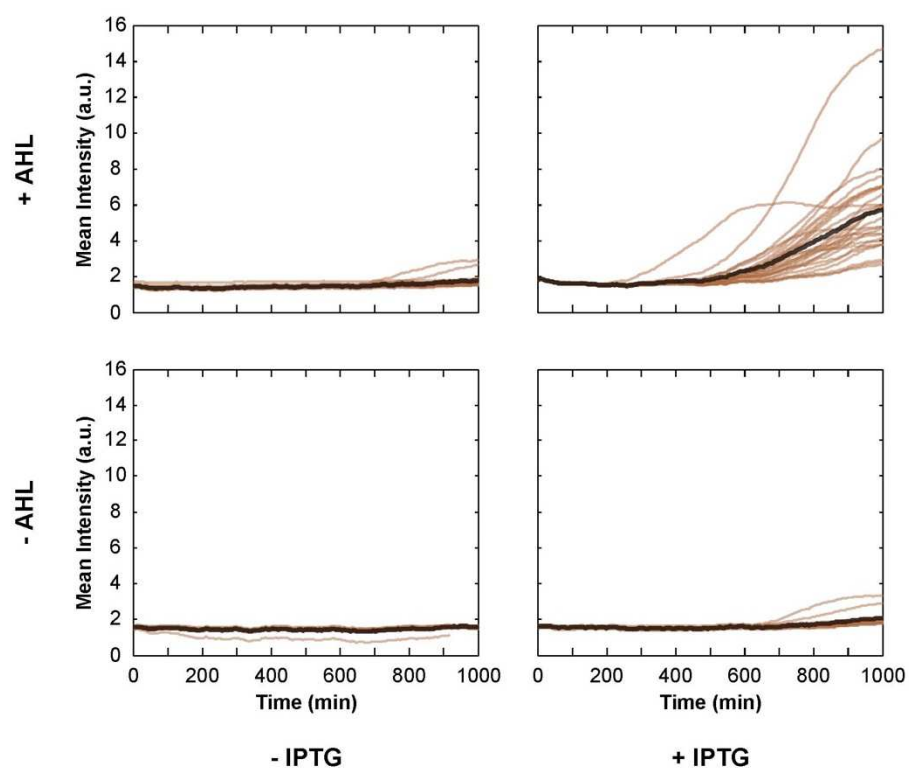
**SI Figure 9** Modeling results for receiver bacteria in the presence of AHL reservoir droplets. The diagrams show the temporal evolution of the average GFP intensity of receiver bacteria in droplets in predicted by a simple theoretical model which assumes reduced effective diffusion constants  $D_{\text{eff}}$  of (A)  $0.1 \mu\text{m}^2/\text{s}$ , (B)  $0.2 \mu\text{m}^2/\text{s}$ , (C)  $1 \mu\text{m}^2/\text{s}$ , (D)  $2 \mu\text{m}^2/\text{s}$ , (E)  $10 \mu\text{m}^2/\text{s}$  and (F)  $100 \mu\text{m}^2/\text{s}$ . The distances of receiver cell droplets from the center of a reservoir droplet filled with 200 nM AHL are color-coded. For details see SI section **Modeling**.



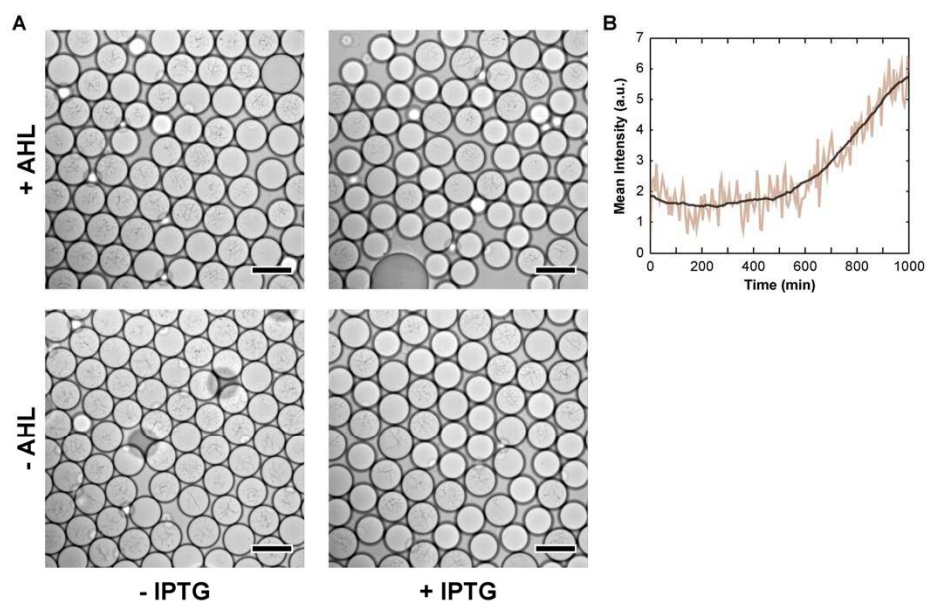
**SI Figure 10** Receiver bacteria in the presence of IPTG reservoir droplets in experiment and model. Temporal evolution of the average RFP intensity of receiver bacteria in droplets in (A) the experiment and in (B) a simple theoretical model which assumes a reduced effective diffusion constant of  $D_{\text{eff}} = 0.05 \mu\text{m}^2/\text{s}$ . The distances of receiver cell droplets from the center of a reservoir droplet filled with 10 mM IPTG are color-coded. For details see SI section **Modeling**.



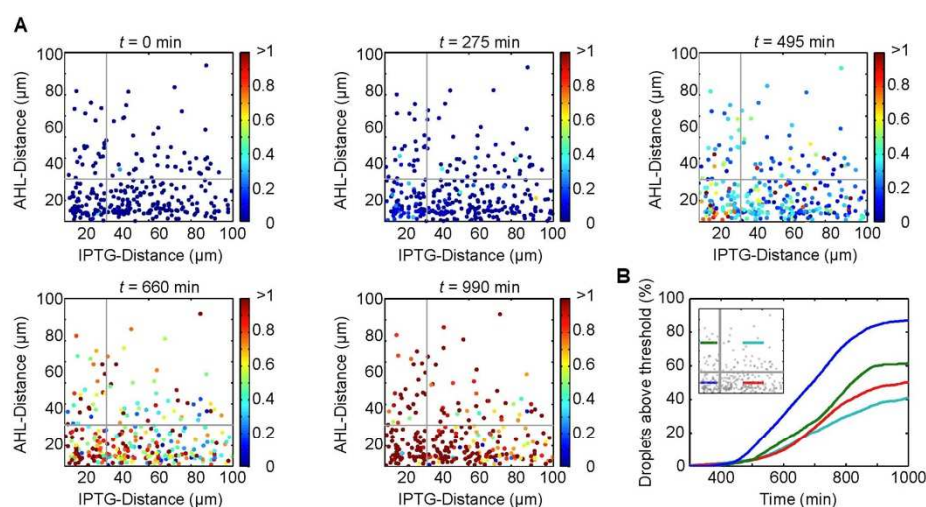
**SI Figure 11** Receiver bacteria in the presence of droplets containing AHL producing sender cells in experiment and model. Temporal evolution of the average GFP intensity of receiver bacteria in droplets in (A) the experiment and in (B) a simple theoretical model which assumes a reduced effective diffusion constant of  $D_{\text{eff}} = 2 \mu\text{m}^2/\text{s}$ . The distances of receiver cell droplets from the center of a sender droplet are color-coded. For details see SI section **Modeling**.



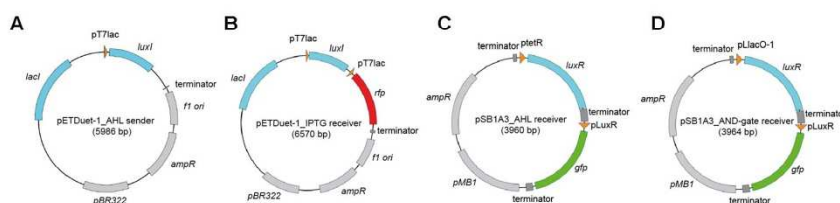
**SI Figure 12** Single droplet fluorescence time traces (light brown) and population mean (dark brown) of AND-gate bacteria in the presence of different inducer droplet combinations as shown in the main text Fig. 3E. The '+IPTG | + AHL' panel contains 27 traces, the others contain 20 traces, from which in each case the mean traces were derived.



**SI Figure 13** AND-gate bacteria in microdroplets. (A) Bright field micrographs of fluorescence images shown in main text Fig. 3e. The scale bar is 50  $\mu\text{m}$ . (B) Example trace of AND-gate bacteria (+ AHL / + IPTG) droplet population mean raw data (light brown) and after smoothing applying a moving average in a 41 data points window.



**SI Figure 14** Spatial response of AND-gate bacteria in microdroplets in the presence of reservoirs with high AHL and IPTG concentrations. (A) The fluorescence of 466 AND-gate droplets is shown as a function of their distance to the next AHL and IPTG reservoir droplets of which there were in total 265 and 87, respectively. Reservoir droplets contained 200 nM AHL and 10 mM IPTG and were identified by TAMRA and ATTO 655 reference dyes added to the buffer solution. GFP fluorescence rises close to both types of reservoirs first (panels for  $t = 465$  and  $t = 660$  min). Due to the high inducer concentration, however, for long waiting times the induction threshold is finally exceeded everywhere. Thus, the spatial pattern generated by the AND gate only exists transiently. (B) Fraction of droplets in the indicated quadrants above a given fluorescence threshold (0.1 in the units of (A)); blue: close to both types of reservoir droplets (distance  $\leq 40 \mu\text{m}$ ); green: receivers close ( $\leq 40 \mu\text{m}$ ) to IPTG, but far ( $\geq 40 \mu\text{m}$ ) from AHL droplets; red: close to AHL and far from IPTG reservoirs; light blue: far from both types of inducer reservoirs.



**SI Figure 15** Plasmid maps of constructs used in this study: (A) AHL sender, (B) IPTG receiver, (C) AHL receiver and (D) AND-gate receiver plasmid



## 2 Supplementary Tables

**Table 1** Primers used in this study

| Primer              | Sequence*  |
|---------------------|--|
| <i>rfp_fwd</i>      | 5'-ccgtccatgatggcttcctccgaagacg-3'<br><i>NdeI</i>  |
| <i>rfp_rev</i>      | 5'-gcagcttaattaagcgatctacactagcactatc-3'<br><i>PacI</i>  |
| <i>ptet_del_fwd</i> | 5'-agatactgagcactactagagaaagagg-3'   |
| <i>ptet_del_rev</i> | 5'-ctctagaagcggccgcgaattc-3'   |
| <i>pLlacO-1_fwd</i> | 5'-gaattcgcgccgcttctagagctgataaatgtgagcggataacattgac<br>attgtgagcggataacaagatactgagcactactagagaaagagg-3' |
| <i>pLlacO-1_rev</i> | 5'-cctcttctctagtagtgctcagtatctgttatccgctcacaatgtcaatgttat<br>ccgctcacatttatcagctctagaagcggccgcgaattc-3'  |

\*Relevant restriction sites are underlined.

### 3 Supplementary Materials

#### Bacterial strains and culture media

Studies with sender and receiver cells were performed using *Escherichia coli* strain BL21(DE3)pLysS (Promega). AND-gates were constructed in *Escherichia coli* DH5 $\alpha$ Zi (ExpressSys), while subcloning was generally performed with *Escherichia coli* DH5 $\alpha$  (Life Technologies). For strain cultivation, Luria-Bertani (LB) medium (Carl Roth, #X968.1) was used with 100  $\mu$ g/ml Carbenicillin (Carl Roth) and 30  $\mu$ g/ml Chloramphenicol (Carl Roth) antibiotics. For chemical communication studies in droplets, LB medium or M9 minimal medium (in the case of AND-gate containing cells) supplemented with 20 mM Glucose and 300  $\mu$ g/ml thiamine hydrochloride (Sigma-Aldrich, #T1270) was used with antibiotic concentrations reduced to 50%.

### 4 Supplementary Methods

#### 4.1 Cell growth

Cells from glycerol stock were recovered in Falcon tubes with 5 ml LB medium and grown overnight at 37 °C shaken at 250 rpm. The overnight cultures were diluted to an initial optical density (OD<sub>600nm</sub>) of 0.01 in Falcon tubes containing fresh LB or M9 minimal medium (Sigma-Aldrich, #M6030). The cells were incubated at 37 °C while shaking for 2 - 3 more hours. Once the diluted cultures reached an OD<sub>600nm</sub> of 0.1 – 0.2, they were transferred into microemulsion droplets for communication studies.

#### 4.2 Plasmid construction

**Senders:** luxI synthase (BioBrick part BBa\_C0261) gene from *Aliivibrio fischeri* was cloned into pETDuet-1 expression vector (Merck Millipore) between BioBrick's cloning sites XbaI and PstI. The multiple cloning sites (MCS) of the vector precede an IPTG inducible T7 promoter. In the compatible host strain *Escherichia coli* BL21(DE3)pLysS, expression is driven by T7 RNA polymerase. To aid the visualization of sender droplets, the monomeric reporter gene rfp was amplified directly from the template BBa\_E1010 by polymerase chain reaction (PCR) with primers (rfp\_fwd, rfp\_rev) that comprise *NdeI* and *PacI* restriction sites. We performed double digestion of both, the PCR fragment and the plasmid and ligated them according to standard protocols. **Receivers:** the BioBrick part BBa\_T9002 on pSB1A3 plasmid was transformed to *Escherichia coli* BL21(DE3)pLysS. **AND-receivers:** T9002 cells were modified to AND-receiver cells. Here, we put *luxR* gene under control of pLlacO-1<sup>1</sup> and *gfp* under plux promoter. To achieve the logic operation, T9002\_pSB1A3 plasmid was linearized by deletion PCR with ptet\_del primers followed by circular polymerase extension cloning (CPEC)<sup>2</sup>. CPEC was used to insert placO-1 promoter with the overlapping pLlacO-1 primers. All primer sequences can be seen in Tab. S1. The final plasmid constructs used in this study are shown in Fig. S14.

#### 4.3 Generation of emulsions

Microemulsion droplets were generated in a microfluidic PDMS device with flow-focus channel geometry. In order to avoid cross contamination during droplet formation, new devices were used when droplet content was changed. To prevent inner channel walls from wetting by the aqueous phase, the

microfluidic chips were baked at 200 °C for 3 h, which results in hydrophobic surfaces<sup>3</sup>. Fluid fluxes were controlled with syringe pumps (TSE Systems). Typical pumping rates were 100 µl/h for the aqueous phase containing the bacteria and 300-500 µl/h for the oil phase. The oil phase was comprised of fluorocarbon oil (Fluorinert® FC-40 from Sigma-Aldrich) containing 1.8 % (w/v) non-ionic surfactant (RainDance Technologies, #E2K0660). During production, droplets were stored in a tygon tubing reservoir, which was connected to the microfluidic chip's outlet. When a sufficient amount of droplets was generated the emulsion was transferred to ibidi microslides. We typically started with droplets containing uninduced bacteria followed by IPTG and AHL. To mix successively generated droplets in the ibidi channels the slide was gently spun before it was mounted in the microscope for long term observation.

#### 4.4 Communication modes

AI droplets communicating with receiver droplets: receiver cells were cultivated and encapsulated as described above. During communication studies in droplets, the LB medium for reservoir droplets was supplemented with 200 nM 3OC6HSL (Sigma-Aldrich, #K3007) and 500 nM Alexa488 dye (Life Technologies) to visualize the droplets. IPTG droplets inducing sender droplets: Reservoir droplets were filled with 10 mM IPTG (Roth, #CN08.2) inducer and stained with 500 nM Texas Red (Life Technologies). Sender cell droplets communicating with receiver droplets: sender cells were induced with 1 mM IPTG before encapsulation. For long-term observations in the microscope droplets were transferred from microfluidic channels to uncoated micro slides (ibidi, #80601). Genetic AND gate processing: AHL (20 nM, Fig.

S16

3d, e, and 200 nM, Fig. S14) and IPTG (200  $\mu$ M, Fig. 3d, e, and 10 mM Fig. S14) containing droplets and bacteria droplets were successively generated and mixed in a microfluidic channel. For AND-gate experiments, AHL droplets were supplemented with 1  $\mu$ M TAMRA (Sigma-Aldrich) and IPTG reservoirs were supplemented with 1  $\mu$ M ATTO 655 (Atto-Tec) for visualization purposes.

#### 4.5 Characterization of genetic circuits

In order to characterize the circuits, bulk measurements were performed on a plate reader (FLUOstar Optima, BMG Labtech) in 96-well plates in which the expression of the fluorescent reporter protein was followed at the appropriate wavelength for varying inducer concentrations and the cell growth was monitored by simultaneous absorption measurements at 600 nm. As a measure for the resulting degree of induction, the maximum value of the first derivative of blank corrected and absorption-normalized fluorescence time traces was determined for each inducer concentration (mean of three independent measurements), which represents the cells' maximum protein expression rate. For AHL and IPTG receiver cells, transfer function parameters were derived by fitting a Hill equation

$$y(C) = y_0 + \frac{y_{max}}{1 + \left(\frac{K}{C}\right)^n}$$

to the maximum protein expression rates  $y$  depending on inducer concentrations  $C$ , where  $y_{max}$  and  $y_0$  are the maximum protein expression rates at full activation and the basal expression level in the absence of inducers,  $K$  is the inducer concentration at the threshold or switching point and  $n$  is the Hill exponent. Transfer curves are shown in SI Fig. 3 for AHL and SI Fig. 4 for IPTG receivers. The resulting parameters are for AHL:

S17

- $y_{\max, \text{AHL}} = 179.4 \pm 6.2$  (a.u./min)
- $y_{0, \text{AHL}} = 0.3 \pm 2.4$  (a.u./min)
- $K_{\text{AHL}} = 15 \pm 0.7$  nM
- $n_{\text{AHL}} = 1.6 \pm 0.1$

and for IPTG

- $y_{\max, \text{IPTG}} = 73.4 \pm 1.5$  (a.u./min)
- $y_{0, \text{IPTG}} = 0.3 \pm 0.7$  (a.u./min)
- $K_{\text{IPTG}} = 0.3 \pm 0.01$  mM
- $n_{\text{IPTG}} = 1.3 \pm 0.1$ .

Values for  $K_{\text{AHL}}$  and the Hill exponent  $n_{\text{AHL}}$  are in the range of literature values for  $K_{\text{AHL}}$  1.4 – 100 nM and  $n_{\text{AHL}}$  0.9 – 1.8 .<sup>4</sup>

For AND-gate bacteria, we determined Hill coefficients and threshold concentrations for both inducers by fitting a 2-dimensional input function assuming two independent activators<sup>5</sup>

$$y(C_1, C_2) = y_0 + \frac{y_{\max}}{\left(1 + \left(\frac{K_1}{C_1}\right)^{n_1}\right) \left(1 + \left(\frac{K_2}{C_2}\right)^{n_2}\right)}$$

to maximum protein expression rates  $y$  depending on inducer concentrations  $C_1$  and  $C_2$ , where  $y_{\max}$  and  $y_0$  are the maximum protein expression rates at full activation and at basal expression level,  $K_1$  and  $K_2$  are the inducer concentrations at the threshold or switching point and  $n_1$  and  $n_2$  are the Hill exponents. The fitting result of the 2-dimensional transfer equation is shown in main text Fig. 3c. The fitted parameters are  $y_{\max} = 150.3 \pm 8.1$  (a.u./min),  $y_0 = 4.5 \pm 3.0$  (a.u./min),  $K_{\text{IPTG}} = 0.02 \pm 0.00$  mM,  $n_{\text{IPTG}} = 1.5 \pm 0.2$ ,  $K_{\text{AHL}} = 1.7 \pm 0.2$  nM and  $n_{\text{AHL}} = 1.5 \pm 0.2$ . All bulk measurements were performed at 37° C.



#### 4.6 Time-lapse microscopy

Time-lapse microscopy measurements were conducted on an Olympus IX81 epifluorescence microscope controlled with CellSense. The microscope setup was equipped with an EMCCD camera iXon3 (Andor), an automated x-y-stage (Prior Scientific, Cambridge, UK) and an incubator box (Okolab) to maintain an operation temperature of 37° C. All long-term observations were performed with 10x apochromatic magnification objectives. Every 5 min, an image in bright field mode, in GFP as well as RFP fluorescence mode (in combination with the appropriate filter sets) were recorded for a total run time of at least 1000 min. The exposure times had to be adjusted according to the lifetime dependent performance of the mercury fluorescence excitation light source (X-Cite 120Q). For later subtraction of background due to auto-fluorescence of oil, a snapshot is recorded during each cycle of a position in a channel on the ibidi-slides that contains oil-surfactant-mix only.

#### 4.7 Modeling

*Bacterial growth:* In the experiments, bacterial growth is limited in terms of space by the droplet boundaries, and in terms of nutrients by the finite amount of growth medium encapsulated. The maximum number of bacteria that could be densely packed into a droplet of  $\approx 12.5 \mu\text{m}$  radius is  $\approx 8000$  (assuming a bacterial volume of 1 fL). However, we never observe complete filling. Typically, bacteria grow well in the droplets over a course of 5 – 10 hours (corresponding to roughly 10 divisions), after which usually a bacterial “colony” with a radius smaller than half the droplet radius has formed. We thus have to assume that the “carrying capacity” of the droplets is in the range of

$$N_{max} \approx 100 - 1000$$

S19

. In the following, we modeled the growth of the bacteria with a logistic function of the form:

$$N(t) = \frac{N_{max} N_0 e^{\gamma t}}{N_{max} + N_0 (e^{\gamma t} - 1)}$$

where  $\gamma$  is the cell division rate, and  $N_0$  is the initial number of bacteria in the droplets.

*AHL reservoirs:* Expression of GFP by receiver bacteria in response to AHL diffusing from a single reservoir droplet is modeled by the following simple reaction-diffusion system, in which the droplet emulsion is treated as a homogeneous medium with an effective diffusion coefficient  $D_{eff}$ . As we can only measure GFP expression *per droplet* (not per cell), bacterial growth is included in the model.

$$\begin{aligned} \frac{\partial}{\partial t} a &= D_{eff} \nabla^2 a - \delta_a a \\ \frac{d}{dt} g &= \frac{R \alpha_g a^n}{a^n + K_a^n} - \delta_g g \\ \frac{d}{dt} g_{mat} &= \alpha_{mat} g - \delta_g g_{mat} \end{aligned}$$

Here,  $a := [AHL]$ , and  $g := [GFP]$  is the concentration of nascent GFP, while  $g_{mat}$  is the concentration of matured (fluorescent) GFP,  $\alpha_g$  is the GFP expression rate at full induction,  $\alpha_{mat}$  is the maturation rate for GFP,  $n$  is the Hill exponent,  $K_a$  is the induction threshold, and  $\delta_a$  and  $\delta_g$  are effective degradation constants for AHL and GFP. Protein expression is further

S20

assumed to be proportional to the bacterial growth rate  $R = \dot{N}(\gamma, N_0, N_{max})$ , which is the derivative of the logistic function given above.

GFP concentrations are implicitly position dependent via the diffusing AHL. Constitutive LuxR production is not explicitly modeled and LuxR concentration is assumed to have reached steady state in the experiment.

We set  $n = 1.6$  and  $K_a = 15 \text{ nM}$  as determined in bulk experiments. A typical AHL degradation rate is  $\delta_a = 1 \times 10^{-5} \text{ s}^{-1}$ <sup>6</sup>. The GFP used in our experiments is stable, and we set a typical value of  $\delta_g = 2 \times 10^{-4} / \text{s}$ . The GFP maturation rate is  $\alpha_{mat} = (5 \text{ min})^{-1} = 3.3 \times 10^{-3} \text{ s}^{-1}$ <sup>7</sup>.  $\alpha_g$  is just used as a scaling parameter and is set to 1, (a typical protein production rate would be  $\sim 10 \text{ nM s}^{-1}$ ). Bacterial growth is modeled with a typical growth rate of  $\gamma = 2/h$ ,  $N_0 = 1$ , and  $N_{max} = 100$ . This leaves  $D_{eff}$  as the major unknown parameter in the model.

In Fig. S9, simulations of GFP expression dynamics for effective diffusion coefficients  $D_{eff} = 0.1, 0.2, 1, 2, 10, 100 \mu\text{m}^2/\text{s}$  are shown. Typical values used for the diffusivity of AHL in an aqueous environment are in the range  $100 - 1000 \mu\text{m}^2/\text{s}$ .

The initial conditions for the simulations are

$$\begin{aligned} a(\mathbf{r}, t = 0) &= 200 \text{ nM} && \text{for } |\mathbf{r}| < 12.5 \mu\text{m}, 0 \text{ otherwise, and} \\ g(\mathbf{r}, t = 0) &= 0 && \text{everywhere.} \end{aligned}$$

Simulations were performed with Matlab's pde solver 'pdepe' using cylindrical symmetry.

Of the plots shown in Fig. S9, the case of a strongly reduced diffusivity  $D_{eff} \approx 2 \frac{\mu\text{m}^2}{\text{s}}$  fits the experimental observations of Fig. 1d in the main text best.

As already discussed there, the simplified treatment of an isolated reservoir

droplet does not account for next-nearest neighbor droplets and higher order effects. Furthermore, leaky gene expression has not been considered in this model, which may explain the deviations between experiment and simulation. The strongly reduced diffusivity may be explained by a variety of factors (viscosity, droplet interface permeability, etc.), which are discussed in more detail in the main text.

*AHL sender bacteria:* The case of sender droplets filled with AHL producing bacteria can be described simply by the addition of an AHL production term to the equations, which is  $> 0$  for  $|r| < 12.5 \mu m$ , and  $= 0$  otherwise (Fig. S11).

*IPTG reservoirs:* IPTG droplet communication was simulated in a similar manner as for the AHL droplets. However, as indicated in the gene circuit for the IPTG receivers in Fig. S7b the process involved is slightly more complicated. T7 RNA polymerase is transcribed from the genome of the bacteria, whereas RFP-mRNA is transcribed by T7 RNAP from a LacI-controlled T7 promoter. We thus assumed:

$$\begin{aligned} \frac{\partial}{\partial t} i &= D_{\text{eff}} \nabla^2 i - \delta_i i; & \frac{d}{dt} t &= R\alpha_0 + \frac{R\alpha_t i^m}{i^m + K_i^m} - \delta_t t \\ \frac{d}{dt} r &= R\alpha_0 + \frac{R\alpha_r i^m}{i^m + K_i^m} \frac{t}{t + K_t} - \delta_r r; & \frac{d}{dt} r_{\text{mut}} &= \alpha_{\text{mut}} r - \delta_r r_{\text{mut}} \end{aligned}$$

Here,  $i := [IPTG]$ ,  $t := [T7RNAP]$ ,  $r := [RFP]$ ,  $\alpha_t, \alpha_r, \delta_i, \delta_v, \delta_r$  are corresponding production and degradation rates,  $m, K_i$  are Hill exponent and activation threshold for LacI-controlled expression, while  $K_t$  describes the binding of T7

S22

RNAP to its promoter.  $\alpha_0$  is a leak expression rate,  $\alpha_{mat}$  is the maturation rate as before. Cell growth  $R = \dot{N}(\gamma, N_0, N_{max})$  is observed to be slower than for the AHL receivers, which is accounted for by  $\gamma = 0.5/h$ .

Due to the larger number of parameters, adjusting the model to the experiment is more arbitrary than for the AHL case. As shown in Fig. S10, we achieve reasonable agreement with Fig. S7, if we assume a considerable leak transcription and a strongly reduced diffusivity of  $D_{eff} = 0.05 \frac{\mu m^2}{s}$ . This seems reasonable in light of the fact that IPTG is less amphiphilic than AHL and presumably penetrates the oil phase more slowly. Parameter settings for the simulation are:

$\alpha_0 = 0.02 s^{-1}$ ,  $\alpha_t = 0.1 s^{-1}$ ,  $\alpha_r = 10 s^{-1}$ ,  $\alpha_{mat} = 3.3 \times 10^{-3} s^{-1}$ ,  $\delta_i = 0$ ,  $\delta_t = 1 \times 10^{-5} s^{-1}$ ,  $\delta_r = 2 \times 10^{-4} s^{-1}$ .  $m = 1.3$  and  $K_i = 0.26 mM$  were taken from characterization experiments,  $K_t$  is set to 1nM. The initial concentration was taken as  $i(\mathbf{r}, t = 0) = 10 mM$  for  $|\mathbf{r}| < 12.5 \mu m$ , and = 0 elsewhere.

#### *Reduced diffusivity between droplets – discussion:*

As discussed above (cf. also Fig. S8-S11), the dynamics of gene expression in receiver droplets are consistent with an RD model of the system, but only with the assumption of strongly reduced 'effective' diffusion coefficients of the inducer molecules. This may be caused by a variety of different factors. In general, diffusion within heterogeneous systems as in the microemulsions considered here depends on several parameters, in particular on the diffusion coefficient in the different phases, the permeability  $\kappa$  of the interfaces, and geometrical effects (characterized by the 'tortuosity' of the system). Diffusion coefficients of small compounds in water are typically in the range  $D_0 = 100 -$

S23

1000  $\mu\text{m}^2/\text{s}$ . The four times higher viscosity of FC-40 oil ( $\eta = 4.1 \text{ mPa s}$  at 25 °C) with respect to water suggests a diffusion coefficient that is reduced by this factor, which alone cannot account for our observations. A well-known result for the effective diffusion coefficient in a system of membranes separated by a medium with diffusion coefficient  $D$  and periodically spaced with a distance  $a$  is  $D_{\text{eff}}^{-1} = D_0^{-1} + (\kappa a)^{-1}$ <sup>8</sup>. This relation becomes considerably more involved for varying diffusion coefficients and more general geometries<sup>8c,8d</sup>, but indicates that for very low permeability  $\kappa$  (which presumably holds in our case) the effective diffusivity is simply given by  $D_{\text{eff}} \approx \kappa a$ . An alternative transport mechanism could be ‘unhindered’ diffusion through a surfactant double layer formed between touching microdroplets. In this case, the free diffusion coefficient would be reduced by a tortuosity factor  $\tau \sim r_d/d$ , where  $r_d$  is the radius of the droplets and  $d$  that of the contact region<sup>9</sup>. Thus, with small droplet spacings  $a$  and permeabilities  $\kappa$ , as well as for small droplet contact areas  $\sim d^2$ , a strongly reduced  $D_{\text{eff}}$  is easily conceivable in both scenarios.

## REFERENCES

- (1) Lutz, R.; Bujard, H. *Nucl. Ac. Res.* **1997**, *25*, 1203.
- (2) Quan, J.; Tian, J. *PLoS ONE* **2009**, *4*, e6441.
- (3) Kaneda, S.; Ono, K.; Fukuba, T.; Nojima, T.; Yamamoto, T.; Fujii, T. *Anal. Sci.* **2012**, *28*, 39.
- (4) aUrbanowski, M. L.; Lostroh, C. P.; Greenberg, E. P. *J. Bacteriol.* **2004**, *186*, 631; bCanton, B.; Labno, A.; Endy, D. *Nat Biotech* **2008**, *26*, 787.
- (5) aAckers, G. K.; Johnson, A. D.; Shea, M. A. *Proc Natl Acad Sci U S A* **1982**, *79*, 1129; bGerland, U.; Moroz, J. D.; Hwa, T. *Proc Natl Acad Sci U S A* **2002**, *99*, 12015.
- (6) Hense, B. A.; Kuttler, C.; Müller, J.; Rothballer, M.; Hartmann, A.; Kreft, J. U. *Nat. Rev. Microbiol.* **2007**, *5*, 230.
- (7) Iizuka, R.; Yamagishi-Shirasaki, M.; Funatsu, T. *Anal Biochem* **2011**, *414*, 173.
- (8) (a) Crick, F. *Nature* **1970**, *225*, 420; (b) Tanner, J. *J. Chem. Phys.* **1978**, *69*, 1748;
- (c) Latour, L.; Svoboda, K.; Mitra, P.; Sotak, C. *Proc. Nat. Acad. Sci.* **1994**, *91*, 1229;
- (d) Sen, P. *J. Chem. Phys.* **2003**, *119*, 9871.
- (9) Berezhkovskii, A. M.; Zitserman, V. Y.; Shvartsman, S. Y. *J. Chem. Phys.* **2003**, *118*, 7146.



### 5.3. Chemical communication between bacteria and cell-free gene expression systems within linear chains of emulsion droplets

Electronic Supplementary Material (ESI) for Integrative Biology.  
This journal is © The Royal Society of Chemistry 2016

#### **Supplementary Information: Chemical communication between bacteria and cell-free gene expression systems within linear chains of emulsion droplets**

M. Schwarz-Schilling,<sup>a</sup> L. Aufinger,<sup>a</sup> A. Mückl<sup>a</sup> and F. C. Simmel<sup>a,b</sup>

<sup>a</sup> Technical University of Munich, Physics Department E14 and ZNN/WSI, Am Coulombwall 4a, 85748 Garching, Germany

<sup>b</sup> Nanosystems Initiative Munich, Schellingstr. 4, 80539 München, Germany

#### **Table of contents**

1. Bulk characterization of synthetic gene circuits
2. Diffusion of inducers in droplet emulsions
  - 2.1 Analytical treatment
  - 2.2 Reaction-diffusion modelling
  - 2.3 Discussion
3. pH changes in the cell-free transcription/translation system
4. Additional data – AHL and IPTG reservoir for bacteria and cell free system
5. SI methods
  - 5.1 Data processing
  - 5.2 Filling of the capillaries
  - 5.3 Plasmid maps

Supplementary References

### 1. Bulk characterization of synthetic gene circuits

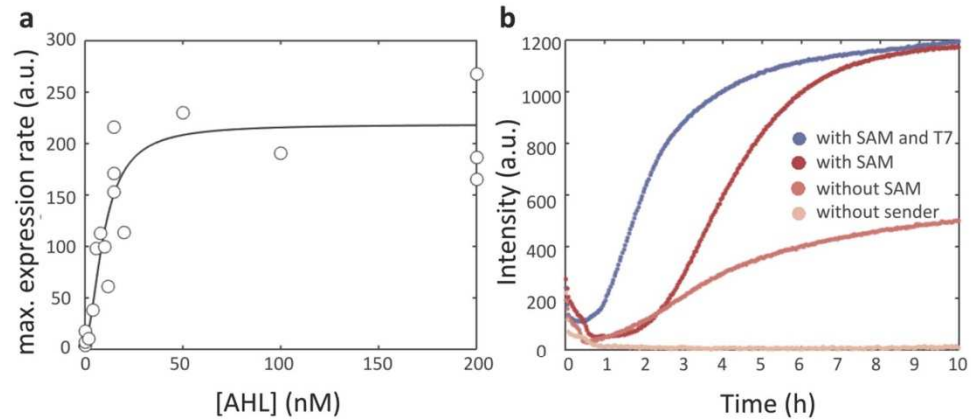


**Figure S1: Bulk characterization experiments.** **a)** Maximum GFP expression rate under control of the lux promoter for varying concentration of AHL. A fit with a Hill curve (continuous line) results in a Hill exponent of  $n=1.8$  and an induction threshold at  $K_a \approx 9.9$  nM. **b)** GFP production recorded in a bulk experiment with sender and receiver plasmids in a cell-free gene expression system. Addition of S-adenosyl methionine (a precursor for the production of the AHL 3-oxo-hexanoyl-L-homoserine lactone by LuxI) considerably increases the production of GFP. Addition of T7 RNA polymerase leads to faster production.

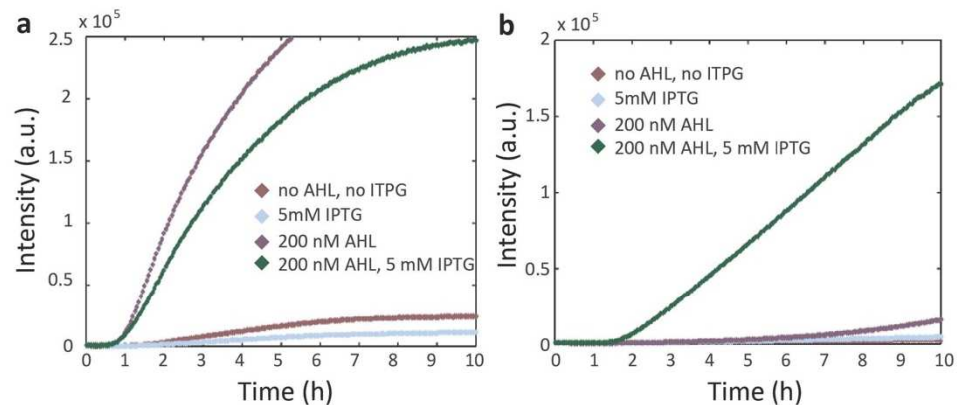


**Figure S2: Bulk experiment with the AND gate in a cell-free system without and supplemented with Lacl.** **a)** GFP expression without addition of Lacl. The cell free system contained AND gate plasmid at 7.5 nM concentration. The GFP production is clearly suppressed in the absence of AHL. However, IPTG only has a minor influence due to a shortage of Lacl in the cell extract. **b)** Supplementing the cell free system with  $\approx 200$  nM His-tagged purified Lacl suppresses the GFP production in the absence of either AHL or IPTG or both (bulk experiment with 7.5 nM of AND gate plasmid), and thus restores the AND gate behaviour with AHL and IPTG as input. This can also be achieved by reducing the plasmid concentration to about 1 nM (data not shown).

## 2. Diffusion of inducers in droplet emulsions

### 2.1 Analytical treatment

For an analytical description of our system, we first assume that the transport of the inducer AHL in our quasi-1D droplet emulsion can be treated as a simple diffusion process with an apparent diffusion coefficient  $D_a$ . The corresponding 1D diffusion equation for the concentration  $a := [\text{AHL}]$  in the capillary reads:

$$\frac{\partial a}{\partial t} = D_a \frac{\partial^2 a}{\partial x^2}, \quad (1)$$

Assuming a constant AHL concentration  $a_0$  at the end of the capillary in contact with the reservoir ( $x = 0$ ) and zero concentration (infinitely) far inside the capillary, the boundary conditions are:

$$a(0, t) = a_0, \quad a(x \rightarrow \infty, t) = 0.$$

The initial concentration inside the capillary is zero:  $a(x, 0) = 0, x > 0$ .

The analytical solution to this semi-infinite system is the complementary error function:

$$a(x, t) = a_0 \cdot \text{erfc}\left(\frac{x}{\sqrt{4D_a t}}\right). \quad (2)$$

Thus, the distance  $x(t)$  at which the AHL concentration has reached a given activation threshold  $K_a$  at time  $t$  is given by:

$$x(t) = \sqrt{4D_a t} \cdot \text{erfc}^{-1}\left(\frac{K_a}{a_0}\right). \quad (3)$$

If we assume that for very large reservoir concentrations  $a_0$  the AHL concentration in any given droplet quickly sweeps from essentially zero to saturation (well above  $K_a$ ), the time  $t_{on}(x)$  at which GFP production starts is approximately given by the time at which the AHL diffusion front reaches the droplet (this will be true at least for the droplets closest to the reservoir). As shown in Figure S3b, we estimate  $t_{on}(x)$  by measuring the time  $t_1(x)$ , it takes until certain GFP intensity is reached (arbitrarily set to 15% of the max. expression level). Additionally, we assume that it takes a time  $\tau$  to reach this level at full induction. Then we have:  $t_1(x) = t_{on}(x) + \tau$ .

Accordingly, in Figure S3a,  $x(t_1)$  was plotted against  $t_1$  and then fitted with the power law:

$$x(t_1) = \alpha \cdot (t_1 - \tau)^\beta \quad (4)$$

(the exponent  $\beta$  accounts for potential anomalous processes).  $\alpha$  is related to the apparent diffusion constant via

$$\alpha \approx \sqrt{4D_a} \cdot \text{erfc}^{-1}\left(\frac{K_a}{a_0}\right). \quad (5)$$

For  $a_0 = 10 \mu\text{M}$ , a fit to the data for the droplets close to the reservoir yields  $D = 43 \frac{\mu\text{m}^2}{\text{s}}$  and  $\beta = 0.49$ , consistent with a normal diffusion process. When the same fit is performed only to data obtained from droplets at distances larger than (arbitrarily)  $1500 \mu\text{m}$ , the apparent diffusion coefficient is considerably reduced. As can be seen in Fig. S3b, the maximum GFP production rate slows down at large distances, and therefore GFP expression may not faithfully report the diffusion of AHL in the system. Potentially, at large distances the AHL concentration does not rise quickly enough to justify the assumption of an “all or none” expression. Furthermore, a reduced expression rate may be due to a degradation of the cell-free extract over time, which is felt more strongly at large distances.

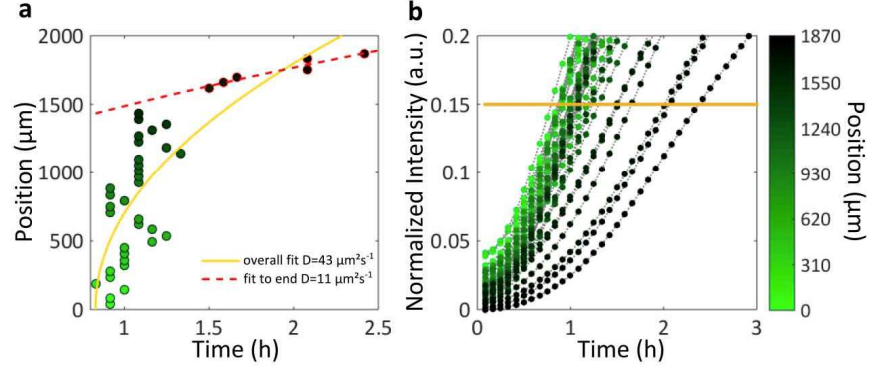


**Figure S3 Estimation of  $D_a$  from data from the 10  $\mu\text{M}$  AHL reservoir.** **a)** A plot of position vs. the time  $t_1$  at which 15% of total expression is reached (defined in (b)) is fitted with a power law (eq. (4)) to estimate the apparent diffusion constant. The orange line corresponds to a fit to all data points, whereas the dashed red line represents a fit (with fixed  $\beta = 0.5$ ) to data points obtained at a distance larger than 1500  $\mu\text{m}$  from the reservoir, indicated by red edges. **b)**  $t_1$  is defined as the time when the time trace of a droplet at a certain position, indicated by the colour bar, has reached a level of 15% of the maximum intensity.

## 2.2 Reaction-diffusion modelling

In order to more accurately estimate the apparent diffusion coefficient than in the previous section, we have to account for the kinetics of GFP production in the droplets in greater detail. To this end, numerical simulations based on a simplified reaction-diffusion model and parameters determined from bulk experiments were performed and compared to the experimental data.

The model equations are:

$$\begin{aligned}\frac{\partial a}{\partial t} &= D_a \frac{\partial^2 a}{\partial x^2} - \delta_a a, \\ \frac{\partial g}{\partial t} &= \frac{\alpha_g(t) \cdot a^n}{K_a^n + a^n} - g \alpha_{mat}, \\ \frac{\partial g_{mat}}{\partial t} &= g \alpha_{mat}.\end{aligned}$$

Here,  $a$ ,  $g$  and  $g_{mat}$  are the concentrations of AHL, nascent and matured GFP, respectively.  $D_a$  is the apparent diffusion coefficient of AHL and  $\delta_a$  is its degradation rate. The Hill exponent  $n$  and the induction threshold  $K_a$  describe the transfer function and were determined in bulk experiments (Fig. S1). It was assumed that the GFP expression rate,  $\alpha_g(t)$ , in the cell extract exponentially approaches the expression rate of full induction,  $\alpha_{max}$  (as shown by Karzbrun et al.<sup>1</sup>), with  $\alpha_g(t) = \alpha_{max}(1 - \exp[-(t - t_1)/t_2])$ . The delay time in protein expression at the beginning is expressed by  $t_1$  and the lifetime of mRNA molecules by  $t_2$ .  $\alpha_{max}$  effectively serves as a scaling variable and was adjusted in the simulations. Boundary and initial conditions were chosen as before.

The equations were solved numerically applying the MATLAB solver *pdepe*. Since the model does not account for depletion of resources in the cell extract it is only applied to the first  $\approx 2\text{h}$  of the reactions. Additionally, a dead time of 5-40 min is assumed, corresponding to the dead time for the different experiments. Simulation parameters are listed in Table S2. As shown in Figure S4, the model can reproduce the observed kinetics quite satisfactorily.  $D_a$  and  $\alpha_g$  as the only fit parameters essentially influence the ‘fanning out’ and scaling of the curves, respectively. We note that variation of the other parameters results primarily in changes of the reaction kinetics, i.e. the curvature of the time traces, but cannot account for their fanning out. The estimated apparent diffusion constant for  $a_0 = 10 \mu\text{M}$  is within the range estimated before. Surprisingly, for lower reservoir concentrations (e.g.,  $a_0 = 1 \mu\text{M}$ ) the simulation matches

the experimental data only by setting an apparent diffusion coefficient that is decreased by about 2 orders of magnitude (Table S1).

**Table S1: comparison of estimated apparent diffusion coefficients**

|  |      |      |            |    |
|--|------|------|------------|----|
| $a_0$ ( $\mu\text{M}$ )                      | 0.2  | 1    | 10         |    |
| method                                       | RD   | RD   | analytical | RD |
| $\beta$                                      | -    | -    | 0.49       | -  |
| $D_{a,eff}$ ( $\mu\text{m}^2\text{s}^{-1}$ ) | 0.15 | 0.08 | 11-43      | 25 |

**Table S2: parameters included in the simulations**

|  |                      |      |     |                               |
|--|----------------------|------|-----|-------------------------------|
| $a_0$ ( $\mu\text{M}$ )                      | 0.2                  | 1    | 10  | Source                        |
| $D_{a,eff}$ ( $\mu\text{m}^2\text{s}^{-1}$ ) | 0.15                 | 0.08 | 25  | adjusted                      |
| $\alpha_g$ ( $\text{pM s}^{-1}$ )            | 400                  | 180  | 280 | adjusted                      |
| $\delta_a$ ( $\text{s}^{-1}$ )               | $10^{-5}$            |      |     | (Hense, 2007) <sup>2</sup>    |
| $\alpha_{mat}$ ( $\text{s}^{-1}$ )           | $3.33 \cdot 10^{-3}$ |      |     | (Iizuka, 2011) <sup>3</sup>   |
| $n$  | 1.8                  |      |     | bulk experiment               |
| $K_a$ (nM)                                   | 9.9                  |      |     | bulk experiment               |
| $t_1$ (min)                                  | 20                   |      |     | (Karzbrun, 2011) <sup>1</sup> |
| $t_2$ (min)                                  | 12                   |      |     | (Karzbrun 2011) <sup>1</sup>  |

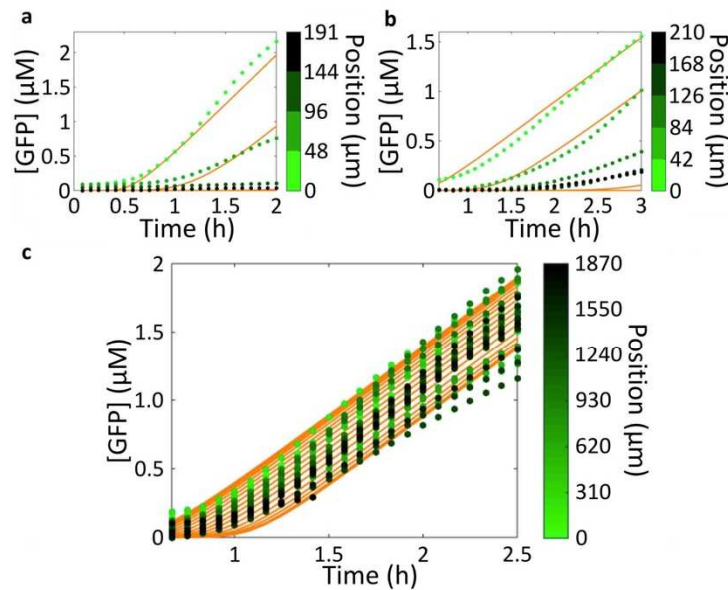


**Figure S4: Estimation of apparent diffusion coefficients from the RD model.** Orange lines represent simulations, while dots represent experimental data. Positions of droplets are indicated by colour bars. **a)**  $a_0=200$  nM, **b)**  $a_0 = 1$   $\mu\text{M}$  **c)**  $a_0=10$   $\mu\text{M}$ . Simulation parameters are listed in Table S2. Experimental data can only be reproduced by using a  $\approx 100$ -fold higher apparent diffusion coefficient for  $a_0=10$   $\mu\text{M}$  compared to the lower reservoir concentrations. Note that the model was applied to simulate the initial phase of the reaction only, and the estimated dead time was 5 min for (a) and 40 for (b),(c), respectively.

### 2.3 Discussion

A variety of effects have to be considered that can potentially account for the reduced diffusion coefficients determined in the previous sections, in particular the discrepancy between the apparent diffusion coefficient for high and low reservoir concentrations:

- a) Depletion of resources and accumulation of waste products in the cell-free droplets
- b) Depletion of AHL by binding to LuxR, and degradation.
- c) Transport mechanisms in a water-in-oil emulsion.

a): Indeed we experimentally observe a change in the cell-free expression medium as indicated, e.g., by changes in pH (Figure S5), probably leading to a slowing down of GFP expression over time. Heuristically, this could be modelled by time dependent reaction constants in the model. In order to avoid complications caused by degradation, we applied the reaction-diffusion model only for the first  $\approx 2$  h of the reaction.

b): The apparent diffusion coefficient could indeed be concentration dependent if the diffusing molecules were immobilized along their path. Binding of AHL to LuxR occurs with a dissociation constant of  $\approx 100$  nM<sup>4</sup> and an estimated unbinding rate of  $\approx 10$  min<sup>-1</sup><sup>5</sup>. In the cell-free system, LuxR is synthesized during the reaction, potentially reaching concentrations of a few  $\mu$ M. Simulations taking reversible binding of AHL to LuxR into account could however not provide an explanation for the observed concentration dependent diffusion behavior.

c): In general, the apparent diffusion coefficient of small molecules in water-in-oil emulsions depends on the different diffusion coefficients in the oil and water phase, partitioning between the phases, interfacial properties and geometrical factors. In systems similar to ours (FC-40 oil and 'EA-surfactant') it was found that the permeability between droplets is primarily dependent on partitioning between the oil and water phase, which in turn depends on the surfactant concentration. The 'EA-surfactant' was designed for optimal emulsion stability and biocompatibility. It is not expected for this surfactant/oil system to form surfactant bilayers due to steric interactions between the relatively long triblock copolymers of perfluorinated polyethers (2000 – 6000 g/mol) which serve as tail groups<sup>6</sup>. Furthermore the tail groups are very well soluble in the continuous phase, reducing the adhesion energy between the monolayers<sup>7</sup>. Since the head groups are uncharged, it is unlikely that the stabilizing surfactant monolayer at the droplets boundary acts as a major barrier to diffusion<sup>8,9</sup>.

In a simplified model, the apparent diffusion coefficient for a system composed of a droplet of radius  $r$  with diffusion coefficient  $D_{aqueous}$  and an oil barrier of thickness  $h$  and diffusivity  $D_{continuous}$  fulfills the relation:

$$\frac{L}{D_a} = \frac{2r}{D_{aqueous}} + \frac{h}{KD_{continuous}},$$

where  $L = 2r + h$ . The partition constant  $K = \frac{c_{continuous,eq}}{c_{aqueous,eq}}$  describes the equilibrium concentrations at the oil-water interface. The permeability is defined as:

$$P = \frac{KD_{continuous}}{h}.$$

Typically the diffusion coefficient of small molecules such as AHL in aqueous solution is on the order of  $D_w \approx 100 - 1000 \mu\text{m}^2/\text{s}$ , which would be similar in M9 medium for droplets containing bacteria. Since the viscosity of the cell-free system should be comparable to that of the *E.coli* cytoplasm, the diffusion coefficient would be reduced by a factor between 2 and 5 in cell-free droplets. The same argument can be made for the diffusion coefficient in fluorinated oil, which has a 4-fold higher viscosity than water so that  $D_{oil} \approx 25 - 250 \mu\text{m}^2/\text{s}$ . Furthermore, a typical diffusion coefficient of surfactant micelles is about  $D_{micelles} \approx 1 \mu\text{m}^2/\text{s}$ <sup>8</sup>.

If we assume that  $D_{aqueous} \gg LP$  and  $L \approx 2r$ , the apparent diffusion coefficient is dominated by the permeability, i.e.,  $D_a \approx LP = \frac{LK}{h} D_{continuous}$ .

If the AHL concentration in the reservoir is very high, it is conceivable that the fraction of AHL partitioned into the oil phase (even for low  $K$ ) is sufficient to induce gene expression. In this case, the apparent  $D_a$  "sensed" by the droplets will be proportional to  $D_{oil} \approx 25 - 250 \mu\text{m}^2/\text{s}$ . By contrast, for low inducer concentrations, AHL partitioning into oil



is too low, and AHL transport through micelles will dominate, i.e.,  $D_a \sim D_{micelles} \approx 1 \mu\text{m}^2/\text{s}$ . This may in fact account for the observed factor of  $\approx 100$  between the apparent diffusion coefficients for low and high AHL.

### 3. pH changes in the cell-free transcription/translation system

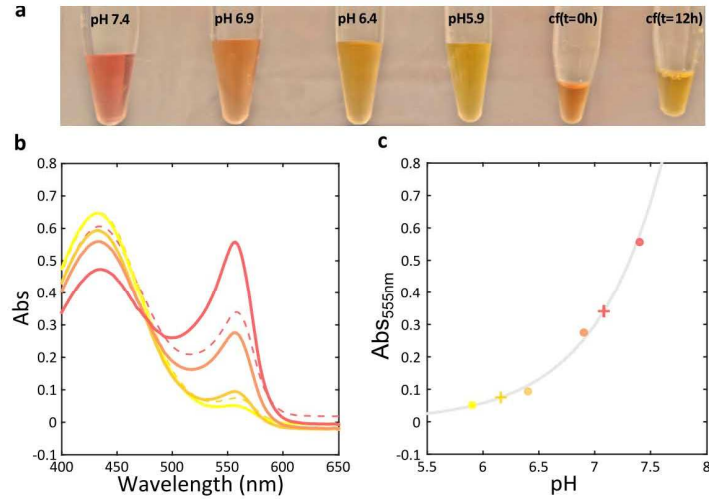


**Figure S5: pH values in the cell free system tested with phenol red.** **a)** Phenol red calibration solutions (100  $\mu\text{M}$  in PBS) between pH 7.4 and pH 5.9 and cell-free reactions supplemented with 100  $\mu\text{M}$  phenol red. **b)** Absorption spectra of calibration solutions and the cell free samples (dashed lines) at  $t = 0\text{h}$  and  $t = 12\text{h}$  after initiation of the experiment. **c)** Absorption maxima at 555 nm plotted against the corresponding pH values. Data points were fitted with an exponential curve.

#### 4. Additional data – AHL and IPTG reservoir for bacteria and cell free system

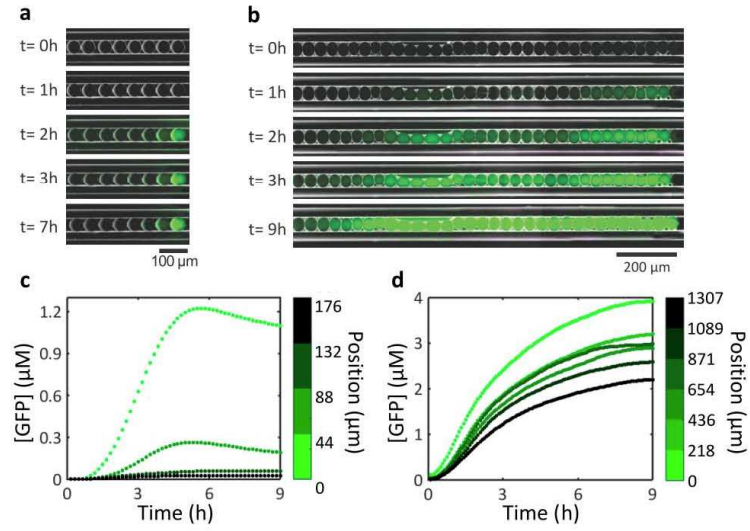


**Figure S6: Cell-free droplets next to AHL reservoirs (alternative data set to main paper).** **a)** Time series for a reservoir concentration of 200 nM. **b)** Time series for a reservoir concentration of  $10\text{ }\mu\text{M}$ . **c)** Average time traces from 3 capillaries for  $\alpha_0 = 200\text{ nM}$ , positions indicated by the colour bar. **d)** Average time traces from 3 capillaries for  $\alpha_0 = 10\text{ }\mu\text{M}$ . For clarity, time traces represent averages from groups of 5 neighbouring droplets.

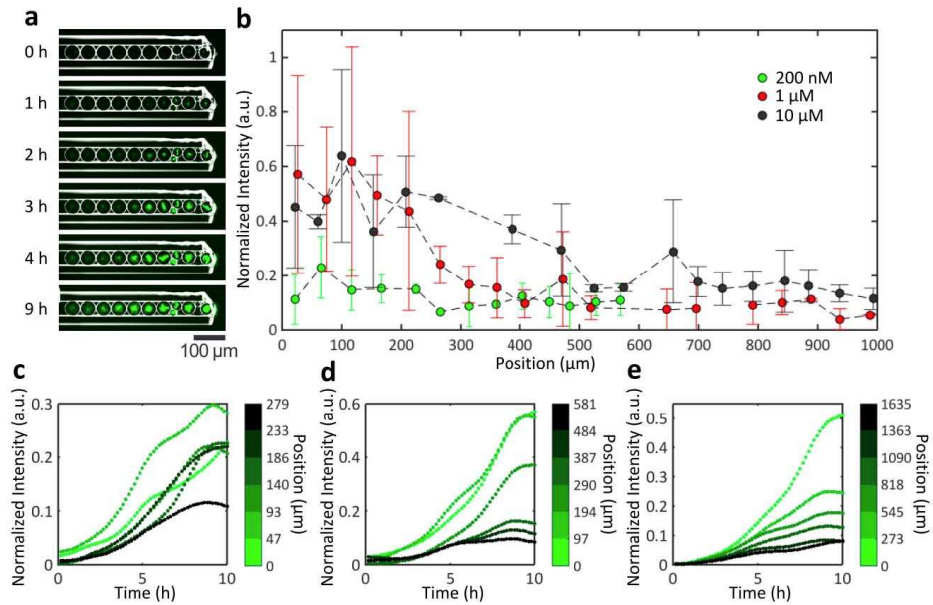


**Figure S7: AND gate bacteria in droplets next to AHL reservoirs.** **a)** Time series of bacteria containing droplets exposed to a reservoir concentration of 1  $\mu\text{M}$ . Expression of GFP is sequentially induced as AHL diffuses into the capillary from right to left. **b)** Average fluorescence profiles for reservoir concentrations of 200 nM, 1  $\mu\text{M}$  and 10  $\mu\text{M}$  9 h after initiation of the experiments. Error bars represent standard deviations from 3, 2 and 2 individual capillaries, respectively. **c)** Average time traces for the first 6 droplets next to a 200 nM reservoir. Positions of droplets are indicated by colour bars. **d)** Average time traces for  $\alpha_0 = 1 \mu\text{M}$ . For clarity, each trace represents the average of two neighbouring droplets. **e)** Average time traces for  $\alpha_0 = 10 \mu\text{M}$ . Each trace represents the average of 6 neighbouring droplets.

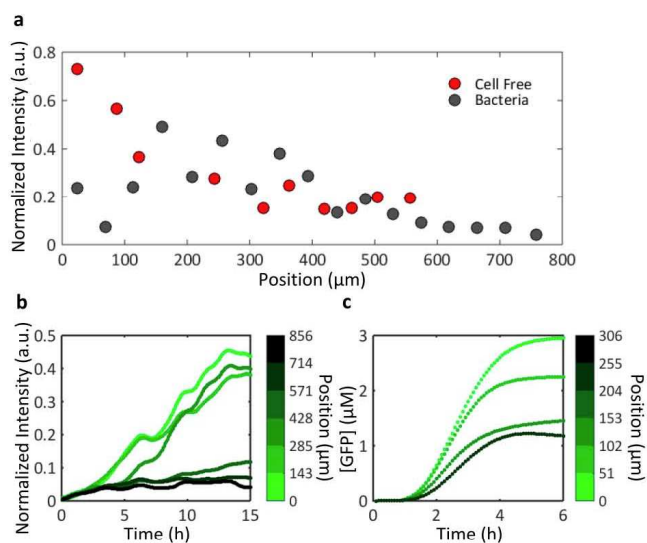


**Figure S8: Cell-free and bacteria containing droplets next to 10mM IPTG reservoirs.** a) Fluorescence profiles for cell-free and bacteria containing droplets 15 h after initiation of the experiments. b) Time traces for bacteria containing droplets, where positions are indicated by the colour bar. Data represents averages from 3 neighbouring droplets for a single capillary. c) Time traces for cell free droplets (data from a single capillary).

## 5. SI methods

### 5.1 Data processing

Microscope images were analysed with an automated droplet tracking software developed in the lab<sup>10</sup>. Time traces of cell-free droplets were generated by taking the mean fluorescence intensities over the whole droplet area (determined from bright field images). Since bacteria accumulate in the centre of the droplet, in this case the mean was taken only from bright pixels (defined by automated thresholding). Intensity traces were then normalized by subtracting the minimum of all traces of one capillary. Based on the distance of the droplets the time traces of multiple (2-3) capillaries were averaged. Subsequently, time traces were normalized to the maximum intensity for bacterial receivers. For cell-free receivers, a calibration with droplets containing purified GFP was performed. Finally, time traces were smoothed in MATLAB with the function *smoothn* (S=100) to reduce the noise and account for missing data points. For data spanning more than one observation area, i.e. 1  $\mu\text{M}$  and 10  $\mu\text{M}$  AHL reservoirs, images A and B were recorded with an overlap so that a reference droplet was present in each image. Accordingly, extracted data was stitched by transforming the positions of droplets in B to the coordinate system of A. It was ensured that droplets present in both images were not taken twice. Positions of droplets were calculated as the distance to the first droplet plus the radius of the first droplet. Pixel sizes of the cameras are 8  $\mu\text{m}$  and 13  $\mu\text{m}$  for IX71 and IX81, respectively. For data of hybrids, droplets were sorted manually dependent on their number of sender neighbours/ their position inside the capillary and averaged.

### 5.2 Filling of the capillaries

Squared borosilicate glass capillaries with dimensions 50  $\mu\text{m}$  x 50  $\mu\text{m}$  x 5 cm (VetroCom, USA) were fixed by placing one end of the capillary between a freshly activated PDMS block and a glass slide (Fig. S9). The end of the capillary was positioned within a pre-punched hole in the PDMS block (diameter 1.25 mm), into which the droplet solution was pipetted. The capillaries were filled by manually applying pressure on the PDMS block. Filled capillaries were sealed with vacuum grease and nail polisher. For the experiments with several droplet species, we scanned for and then focused on appropriate droplet configurations.

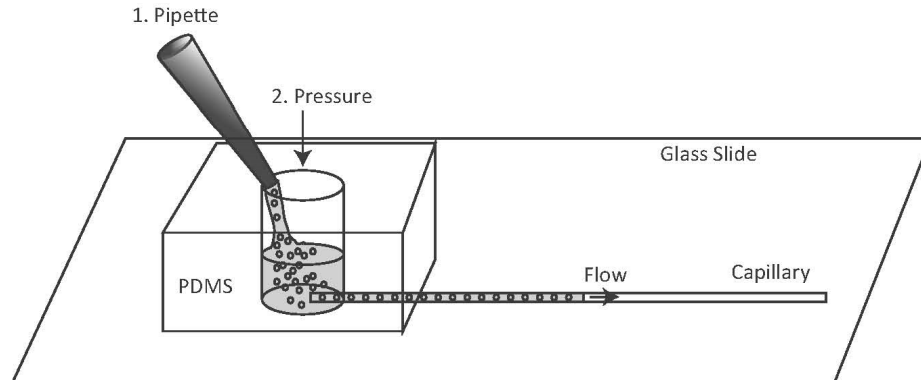
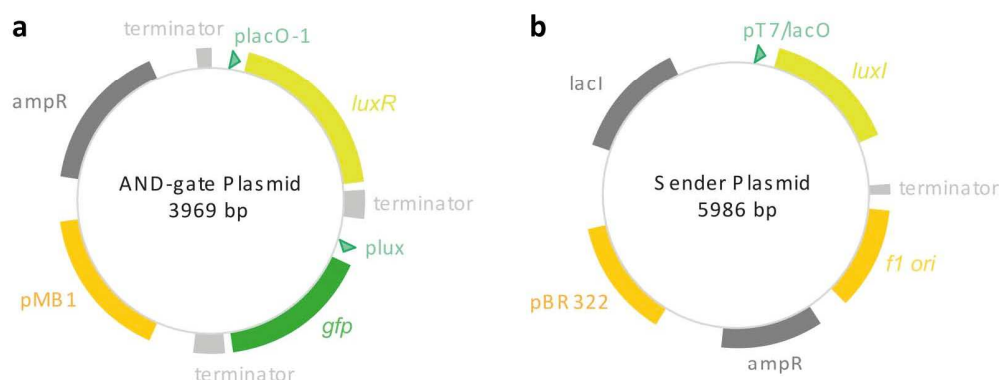


Figure S9: Filling of capillaries.

## 5.3 Plasmid maps



**Figure S10: Plasmid Maps of constructs used in this study.** a) The AND-gate plasmid is based on the BioBrick part pSB1A3 with insert T9002 completed with *lacO-1* promoter. b) pETDuet-1 vector was used for the sender plasmid with the BioBrick insert C0061 (*luxI*). Construction details can be extracted from Weitz et al.<sup>11</sup>

## Supplementary References

1. E. Karzbrun, J. Shin, R. H. Bar-Ziv and V. Noireaux, Coarse-Grained Dynamics of Protein Synthesis in a Cell-Free System, *Phys. Rev. Lett.*, 2011, **106**, 048104.
2. B. A. Hense, C. Kuttler, J. Müller, M. Rothballer, A. Hartmann and J.-U. Kreft, Does efficiency sensing unify diffusion and quorum sensing?, *Nat. Rev. Microbiol.*, 2007, **5**, 230-239.
3. R. Iizuka, M. Yamagishi-Shirasaki and T. Funatsu, Kinetic study of de novo chromophore maturation of fluorescent proteins, *Analytical Biochemistry*, 2011, **414**, 173-178.
4. M. L. Urbanowski, C. P. Lostroh and E. P. Greenberg, Reversible acyl-homoserine lactone binding to purified *Vibrio fischeri* LuxR protein, *Journal of Bacteriology*, 2004, **186**, 631-637.
5. M. Weber and J. Buceta, Dynamics of the quorum sensing switch: stochastic and non-stationary effects, *BMC systems biology*, 2013, **7**, 6.
6. C. Holtze, A. C. Rowat, J. J. Agresti, J. B. Hutchison, F. E. Angilè, C. H. J. Schmitz, S. Köster, H. Duan, K. J. Humphry, R. A. Scanga, J. S. Johnson, D. Pisignano and D. A. Weitz, Biocompatible surfactants for water-in-fluorocarbon emulsions, *Lab Chip*, 2008, **8**, 1632.
7. P. Poulin and J. Bibette, Adhesion of Water Droplets in Organic Solvent, *Langmuir*, 1998, **14**, 6341-6343.
8. Y. Skhiri, P. Gruner, B. Semin, Q. Brosseau, D. Pekin, L. Mazutis, V. Goust, F. Kleinschmidt, A. El Harrak, J. B. Hutchison, E. Mayot, J.-F. Bartolo, A. D. Griffiths, V. Taly and J.-C. Baret, Dynamics of molecular transport by surfactants in emulsions, *Soft Matter*, 2012, **8**, 10618.
9. A. R. Thiam, N. Bremond and J. Bibette, From stability to permeability of adhesive emulsion bilayers, *Langmuir*, 2012, **28**, 6291-6298.
10. K. Kapsner and F. C. Simmel, Partitioning Variability of a Compartmentalized In Vitro Transcriptional Thresholding Circuit, *ACS Synth. Biol.*, 2015, **4**, 1136-1143.
11. M. Weitz, A. Mückl, K. Kapsner, R. Berg, A. Meyer and F. C. Simmel, Communication and computation by bacteria compartmentalized within microemulsion droplets, *J Am Chem Soc*, 2014, **136**, 72-75.



## Acknowledgement – Danksagung

Vielen Dank...

- an Ilka, für das in mich gesetzte Vertrauen, ohne dich wäre diese Arbeit nicht zustande gekommen.
- an Markus Kollmann für die aufrichtige Übernahme der Zweitbetreuung.
- an Fritz, weil ich immer die Möglichkeit hatte, meine eigenen Ideen zu verwirklichen.
- an das komplette Simmel Lab, für die schöne Zeit gegenseitiger Motivation und Begeisterung für all unsere Projekte.
- Helene, für deine Unterstützung in jeder Hinsicht und deiner offenherzigen Hilfsbereitschaft beim „Mal was ausprobieren“
- Andrea, Katrin, Korbinian, Matthäus, Maxi, Tiago und Severin für die gemeinsame Zeit im Labor und die erfolgreiche Zusammenarbeit
- Evi, Katha und Flo für die wertvollen Diskussionen rund um *E. coli*.
- Claudia Paulus und Peter Weiser für die exzellente Reinraumbetreuung.
- dem BACTOCOM-Konsortium und dem Center for NanoScience (CeNS) für das tolle Netzwerk
- an meinen Mann und meiner ganzen Familie, dass ihr für mich da seid!

# Curriculum Vitae

|                    |  |
|--------------------|--|
| Name               | Andrea Mückl   |
| Place of birth     | Cham, Germany  |
| 2016 – 2018        | <b>PhD in Biology</b><br>Institute of Synthetic Microbiology, Jun.-Prof. Dr. Ilka M. Axmann<br>Heinrich-Heine-University Düsseldorf<br><i>Thesis: Bacterial communication in synthetic biology quantified by single cell (droplet) microfluidics</i> |
| since 2011         | <b>Laboratory engineer</b><br>Physics of Synthetic Biological Systems, Prof. Dr. Friedrich C. Simmel<br>Technical University of Munich   |
| 2010               | <b>Project manager</b><br>Bioprocess Engineering and Food Technology, ttz-Bremerhaven  |
| 2007 – 2010        | <b>Dipl. Ing. (FH) Biotechnology</b><br>Hochschule Darmstadt<br><i>Thesis: Optimization of a Fluorescence Immunoassay for quantitative detection of aflatoxin M1 in milk and the transfer to a micro-fluidic device</i>                              |
| 2004 – 2007        | <b>Dipl. Ing. (FH) Biotechnology</b><br>FH Weihenstephan – Freising  |
| 2002 – 2004        | <b>Fachhochschulreife</b><br>Fachoberschule – Cham<br>Specialization: Social work  |
| 1998 – 2002        | <b>Mittlerer Bildungsabschluss</b><br>Realschule – Furth im Wald<br>Specialization: Technology   |
| München, Nov. 2017 | Andrea Mückl   |